Temporal fluctuations in the motion of Arctic ice masses from satellite radar interferometry

Steven J. Palmer

PhD

The University of Edinburgh

School of GeoSciences

College of Science and Engineering

2009

Declaration

This thesis represents the culmination of four years of work. The work presented is my own; where content has been published or submitted for publication elsewhere, I have noted the contribution of co-authors accordingly. This thesis has not been submitted for any other professional qualification.

Steven J. Palmer

Acknowledgements

I'm grateful to Andrew Shepherd for providing training and supervision. Many thanks to Margaret Palmer for constant support (despite my decision not to study law). Thanks also to Matt Palmer and Becca Broughton for showing me how to be successful at school and beyond. Extra thanks to Matt for useful discussions about my work and for giving me feedback on various chapters of this thesis. I'm grateful to Shiela Wilkinson and the extended Wilkinson clan for providing a loving and supportive environment and especially to Ken Wilkinson for interesting discussions about New Scientist articles from an early age. Thanks to Ben Broughton, Damien Gardiner, Steve and Ali Morris, Andy Doré, James Gething and Pete Gething for showing me that embarking on a PhD was the right decision. I'm grateful to Toby Benham and Bob Hawley at Scott Polar Research Institute for patient advice in the early days of my PhD. Thanks to fellow students and postdocs at SPRI and Edinburgh (Kelly Hogan, Ruth Mugford, Stewart Jamieson, Vicki Parry, Kate Briggs, Mal McMillan, Ian Bartholomew, Iain Cameron, Aud Sundal, Eero Rinne, Santiago de la Peña and Noel Gourmelen) for various fruitful discussions on methods and glaciological interpretation. Thanks to Ruth Lewis for sharing part of the PhD experience with me. Additional thanks to Tony Payne, Hans Oerlemans, Bob Bindschadler, Finnur Palsson and especially Pete Nienow, who have all influenced aspects of my work over the last four years. Finally, thanks to Katharine Fitzpatrick for loving support and helping to keep a smile on my face over the past six months.

Contents

List of figures

List of Tables

Abstract

This thesis considers the use of Interferometric Synthetic Aperture Radar (InSAR) for surveying temporal fluctuations in the velocity of glaciers in the Arctic region. The aim of this thesis is to gain a broader understanding of the manner in which the flow of both land- and marine-terminating glaciers varies over time, and to asses the ability of InSAR to resolve flow changes over timescales which provide useful information about the physical processes that control them. InSAR makes use of the electromagnetic phase difference between successive SAR images to produce interference patterns (interferograms) which contain information on the topography and motion of the Earth's surface in the direction of the radar line-of-sight. We apply established InSAR techniques (Goldstein et al., 1993) to (i) the 925 km^2 Langjökull Ice Cap (LIC) in Iceland, which terminates on land (ii) the 8 500 km^2 Flade Isblink Icecap (FIIC) in Northeast Greenland which has both land- and marine-terminating glaciers and (iii) to a 7 000 km^2 land-terminating sector of the Western Greenland Ice Sheet (GrIS). It is found that these three regions exhibit velocity variations over contrasting timescales. At the LIC, we use an existing ice surface elevation model and dual-look SAR data acquired by the European Remote Sensing (ERS) satellite to estimate ice velocity (Joughin et al., 1998) during late-February in 1994. A comparison with direct velocity measurements determined by global positioning system (GPS) sensors during the summer of 2001 shows agreement ($r^2 = 0.86$), suggesting that the LIC exhibits moderate seasonal and inter-annual variations in ice flow. At the FIIC, we difference pairs of interferograms (Kwok and Fahnestock, 1996) formed using ERS SAR data acquired between 15th August 1995 and 3rd February 1996 to estimate ice velocity on four separate days. We observe that the flow of 5 of the 8 outlet glaciers varies in late-summer compared with winter, although flow speeds vary by up to 20 % over a 10 day period in August 1995. At the GrIS, we use InSAR (Joughin et al., 1996) and ERS SAR data to reveal a detailed pattern of seasonal velocity variations, with ice speeds in late-summer up to three times greater than wintertime rates. We show that the degree of seasonal speedup is spatially variable and correlated with modeled runoff, suggesting that seasonal velocity changes are controlled by the routing of water melted at the ice sheet surface.

The overall conclusion of this work is that the technique of InSAR can provide useful

information on fluctuations in ice speed across a range of timescales. Although some ice masses exhibit little or no temporal flow variability, others show marked inter-annual, seasonal and even daily variations in speed. We observe variations in seasonality in ice flow over distances of ~ 10 km and over time periods of ~10 days during late-summer. With the aid of ancillary meteorological data, we are able to establish that rates of flow in western Greenland are strongly moderated by the degree of surface melting, which varies seasonally and secularly. Although the sampling of our data is insufficiently frequent and spans too brief a period for us to derive a general relationship between climate and seasonality of flow, we show that production of meltwater at the ice surface and its delivery to the ice bed play an important role in the modulation of horizontal flow speeds. We suggest that a similarly detailed investigation of other ice masses is required to reduce the uncertainty in predictions of the future Arctic land-ice contribution to sea level in a warming world.

Chapter 1: Introduction

1.1. Aim

The aim of this thesis is to investigate the use of satellite interferometric synthetic aperture radar (InSAR) techniques for detecting temporal fluctuations in the flow rate of land- and marine-terminating glaciers. The results of this work contribute towards a growing inventory of monitored glaciers and provide a more detailed understanding of the processes that control glacier dynamics.

1.2. Motivation

The amount of ice on the Earth is decreasing (Lemke et al., 2007). The Intergovernmental Panel on Climate Change (IPCC) fourth assessment (AR4) provides evidence of widespread retreat of glaciers and ice caps since the end of the 19th century, though large uncertainties in estimates of ice mass loss exist due to incomplete coverage of monitored ice masses (Solomon et al., 2007). Recent remote sensing studies have shown that the margins of the Greenland Ice Sheet (GrIS) are thinning (Krabill et al., 2004; Pritchard et al., 2009) through increased surface melting (Abdalati et al., 2001) and increased rates of ice mass flux into the surrounding ocean (Rignot and Kanagaratnam, 2006). However, incomplete model physics, inadequate model resolution and insufficient understanding of ice-ocean interactions limits our ability to predict the response of Earth's ice masses to recent and projected warming (Meehl et al., 2007). Additional uncertainties arise due to incomplete understanding of the processes that govern ice flow and ice sheet stability - this thesis investigates the use of satellite radar interferometry to address these key uncertainties.

Ice motion is affected by many factors, including the balance of surface mass accumulation (surface mass balance), glacier geometry and the extent of sliding at the bed. For marine-terminating ice, the additional factors of tidal displacements and back-pressure from an ice shelf or glacier tongue may also be applicable (Paterson, 1994). Ice formed from compacted snow spreads and slides under gravity to lower elevations, where it melts or calves into the ocean to form icebergs. Ice motion therefore controls the rate at which ice is transported from regions of accumulation to regions of ablation

and/or loss by iceberg calving. Changes in ice basal conditions such as the presence of saturated underlying sediment affect the force balance of the ice and may result in ice dynamical changes (Paterson, 1994). Observations of temporal variations in the motion of ice caps and ice sheets have the potential to improve our understanding of the processes controlling ice dynamics, which is crucial for making accurate predictions of how the cryosphere will respond to current and future climate.

The technique of interferometric synthetic aperture radar (InSAR) is capable of detecting ice motion and has enabled great accuracy in measurements of glacier surface elevation (metre-scale) and motion (centimetre-scale) (e.g. Joughin et al., 1996a). The main advantage of InSAR over ground-based methods (e.g. Global Positioning System (GPS)) is that it can be used to determine precise ice motion and elevation over areas of the order of 10 000 km^2 simultaneously (Joughin et al., 2000; Madsen and Zebker, 1998). An advantage of InSAR over other remote sensing techniques is the ability to retrieve data from featureless areas of ice such as the interior of Greenland and Antarctica (Goldstein et al., 1993; Joughin et al., 1995; Kwok and Fahnestock, 1996). Other techniques require surface features such as supraglacial debris or crevasses in order to measure ice motion. Utilisation of a 'window' in the atmospheric absorption spectrum means also that this active technique can be used irrespective of cloud cover and illumination conditions, unlike optical techniques. These considerations show InSAR to be a suitable method for achieving the aims of this thesis. In the following sections, we summarise recent remote sensing observations of Arctic ice masses and identify the research objectives of this thesis.

1.3. Background

1.3.1. The cryosphere within the climate system.

The cryosphere consists of the Earth's snow, ice and frozen ground and is a key component of the climate system. Presently, ice permanently covers about 10% of the Earth's land surface, of which only a tiny fraction (less than 0.5 % by volume) lies in ice caps and glaciers outside Antarctica and Greenland (Lemke et al., 2007). The cryosphere responds to climate variations over a wide range of time scales (hourly to millenial), making it a natural barometer of climate variability and change. Fluctuations in climate

result in variations in snowfall and in melting, which result in the expansion or contraction of an ice mass (Paterson, 1994). These climate-driven fluctuations in ice mass represent 'noise' to studies of longer-term trends in the mass balance of the cryosphere. Recent decreases in ice mass are correlated with rising surface air temperatures (Box et al., 2006) and ocean temperatures (Hanna et al., 2009). This relationship is clearest for the Arctic region, where temperatures have increased by about twice the global average since the 1960s (e.g.Alley et al., 2003; Zhang, 2005) and which is the geographical focus of this thesis.

Ice caps adapt to changes in climate conditions much more rapidly than ice sheets (Dowdeswell et al., 1997) because they typically have a higher ratio between annual mass turnover and their total mass. They are typically in maritime settings with higher accumulation and ablation rates than the ice sheets and so the mass turnover rate is also higher, making them sensitive to changes in accumulation. Ice caps are widely distributed geographically, in many cases providing information in remote areas where no direct climate records are available. Changes in the mass balance of ice caps contribute to sea level changes and affect the freshwater availability in the surrounding regions.

The present-day retreat of glaciers and ice caps is making a substantial contribution to sea level rise. Raper and Braithwaite (2006) estimated mean annual contribution of glaciers and ice caps to sea level over the 20th Century was about 30 mm, 16 % of the total observed rise. Dyurgerov and Meier (2000) estimated that the mass loss of glaciers and ice caps over the last 4 decades of the 20th century was 150 mm yr^{-1} water equivalent and showed a distinct increase in response to a warming of the climate in the mid-1970s. Due to its large area (275 000 km^2), Arctic land ice (excluding the GrIS) represents one of the largest contributions to sea level rise; Dowdeswell et al., (1997) estimated it to be 0.13 mm yr^{-1} at the end of the 20th century. Glaciers and ice caps are expected to continue to make a significant contribution over the next 100 years, though projections show a large range of estimates. Raper and Braithwaite (2006) estimate that glaciers and ice caps will contribute around 50 mm to global sea level during the 21st century, while Meier et al., (2007) estimate a value of 100 - 250 mm. A more recent study (Bahr et al., 2009) estimated a lower bound of the contribution to be 180 ± 30 mm though the authors suggest a value of 370 ± 20 mm to be more likely.

The volumes of the Greenland and Antarctic ice sheets are equivalent to approximately 7 m and 57 m of sea level rise, respectively. Although the Greenland Ice Sheet (GrIS) contains only 12% of the potential contribution of Antarctica to future sea level rise, it is currently an unequivocal source (Lemke et al., 2007) which has made it the major focus of current glaciological research (including Chapter 4 of this thesis). New and improved observational techniques such as satellite altimetry and InSAR reveal changes in many parts of the large ice sheets. Microwave backscatter observations have shown that the total melted area in Greenland has increased by ~16 % between 1979 and 2002, with widespread melting above 2000 m elevation observed in 2002 and 2005 (Steffen et al., 2004; Hanna et al., 2005). Thickening in central regions of Greenland has been more than compensated by increased melting near the coast (Pritchard et al., 2009).

1.3.2 Mechanisms of ice motion

Ice moves under its own weight through a combination of internal deformation, sliding at the ice/bed interface and deformation of the bed. Surface velocity results from the combined contribution of these mechanisms of motion. As InSAR detects motion of the ice surface, it can be used to investigate all three processes; though isolating the individual contributions is difficult in the absence of additional data. Each of the mechanisms is described in more detail below.

1.3.2.1. Internal deformation

Several processes contribute to the deformation of polycrystalline ice and are summarised by Paterson (1994). A constitutive relation between stress σ and strain rate $\dot{\varepsilon}$ is given by the Glen-Nye Flow Law (Glen, 1955):

$$\dot{\varepsilon} = k\sigma^n \tag{1.1}$$

where k and n are constants. The value of k depends on temperature though a value of 3 is typically used (Paterson, 1994). The lowest velocities are near the base of the ice where friction acts against flow, and sliding at the bed occurs. Velocity increases with vertical distance from the bed and with horizontal distance from the edge of a glacier towards the centre-line, as the amount of deformation decreases.

1.3.2.2. Sliding

Sliding at the ice/bed interface can occur where the basal ice is at the melting point, which is a function of both temperature and pressure. The ‘sliding law’, which links basal velocity to shear stress, water pressure and the characteristics of the glacier bed, is the basal boundary condition in the analysis of ice flow for glaciers with the basal ice at the pressure melting point. Its correct formulation is essential for predicting overall motion of the glacier as well as understanding the mechanisms behind glacier surges (Paterson, 1994). An important observation, first documented by James Forbes in the mid-19th century, is the increase in surface velocity of many glaciers early in the melt season and after heavy rain. This increases the amount of water at the bed which raises basal water pressures and results in reduced basal friction (e.g. Kamb, 1987; Engelhardt and Kamb, 1998). An increase in velocity during summer suggests that a glacier is sliding. A major obstacle to the understanding of basal motion is the difficulty of observing it, though recent surface radar and seismic studies have provided new insights into conditions at the bed of fast-flowing ice in West Antarctica (e.g. King et al., 2007; Smith and Murray, 2009).

1.3.2.3. Deformation of the bed

Ice often overlies deformable sediments deposited by previous glaciations or by water, and which is generally referred to as 'till'. Significant subglacial deformation occurs only when the till is saturated with water at a pressure close to the ice-overburden pressure (Paterson, 1994). This means that the factors such as glacial hydrology, till porosity and the way in which water flows through till must be taken into account. Till is rarely homogeneous which makes it difficult to formulate general flow relations linking till deformation to applied stress. Airborne radar (Bell et al., 1998) and seismic (Anandakrishnan et al., 1998; King et al., 2007) investigations of West Antarctic ice streams have shown that the locations of fast-flowing ice coincide with the locations at which deformable sediment is present at the bed. These studies imply that deformable sediments at the ice bed influence the response of Antarctica to changes in the global climate system (Bell et al., 1998). Kjær et al., (2006) propose a ‘dual-coupled’ mechansim of fast ice flow, whereby the the glacier is coupled to a layer of sediment at the bed, below which pressurized water acts to decouple the sediment and ice above from the bedrock below. In practise, a combination of these different mechanisms of ice

flow occurs at a single glacier at different times, and simulataneously at different locations.

1.3.3. Remote sensing techniques for detecting ice motion

Accurate ice-motion measurements are necessary for a wide range of studies such as calculating the mass budget of a glacier and to constrain models of ice-sheet flow and dynamics. Such measurements are an essential prerequisite to the realistic estimation of ice-sheet mass balance, in concert with topography, ablation/accumulation, surface temperature, albedo, and ice thickness. Recent advances in satellite remote-sensing techniques have improved our ability to measure and monitor ice motion. While *in situ* GPS measurements enable high-precision point estimates of three-dimensional ice velocity (e.g., King, 2004; van de Wal et al., 2008; Shepherd et al., 2009), such data are limited in space and time and are logistically difficult to acquire. Satellite remote sensing is well suited to large-scale measurement of ice velocity, enabling the simultaneous collection of thousands of measurements over vast remote regions. Surface measurements remain, however, an important means of calibrating satellite retrievals. Recent remote sensing and *in situ* GPS and ice-penetrating radar observations have identified significant changes in the configuration and flow speeds of fast-moving ice streams on timescales ranging from decadal (e.g., Bindschadler and Vornberger, 1998) through century (Shabtaie and Bentley, 1987) to millennial (Bindschadler, 1998)

Prior to the development of InSAR techniques, the main method of retrieving ice velocity from satellite data was optical or radar feature tracking. Feature tracking determines the ice-surface velocity field by detecting and tracking identifiable features, such as crevasses, using cross correlation techniques. These features act as markers which persist in time and move with the ice. The velocity field then represents the mean rate of surface motion over the period between image acquisitions. The technique yields medium- to long-term average velocity only, with typically a year or more between sequential image pairs (e.g., Scambos et al., 1992). Moreover, the acquisition of suitable image pairs is hampered by persistent cloud cover (over ice-sheet margins, in particular) and, in the case of visible to near-IR data, polar darkness. Although feature tracking using SAR amplitude image time series (e.g. Luckman and Murray, 2005) is unaffected by cloud cover and light conditions, it suffers the same limitation as optical image

feature tracking in that identifiable features and detectable displacements must be present between image acquisitions (Forster et al., 2003). By penetrating the surface, however, the SAR is likely to locate more tracking features related to internal inhomogeneities and crevasses. Conventional feature tracking is limited both by its relative lack of precision (based on the large image pixel size), and its requirement that nunataks or other fixed points are present in the images to aid image co-registration.

The emergence of satellite SAR interferometry fills a major gap in this respect, as well as providing additional key information. InSAR is not dependent on solar illumination and cloud-free conditions, and can also provide measurements of ice motion in featureless ice sheet interior regions where conventional feature-tracking techniques typically break down. Whereas feature tracking using optical or SAR amplitude data produces velocity fields averaged over a period of months or years, InSAR can uniquely provide a near-instantaneous velocity estimate - i.e., over 24 hours. This enables resolution of short-term acceleration or deceleration in ice flow (Joughin et al., 2004a). While individual InSAR-derived pixel velocities may not be as accurate as GPS measurements, satellite InSAR has the advantage of acquiring a large number of measurements over a wide area, and over a denser spatial network than conventional feature-tracking techniques. This enables both the constraint of the ice dynamics and the detection and monitoring of changes in ice-flow regimes. To date, InSAR has mostly been used in the Arctic region to study either single marine-terminating glaciers (Joughin et al., 1996c; Joughin et al., 2004), or to map large areas of the GrIS (Rignot and Kanagaratnam, 1996). With the exception of Dowdeswell et al., 2002, it has not so far been used extensively on ice caps with a combination of land- and marine-terminating glaciers or on land-terminating sectors of the western GrIS.

1.3.4. Observed temporal variations in ice motion

Glaciological phenomena result in temporal variations in ice motion on a range of time-scales which we summarise here.

1.3.4.1. Hourly to daily

Motion events lasting hours to days have been observed at several glaciers and are summarised by Willis (1995). These events tend to occur early in summer, and during

the event, flow typically increases to a few times the mean annual rate. The events are typically asymmetrical in time, exhibiting a rapid rise and slow decline and occur at progressively higher elevations over the course of summer, for example at Variegated Glacier in Alaska, USA (Kamb and Engelhardt, 1987). These short-lived speedups have been correlated with short periods of high surface melting early in the melt season (Iken, 1974) and elevated subglacial water pressures (Iken and Bindschadler, 1986) and are sometimes accompanied by glacier uplift (Iken and Bindschadler, 1986). Borehole or moulin water levels often drop to unusually low levels after the events (Willis, 1995). Mechanisms appropriate to a range of basal conditions have been proposed to explain the observations and are summarised by Willis (1995). In all cases, the role of water is important due to its affect on basal 'lubrication'.

Diurnal cycles of glacier movement typically occur during the summer months (Willis, 1995). At the western margin of the Greenland ice sheet, GPS measurements of summertime flow have shown diurnal variations resulting from the daily cycle of melting and subsequent delivery of melted water to the glacier bed (Shepherd et al., 2009). For marine-terminating ice, additional variations can occur due to the ocean's tides, which can modulate horizontal flow (e.g. Bindschadler et al., 2003).

1.3.4.2. Daily to monthly

Previous studies have shown that daily to weekly variations in glacier surface velocity are correlated with patterns of water input to the glacier from surface melting or rainfall. For example, at Unteraargletscher, Switzerland, Flotron (unpublished data, cited in Kamb and Engelhardt, 1987) observed periods of much faster flow lasting around 5 days, which occurred at intervals of 10-30 days between mid-May and late June and which were correlated with high rates of melting. Joughin et al. (1996c) detected a "mini" surge of Ryder Glacier in north Greenland, observing that the glacier speed increased by a factor of greater than 3 before returning to the 'background value' all within a period of 7 weeks. This speedup has been attributed to the draining of several supraglacial lakes nearby. The relationship between high water inputs and speedup appears to vary during the summer. Following the first melt-related increases in speed above the 'background value', subsequent increases in water input often has little or no effect on the glacier velocity (Willis, 1995).

1.3.4.3. Monthly to annual (seasonal)

On almost all of the glaciers that have been studied, spring/summer flow velocities are greater than autumn/winter velocities (Willis, 1995). Seasonal variations in flow speeds of 10 – 15 % have been observed at the western GrIS (Joughin et al., 2008). At many glaciers, the peak summer velocity precedes the maximum ablation rates or maximum proglacial stream discharges by about 1 month (e.g. Iken, 1974). On some glaciers, the location of peak velocity in summer moves down-glacier with time. For example, a wave of peak velocity at Hintereisferner, Austria, moved down the glacier so that maximum velocities were observed in the accumulation area (8 km from the terminus) in May, while the lower ablation area (150 m from the terminus) attained maximum velocity in September (Schimpp, 1958). In contrast, other glaciers show evidence for seasonal waves of maximum velocity moving up-glacier. The peak summer velocities in the ablation area of Kitdlerssuaq Glacier, Greenland, occurred in early June whereas maximum speeds were reached in late July/early August in the accumulation area (Andreasen, 1985). Seasonal fluctuation in the drainage of rainfall and surface melt to the bed modulates the sliding speed of many alpine glaciers (Kamb et al., 1994).

1.3.4.4. Inter-annual to decadal and episodic variations

Some outlet glaciers exhibit sudden rapid advances of up to 20 km over a few months or years, known as glacier surges. Glaciers in Iceland and Svalbard are known to surge (Dowdeswell et al., 1991; Luckman et al., 2002; Björnsson et al., 2003) and surges have also been observed in many temperate glaciers (Paterson, 1994). Surge-type glaciers exhibit cyclical flow alternating between decades of 'slow-flow' punctuated by shorter periods of flow that is typically 10 – 1 000 times faster. This is too high to be produced by ice deformation and is attributed to fast sliding and/or deformation of the bed (Paterson, 1994). Different surging glaciers have different characteristics and it is unlikely that a single mechanism can explain all surges, though it is clear that the routing of water plays a crucial role.

Prior to the advent of InSAR, very little was known about the short-term variability in flow speed of glacier surges. During surge events, substantial volumes of ice can be transferred to lower altitudes, leading to a temporary acceleration of the rate of melting (Murray et al., 2001; Luckman et al., 2002). High velocities during a surge can cause loss of interferometric coherence by temporal decorrelation reducing the ability of

InSAR to map the dynamics of surging glaciers (Fatland and Lingle, 1998; Mohr et al., 1998; Murray et al., 2002). However, certain glaciers are characterized by less extreme surge episodes, which are suitable for measurement by InSAR (Dowdeswell et al., 1999; Luckman et al., 2002; Strozzi et al., 2000).

Some inter-annual to decadal variations in ice flow are associated with changes in accumulation (McConnell et al., 2000) and ablation (Hanna et al., 2008) which alter the geometry and therefore the driving stresses within the ice. Some of these changes are associated with quasi-periodic phemomena such as the Arctic Oscillation (Thompson and Wallace, 1998) and are discussed in detail elsewhere (e.g. Hurrell, 1995).

1.3.5. Background to the study areas

1.3.5.1. Langjökull ice cap, Iceland

The Langjökull ice cap (LIC) is Iceland's second largest ice cap (Björnsson and Pálsson, 2008). It covers an area of 925 km^2, has a mean ice thickness of about 200 m and a total volume of ~ 195 km^3 (Björnsson and others, 2006). In the maritime Icelandic climate, snow accumulation is sensitive to winter temperature and the position of the paths of the North Atlantic low pressure weather fronts. As a consequence, the temperate glaciers of Iceland are dynamically active and respond sensitively to climatic fluctuations (Björnsson, 1979). Due to a steeply decreasing precipitation gradient from south to north, south-flowing glaciers tend to be steep and fast flowing, terminating at low altitude in areas of high ablation. Conversely, north-flowing glaciers have lower accumulation in their higher reaches, shallower slopes and terminate in broad fronts at higher altitudes. During the early 20^{th} century there was a general recession of Icelandic glaciers which accelerated after the 1930s and slowed after the 1960s (Björnsson, 1979). Previous studies of the LIC have shown that the southern outlet glacier of Hagafellsjökull Vestri has experienced four separate periods of glacier surging between 1971 and 2002, which affected an area of 150 km^2 (Björnsson and others, 2003).

1.3.5.2. Flade Isblink, eastern North Greenland

Flade Isblink is situated in Kronprins Christian Land in eastern North Greenland on Princess Dagmar Peninsula. With an area of 8 500 km^2, it is the largest independent ice cap in Greenland (Kelly and Lowell, 2009) and has a maximum elevation of ~900 m.

Recent remote sensing studies have provided sparse observations of ice velocity and surface elevation changes. Higgins (1991) used aerial photographs taken between 1961 and 1978 to track features of the FIIC in order calculate mean ice velocity at the 2 fastest flowing glaciers. More recent ICESat elevation observations show a distinct longitudinal gradient in surface elevation change, with the western half of the FIIC having thickened by around 50 cm yr^{-1}, and the eastern half having thinned by around 20 cm yr^{-1} between 2003 and 2007 (Pritchard et al., 2009).

1.3.5.3. Western Greenland Ice Sheet

The central part of the GrIS has been observed to change slowly, but near the coast rapid changes over large areas have been documented. Recent airborne altimeter observations show that the greatest thinning is along fast flowing marine-terminating outlet glaciers where rates exceed 10 m yr^{-1} (Abdalati et al., 2001; Krabill et al., 2004). Satellite laser altimeter observations show that glaciers flowing faster than 100 m yr^{-1} thinned at an average rate of 0.84 m yr^{-1} over the period 2003 to 2007 (Pritchard et al., 2009). Rignot and Kanagaratnam (2006) observed that the 21 largest outlet glaciers accelerated by 57 % between 1996 and 2005. They estimated mass loss due to ice discharge increased by 100 Gt yr^{-1} over the same period, resulting in a 150 % increase of the GrIS's contribution to sea level.

Since thinning rates exceed those expected from changes in surface mass balance alone (Abdalati et al., 2001), the rapid thinning of some GrIS marine-terminating outlet glaciers has been attributed to changes in ice dynamics. For three of the GrIS's largest marine-terminating outlet glaciers - Helheim Glacier; Kangerdlugssuaq Gletscher; and Jakobshavn Isbræ - these changes in ice dynamics are thought to have been caused by perturbations at the calving front due to climate induced thinning of their termini (Abdalati et al., 2001; Howat et al., 2007; Holland et al., 2008).Thinning and breakup of the floating ice tongue of Jakobshavn Isbræ were accompanied by approximate doubling of the ice flow velocity (Thomas et al., 2003; Joughin et al., 2004; Thomas, 2004). Enhanced calving may have removed not-quite-floating ice at Helheim Glacier, reducing restraint on the remaining ice and allowing faster flow (Howat et al., 2005). However, it is not yet clear to what extent calving is responsible for the thinning and acceleration of other GrIS marine-terminating outlet glaciers (Krabill et al., 2004).

An additional mechanism linking climate to ice dynamics has been proposed by Zwally et al. (2002), who suggested that enhanced surface melting caused by climatic warming is affecting ice dynamics directly. Longer and more widespread surface melting may increase drainage to the bed and thus enhance ice flow through basal lubrication. Zwally et al. (2002) showed for one site near the equilibrium line at the western margin of the GrIS that ice velocity increased following the seasonal onset of drainage of surface melted water into the ice sheet, and that greater summertime ice flow acceleration occurred in years with greater melting. Large melt-water ponds (~5 km diameter) form on the ice sheet surface during the melt season which can drain in a matter of hours (Box and Ski, 2007; Das et al., 2008). A large, rapid influx of water to the bed could change the subglacial drainage system, resulting in a reduction in basal friction and subsequent acceleration of the overlying ice (McMillan et al., 2007; Sneed and Hamilton, 2007). In their study, Zwally et al. (2002) estimated total acceleration to be of the order of 10%. Inclusion of this enhanced sliding effect in one model (Parizek and Alley, 2004) altered the ice sheet hypsometry, increasing the sensitivity of the ice sheet to various warming scenarios. The authors suggest that melt-induced thinning may result in a positive-feedback; as the ice sheet surface lowers, it will be exposed to warmer air temperatures and will experience more melting, thereby accelerating the process (Parizek and Alley, 2004).

Uncertainty remains as to whether access of meltwater to the bed would migrate inland with increased melt extent, and whether fast-flowing ice is affected (Alley et al., 2005). McMillan et al., (2007) made observations of supraglacial lakes at the western margin of the GrIS and concluded that lake volume is seasonally driven, culminating in widespread drainage in late summer. Ground-based observations made by Das et al., (2008) confirmed that water drained from supraglacial lakes can and does penetrate through ~1 km thick, cold ice to the bed within as little as 2 hours indicating the potential for supraglacial lakes to provide large volumes water for basal lubrication on short timescales. It is not known whether fast-moving glaciers and ice streams are similarly affected, though outlet glaciers appear to be less sensitive to direct input of meltwater to the bed over longer time periods (Echelmeyer and Harrison, 1990). Seasonally invariant velocity observed at JI has been attributed to deformation of a thick (~300 m) layer of softer, temperate ice at the glacier bed, providing the majority of ice motion, as opposed to basal sliding or a deforming sediment layer (Funk et al., 1994;

Luthi et al., 2002). However, a speedup of 10 - 15 % was observed (Luckman and Murray, 2005) at just below the grounding line of Jakobshavn Isbræ during summer 1995 - a year with unusually high melting (Abdalati and Steffen, 2001) - and has been attributed to melt-induced acceleration. In general, recent summer accelerations of marine-terminating GrIS outlet glaciers represent speedups of less than 15% of their annual mean velocities (Joughin et al., 2008a), though larger accelerations have been observed; Joughin et al., (1996) observed a 7-week speedup of ~300 % at Ryder glacier which coincided with the drainage of several large supraglacial lakes.

Although the idea of widespread enhanced sliding due to the presence of basal water drained from supraglacial lakes appears to have been largely accepted by the scientific community (e.g. Alley et al., 2005; Joughin et al., 2005; Rignot and Kanagaratnam, 2006; Shepherd et al., 2007; Das et al., 2008) it is not without controversy. Van de Wal et al., (2008) used GPS measurements to observe large and rapid velocity fluctuations in the ablation zone at the western margin of the GrIS, apparently due to summertime input of surface water to the bed. The authors did not observe a correlation between annual ablation rate and annual ice velocities which they explain by suggesting that the internal drainage system adjusts to the increased water input so that annual velocities remain roughly constant. Price et al., (2009) suggest that the acceleration of inland ice observed by Zwally et al. (2002) can be explained by longitudinal coupling to thinner marginal ice and that further study is required before the claims of Zwally et al. (2002) are fully warranted. It is clear that an improved understanding the relative importance of calving front retreat and meltwater lubrication on ice dynamics is required to make accurate century-scale predictions of the GrIS.

1.4. Objectives

The discussion above reveals that gaps in our understanding of ice dynamics exist, such as whether access of melt water to the bed would migrate inland if warming caused surface melting to migrate inland. The aim of this thesis is to address some of these gaps and our specific objectives to achieve this aim are:

1. to derive the first ice velocity map of the Langjökull ice cap (LIC), a land-terminating ice cap in Iceland, and to compare these observations with

independent GPS measurements of ice velocity to investigate inter-annual variations in rates of ice flow (Chapter 3).

2. to derive the first ice velocity map of the Flade Isblink ice cap (FIIC), an ice cap in East Northern Greenland drained by a mixture of land- and marine-terminating glaciers, and to investigate seasonal variations in rates of ice flow (Chapter 4).
3. to measure seasonal variations in rates of ice flow at a land-terminating sector of the western GrIS, and to investigate the associated mechanism(s) (Chapter 5).

1.5. Summary

The aim of this work is to assess the utility of InSAR for investigating the physical processes that govern temporal fluctuations in ice motion. Each of the three results Chapters takes the form of a journal article and each varies in length depending upon the journal for which it was written. Where the Chapter has been submitted or published, detail is provided about authorship and publication status. Chapter 3 investigates the use of InSAR techniques for mapping 3D ice flow for land-terminating ice in Iceland. Chapter 4 investigates the use of InSAR for mapping ice elevation and quantifying seasonal ice for both land-terminating and marine terminating outlet glaciers at an ice cap in eastern North Greenland. Chapter 5 presents the use of InSAR for quantifying spatial and temporal ice velocity variations for a land-terminating sector of the GrIS and investigating the forcings behind the observed variations. The objectives outlined above aim to fill gaps in our understanding of processes controlling glacier dynamics in order to reduce the key uncertainties identified by the IPCC AR4 (Solomon et al., 2007).

Chapter 2: InSAR methodology

2.1. Introduction to InSAR

Synthetic Aperture Radar interferometry (InSAR) uses phase differences in backscattered radar signal received at two different points in space to detect centimetre-scale changes in the Earth's surface (Figure 2.1). A major strength of InSAR is its unique ability to provide high-resolution (5 m in azimuth, 9.5 m in slant-range for ERS), near-instantaneous (1 day) measurements over large (10 000 km^2) areas. InSAR was first used to meaure ground movement during the 1992 Landers earthquake in California, USA (Massonnet et al., 1993) and has since been used in the studies of tectonic deformation (e.g. Fialko et al., 2005), fault movement (e.g. Wright et al., 2004), rifting (Wright et al., 2006), volcanic deflation (Massonnet et al., 1995), subsidence (Amelung et al., 1999) and landslides (Hilley et al., 2004).

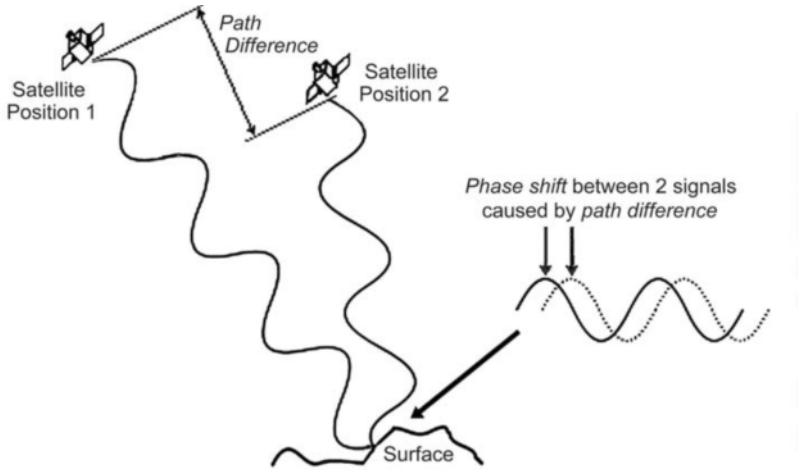

Figure 2.1. Schematic showing phase shift between backscattered signal received at 2 locations caused by the radar path difference. Massom and Lubin (2006).

The first application of InSAR to the study of ice flow was demonstrated by Goldstein et al. (1993), who used the technique to measure ice velocity at an Antarctic ice stream. Their study used repeat-pass data acquired by the European Remote Sensing satellite-1 (ERS-1) which was launched in 1991 by the European Space Agency (ESA). InSAR has led to advances in several important areas of ice sheet research including the measurement of ice discharge rates (Rignot and Kanagaratnam, 2006; Rignot et al., 1997; Joughin et al., 1999a); the detection of outlet glacier grounding lines (Goldstein et

al., 1993; Gray et al., 2002; Rignot, 1996); the estimation of regional mass balance (Rignot and Thomas, 2002); and the monitoring of glacier surges (Joughin et al., 1996a; Strozzi et al., 2000). These studies provide useful datasets for the climate, sea level change and ice modelling communities.

2.2. InSAR background

InSAR techniques utilise the phase component of synthetic aperture radar (SAR) data. A SAR illuminates the Earth with a beam of coherent microwave radiation, and measures the signal backscattered from the surface. The radar wave can be described by its wavelength, amplitude and phase, as shown in figure 2.2. The phase describes the shift of one wave relative to another; radar waves are 'in-phase' if their origins are perfectly superimposable. If one of the two identical waves is then shifted relative to the other along the x-axis until they are superimposed again, it has undergone 1 complete cycle of phase shift corresponding to 360º. Differencing the phase components of two SAR images produces an interferogram. Phase differences between 2 SAR images represent sub-wavelength differences in the round-trip travel time of radar pulses between the satellite and the surface scatterers. These in turn represent extremely precise measures of the change in the length of the path taken by the received signals. Interferograms contain information about the height and motion of scatterers within the illuminated scene.

Successful interferogram generation requires the phase values contained within the constitutive SAR images to be spatially coherent. This interferometric coherence is calculated by correlating the phase values of the SAR image pair within a window (a few pixels in range and azimuth) and it ranges from 0, where there is no useful information in the interferogram; to 1, where there is no noise in the interferogram. Interferometric coherence is affected by the local slope (steeper slopes lead to lower coherence), the properties of the surface being imaged (vegetated or moving surfaces have lower coherence), the interval between acquisitions of constitutive SAR data (longer periods lead to lower coherence), the baseline (larger baselines lead to lower coherence) as well as the method used to form the interferogram. Coherence can be regarded as a measure of the quality of an interferogram.

To obtain the results presented in chapters 3, 4 and 5 of this thesis, I used data acquired

by a repeat-pass, single-antenna SAR system mounted on the polar-orbiting ERS-1/-2 satellites. The ERS satellites are in sun-synchronous retrograde orbits with a nominal repeat period of 35-days. Until the launch of the companion satellite, ERS-2 in 1995, the shortest interferometer acquisition interval was 3-days during the first and second ice mission phases of the ERS-1 mission in 1991/1992 and 1994. This 3-day interval is not sufficiently short to prevent temporal decorrelation due to excessive surface change in the most dynamic areas of ice. Shortly after the launch of ERS-2, the two ERS satellites were manoeuvred into the same orbit, in order to acquire data from the same location on the ground, separated by 1-day. This 'Tandem mission' during 1995 and 1996 provided the most important archive of data for SAR interferometry studies of the cryosphere as interferometric coherence is maintained over most ice areas where data were acquired.

In repeat-pass InSAR studies, two or more SAR images are acquired from the same scattering volume but from slightly different positions in space, separated by a spatial (interferometric) baseline and a temporal baseline. This is achieved by using data acquired by a single satellite SAR on different orbits (e.g. Chapter 3) or by identical instruments on different satellites flying in the same orbit such as the ERS Tandem mission (Chapters 4 and 5). Here I describe the theory and outline the practice of InSAR data processing, from the raw SAR data to the derivation of ice motion and elevation.

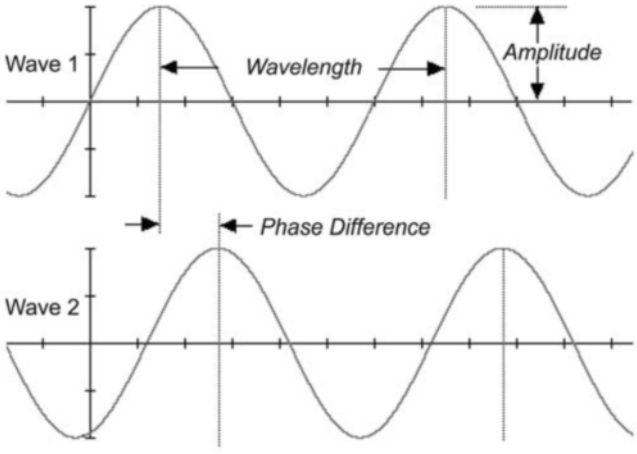

Figure 2.2. A schematic representation of the relationship between the wavelength, amplitude and phase characteristics of electromagnetic radiation. Massom and Lubin (2006).

2.3. InSAR theory

By interfering two SAR images, a measure of the interferometric phase (ϕ) is obtained. ϕ can be regarded as a linear combination of independent contributions due to several terms (Bamler and Hartl, 1998), including imaging geometry (the spheroid-Earth phase) ϕ_0, local topography ϕ_{topo}, surface motion ϕ_{motion}, atmospheric (tropospheric and ionospheric) propagation delays ϕ_{atm} and system noise ϕ_{noise}, where:

$$\phi = \phi_0 + \phi_{topo} + \phi_{motion} + \phi_{atm} + \phi_{noise} \tag{2.1}$$

My study areas are in at high-latitudes where the atmosphere is thinnest, and because the SAR data were acquired at a time of minimal solar activity (Lang, 1999), the atmospheric phase contribution ϕ_{atm} is likely to be a fringe or less. As this is much smaller than the phase contribution due to ice motion ϕ_{motion} (on the the order of 100 fringes for the fastest flowing ice), the ϕ_{atm} component is sufficiently small to be ignored. By selecting interferometric image pairs of suitable coherence, ϕ_{noise} is minimized such that ϕ can be rewritten, after the spheroid-Earth correction is applied, as a function of the topographic- and motion-contributions alone:

$$\phi_{unwrap} = \phi_{topo} + \phi_{motion} \tag{2.2}$$

where ϕ_{unwrap} denotes the unwrapped interferometric phase difference (see section 2.7) achieved by processing to remove the modulo-2π ambiguity (Werner et al., 2000). For repeat-pass interferometry, the range difference between passes, Δ, is estimated by using (Joughin et al., 1998):

$$\Delta = \frac{\lambda}{4\pi}\phi_{unwrap} \tag{2.3}$$

where λ is the radar wavelength. Referring to the geometry of repeat-pass satellite interferometry (Figure 2.3), the interferometer baseline (their separation in space) and

range difference due to topography Δ_{topo} are related by:

$$B_{\perp}\sin\theta_d + B_{\mathrm{II}}\cos\theta_d = -\Delta_{topo} - \frac{\Delta_{topo}^2}{2r_0} + \frac{B^2}{2r_0} \tag{2.4}$$

where $B\perp$ and $B_{\parallel}$ are the normal and parallel components of the baseline B, relative to the radar slant range vector r_0. Applying (2.2) and (2.3), the phase due to topography is solved for as:

$$\begin{aligned}\phi_{topo} &= \frac{4\pi}{\lambda}\left[-r_0 + \sqrt{r_0^2 - 2r_0\left(B_{\perp}\sin\theta_d + B_{\mathrm{II}}\cos\theta_d\right) + B^2}\right] \\ &\approx -\frac{4\pi}{\lambda}\left(B_{\perp}\sin\theta_d + B_{\mathrm{II}}\cos\theta_d - \frac{B^2}{2r_0}\right)\end{aligned} \tag{2.5}$$

The contribution to the phase from surface motion ϕ_{motion} is given by:

$$\phi_{motion} = \frac{4\pi}{\lambda}\left(\Delta_{motion,xs}\sin\varphi - \Delta_{motion,z}\cos\varphi\right) \tag{2.6}$$

where $\Delta_{motion,xs}$ denotes the component of displacement tangiential to the surface of a reference ellipsoid and directed orthogonal to the satellite ground track, $\Delta_{motion,z}$ denotes displacement directed normal to the ellipsoid, and φ denotes the local surface slope (see Figure 2.3). For steady motion during the interferogram acquisition interval, the phase is related to the surface velocity by:

$$\phi_{motion} = \frac{4\pi}{\lambda}\left[\delta T\left(v_{xs}\sin\varphi - v_z\cos\varphi\right)\right] \tag{2.7}$$

where δT is the time interval between acquisition of images, v_{xs} is the across-track component of velocity and v_z is the component of velocity directed normal to the ellipsoid.

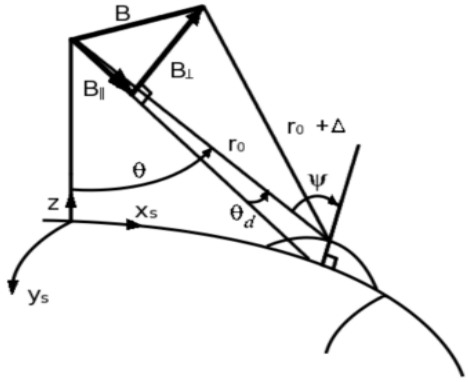

Figure 2.3. Schematic showing repeat-pass InSAR geometry (after Joughin et al., 1998).

It is possible to form interferograms using 2, 3 or 4 satellite passes, though 2-pass InSAR requires independent knowledge of the topography within the scene to isolate the motion field (see chapter 3). In 3-pass and 4-pass (or double-differencing) InSAR, separation of the topographic and motion terms using only SAR data may be achieved (e.g. Rignot, 1998). The procedure involves differencing two interferograms of differing spatial baselines but identical temporal baselines, in order to cancel the phase contribution from surface motion and therefore isolate the phase contribution from topography. This method relies on the assumption that surface motion is the same during each of the acquisition intervals. Chapters 4 and 5 of this thesis utilize 4-pass InSAR, which is explained in detail below. Equation 2.2 shows that the unwrapped interferometric phase ϕ_{unwrap} contains contributions from both topography and motion toward or away from the sensor in the SAR line-of-sight (LOS) (Joughin et al., 1996c). The phase from two interferograms from four passes (1, 2, 3 and 4) can be written:

$$\Delta\phi_{12} = \frac{4\pi}{\lambda}\left[B_{12}\sin\left(\theta - \alpha_{12}\right) + v\delta T \cdot r_0\right] \tag{2.8}$$

and

$$\Delta\phi_{34} = \frac{4\pi}{\lambda}\left[B_{34}\sin\left(\theta - \alpha_{34}\right) + v\delta T \cdot r_0\right] \tag{2.9}$$

where α is the tilt of the baseline with respect to the horizontal. As the duration of observation δT is also equal for both acquisitions, the phase due to motion, $(4\pi/\lambda)v\delta T \cdot r_0$, is a constant and differencing the two interferograms yields a single interferogram with

the phase contribution of the displacement field to the phase removed:

$$\begin{aligned}\Delta\phi_{12-34} &= \Delta\phi_{12} - \Delta\phi_{34} \\ &= \frac{4\pi}{\lambda}\left[B_{12}\sin(\theta - \alpha_{12}) - B_{34}\sin(\theta - \alpha_{34})\right]\end{aligned} \tag{2.10}$$

The interferometric sensitivity to the variation in ice sheet topography now depends on the difference between the two interferometer baselines B_{12} and B_{34}. To form a differential interferogram with high sensitivity to topography, the difference between B_{12} and B_{34} should be large. This topography-only interferogram can then be scaled to the appropriate baseline length and subtracted from the remaining interferograms in order to isolate the phase contribution due to ice motion. Assuming that ice flows parallel to the surface and in the direction of steepest slope (Paterson, 1994), the motion-phase (ϕ_{motion}) can be used to estimate the relative ice velocity (e.g. Kwok and Fahnestock, 1996).

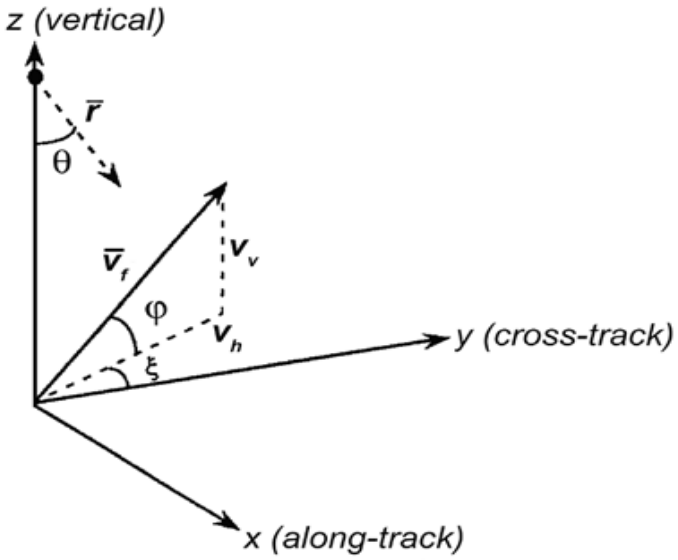

Figure 2.4. Schematic showing the effect of surface relief on observed LOS velocity (Kwok and Fahnestock, 1996).

In order to isolate phase due to displacement, the topography-only interferogram, $\Delta\phi_{12\text{-}34}$, is subtracted from the original mixed interferogram e.g.:

$$\Delta\phi_{34} - k\Delta\phi_{12-34} = 2kv\delta T \cdot r_0 \tag{2.11}$$

where k is the factor scaling the $B_{12\text{-}34}$ fringe pattern into that of the B_{12} interferogram

which is essential to compensate for the difference in sensitivity to topography due to the different spatial baselines.

The LOS displacement measured by InSAR is a function of the radar look angle θ, the surface slope φ and the angle (in the *x*-*y*-plane) formed between the look direction projected onto the *x*-*y*-plane and in the ice flow direction ξ (Kwok and Fahnestock, 1996)(see Figure 2.4). From this geometry, the component of the ice surface velocity vector in the radar LOS (slant range) direction V_r is given by:

$$V_r = \frac{\phi\lambda}{4\pi\delta T} + V_0 \sin\theta \cos\xi \tag{2.12}$$

where V_0 is the spatially constant component of the surface velocity. The first term is based on the satellite-derived difference due to ice-surface displacement between image acquisitions, and represents the spatial variability in velocity. This is a relative rather than absolute velocity as it includes no spatially constant velocity. The absolute displacement offset is typically estimated using ground control points (GCPs) (Joughin et al., 1998). The second term is analogous to a baseline velocity, with sine and cosine functions projecting the constant ice surface velocity into the direction of the radar LOS. The ice surface velocity in the direction of actual flow V_f can then be written (Kwok and Fahnestock, 1996):

$$V_f = \frac{V_r}{\cos\xi \cos\varphi \sin\theta - \cos\theta \sin\varphi} \tag{2.13}$$

As the measurement of velocity requires observations at two or more points (i.e. from two or more look-directions), the radar look angle θ and the angle between the radar look and actual ice flow direction ξ change with one measurement of V_f In the above relationships, the surface slope is taken to be in the direction of flow, with the implicit assumption that the flow vector is tangential to the surface topography. $V_v = V_f \sin\varphi$ and $V_h = V_f \cos\varphi$ are the vertical and horizontal components, respectively, of the velocity vector in the flow direction (Figure2.4), and both are present in the InSAR-derived ice motion. The fact that a repeat-pass interferometer is sensitive to surface displacement directed along the LOS only (Joughin et al., 1998) has the effect of emphasizing vertical

relative to horizontal displacement (Joughin et al., 1995). As a result, it is not possible to unambiguously separate the mixed vertical and horizontal displacement signals in the interferogram without additional information or assumptions (Joughin et al., 1998).

2.3.1. Retrieval of three-dimensional velocity vectors

A limiting factor for InSAR observations from a single-orbit track is that they yield velocity in the radar LOS only (Goldstein et al., 1993; Joughin et al., 1996c; Rignot, 1996). However, knowledge of the full three-dimensional (3D) flow pattern is desirable for ice-dynamics studies and the validation of ice-flow models. Additional steps are necessary to isolate the vertical and horizontal components of the velocity vector. For interferograms formed from data acquired in one look-direction, the two-dimensional flow field is typically constructed by assuming that the ice is is steady state and that horizontal flow component occurs in the direction of maximum downhill surface slope as averaged over 10 - 20 ice thicknesses (Joughin et al., 1996c, Joughin et al., 1998a; Paterson, 1994). While this assumption holds for large regions of the ice-sheet interior (Paterson, 1994), the assumption that ice flows in the direction of steepest slope can break-down near the margins. If both ascending- and descending-pass orbit data are available, the 3D flow pattern can be derived from InSAR measurements from these two different look directions (Joughin et al., 1998; Mohr et al,. 1998; Chapter 3). This technique is particularly valuable in regions where the direction of ice flow deviates from the regional slope aspect. Following Joughin et al., (1998), ice velocity in the horizontal (x, y) and vertical (z) directions can be expressed as:

$$v = v_x \hat{x} + v_y \hat{x} + v_z \hat{z} = v_h + v_z \hat{z} \tag{2.14}$$

If we make the assumption that surface ice is constrained to flow parallel to the ice surface $z_t(x, y)$, then vertical velocity is related to horizontal velocity by:

$$v_z = \left[\nabla_{xy} z_t(x, y)\right]^T v_h \tag{2.15}$$

Substituting this expression into (14) yields

$$v = v_h + \left[\nabla_{xy} z_t(x,y)\right]^T v_h \hat{z} \tag{2.16}$$

Which allows the velocity vector to be determined using observations from ascending- and descending-pass satellite data when the surface slope is known.

2.4. Selection of suitable raw SAR data

Consideration of the interferometric baseline and time interval between the pair of SAR acquisitions is required for optimal raw data selection. Not only does the baseline length $B\perp$ (see figure 2.2) play a key role in interferometric geometry and the successful generation of an interferogram, it also serves as a measure of both the quality and the suitability of the SAR image pairs for a given application. Equally important is the temporal baseline δT, in that scatterers must remain coherent for InSAR to work. The optimal combination of spatial and temporal baselines depends on the application; for topographic mapping, errors are minimised by selecting image pairs with large baselines $B\perp$ (Mohr and Madsen 1996), while for ice motion mapping, $B\perp$ should be as small as possible to minimise errors due to unmodeled topography (Joughin et al., 1996a). Increasing the temporal baseline δT will decrease the relative error in ice motion retrievals but will decrease the likelihood that the assumption of steady flow is valid. In addition, increasing the temporal baseline will increase the likelihood of temporal decorrelation for both height and motion retreivals. Longer temporal baselines are better suited to regions of slow-moving ice, while short temporal baselines are necessary for the study of fast outlet glaciers. For differential InSAR using SAR data only, short- and long-baseline SAR image pairs are required for accurate retrieval of both motion and ice surface elevation, as demonstrated in Chapters 4 and 5. When using an independently derived DEM as demonstrated in Chapter 3, the criticality of the perpendicular baseline $B\perp$ depends on the resolution of the DEM used to isolate motion – the coarser the DEM, the smaller $B\perp$ needs to be.

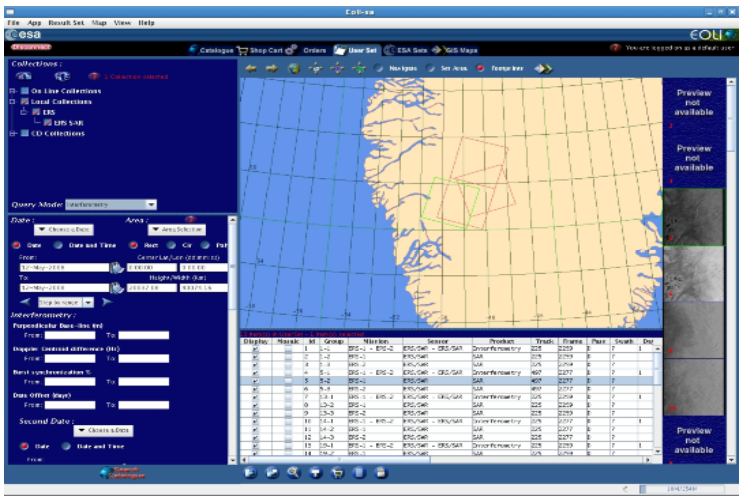

Figure 2.5. Eoli-SA data selection screen

A number of online software packages have been developed to facilitate the selection of suitable raw data. We use the ESA-developed Eoli-sa software (www.eolisa.esa.int), which enables the user to asses the quality of the SAR multi-looked intensity image as shown in Fig. 2.5.

2.5. SAR processing

We use commercial software developed by Gamma Remote Sensing (Gamma) to process raw SAR data to estimate ice velocity and elevation (Werner et al., 2000). The first step when processing raw SAR data to Single-Look Complex (SLC) data with Gamma's modular SAR processor (MSP) is to create a MSP parameter file. This is created from the leader file supplied with the raw data using *ERS_proc* and contains the parameters used in the raw to SLC processing chain. Raw ERS SAR data often suffers from missing lines due to incomplete data transmission. If only a few lines are missing, it is almost impossible to tell by visual inspection of the multi-look intensity image produced. For interferometry, a single missing line will result in decorrelation between images. This problem can be corrected by replacing missing lines with null values using the procedure *ERS_fix*. This routine can also be used to concatenate adjacent data frames to form a single strip of data.

The position and velocity of a satellite in its orbit are given by orbit-state vectors. Precise orbit information is provided by the Department of Earth Observation and Space Systems (DEOS) at the Technical University of Delft (Scharroo and Visser, 1998). The

Gamma routine *DELFT_proc2* extracts and interpolates the state vectors to update the MSP parameter file state vectors.

The remainder of the processing chain from raw SAR data to SLC format is shown schematically in figure 2.6 and described in detail by in Appendix A.

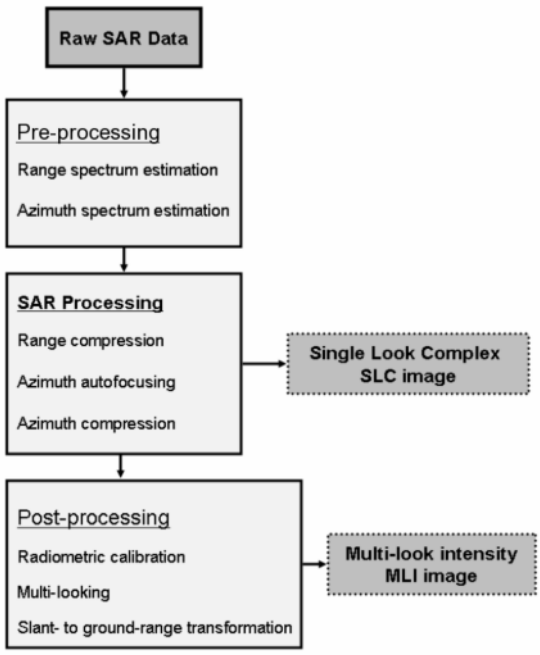

Figure 2.6. Schematic of pre-processing steps for the Gamma modular SAR processor (MSP). Gamma (2008).

2.6. Interferometric processing

Once two suitable SAR scenes are processed to SLC, the interferometric processing can begin. Figure 2.7 shows a schematic represenation of the sequence of processing steps taken when forming a DEM using Gamma's Interferometric SAR processor (ISP).

A key step in InSAR processing is the precise co-registration of both the intensity and phase of the input images prior to interferogram generation (Gens and Van Genderen, 1996; Massonet and Rabaute, 1993). Co-registration involves the geometric alignment of the secondary image to the primary reference image. Accurate co-registation requires knowledge of the offset between the two scenes, such that the secondary can be

superimposed onto the primary, while maintaining the phase content of the pixels. Image offsets occur as a result of uncertainty in sensor location, differences in the look angles between repeat passes and diverging or converging orbits (Kwok and Fahenstock, 1996). Co-registration is generally carried out in 2 stages – the first involves coarse matching to within a few pixels using precision satellite state-vector data (Gens and van Genderen, 1996). Coarse matching is followed by fine co-registration, whereby the image alignment is refined to within a fraction of a pixel, typically by comparing roughly corresponding areas and solving for a set of local transformation parameters (Massonet and Feigl, 1998)

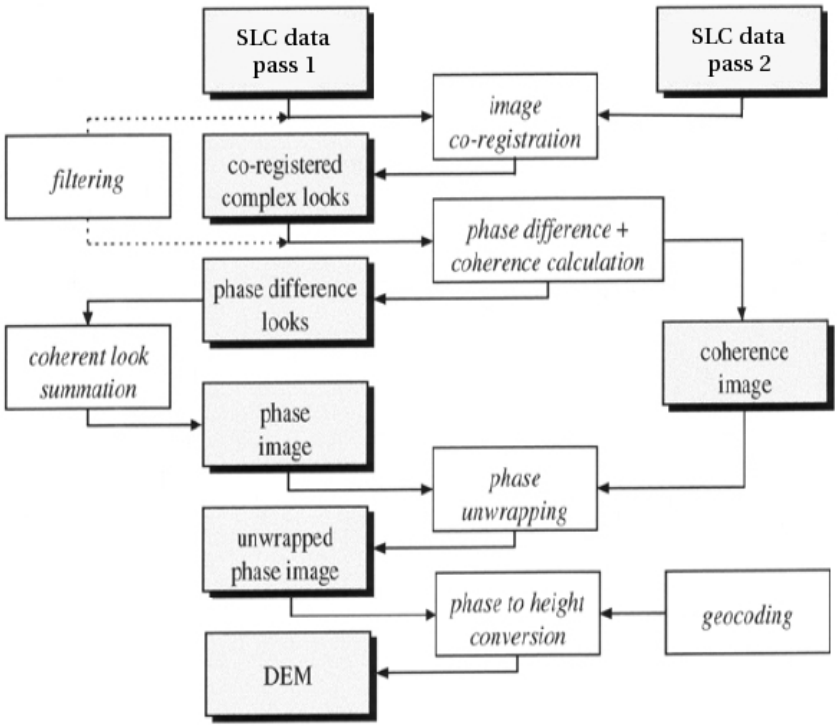

Figure 2.7. Schematic showing Gamma Interferometric SAR processing (ISP) steps to form an InSAR DEM.

2.6.1. Generation of offset parameter file.

In the same way that the MSP SLC parameter file contains all information concerning a SAR image, interferometric products are accompanied by a parameter file containing information on the co-registration of the SLC pair and parameters used or determined during the processing.

2.6.2. Estimation of offsets

The calculation of the offsets is based on the local spatial correlation function for a number of small areas throughout the image. The image offsets which maximise the local correlation can be determined either by cross correlation of the image intensity or by optimisation of the fringe visibility. Computed offsets are then used to define the coefficients of the polynomial for the transformation between the secondary and reference geometry. Initial offsets help in guiding the precise estimation of offsets and are calculated from the orbit parameters using *init_offset_orbit*. This routine estimates a constant offset and does not take into account variations in offset across the image. To calculate the precise offset estimates, the *offset_pwr* routine is used. This procedure divides each of the intensity images into patches of user-defined size in which range and azimuth offsets are estimated. In order for the algorithm to work, there must be sufficient contrast within the local estimation window. The local estimates of the offsets computed during the previous stage are then used to estimate coefficients of an offset polynomial for the whole image using the routine *offset_fit*. This program generates polynomial models of range and azimuth offsets using linear least-squares, rejecting offsets far from the initial fit in order to iteratively improve the coefficients. A higher number of offsets above the signal-to-noise ratio (SNR) can sometimes be achieved by running *offset_pwr* and *offset_fit* iteratively.

2.6.3. Resampling of the secondary image

Once the offset functions are known, the 2 SLC images can be co-registered by resampling the slave image using *interp_cpx*. After its parameters have been determined, the transformation is applied to the secondary image. Pixel values must be interpolated in order to attain the new value according to the transformation applied (Usai, 2001).

2.6.4. Baseline estimation

It is necessary to have an estimate of the baseline separation for the pair of SLC images, which can be obtained from the orbital parameters using *base_orbit*. The perpendicular baseline can be estimated using *base_perp*. *Base_orbit* produces an baseline estimate accurate enough to proceed with interferometric processing though a more accurate estimate can be obtained using *base_ls*. However, this procedure estimates the baseline using phase values at the locations of GCPs, so can only be performed after

interferogram generation.

2.6.5. Interferogram generation

After co-registration, the complex interferogram is formed by multiplying each complex pixel of the primary image by the complex conjugate of the corresponding pixel in the secondary image using the routine *interf_SLC*. This operation can be expressed in polar notation as:

$$r_1 e^{i\phi_1} \cdot r_2 e^{-i\phi_2} = r_1 r_2 e^{\phi_1 - \phi_2} \tag{2.17}$$

The resulting interferogram contains the product of the magnitudes ($r_1 r_2$) and the phase difference (ϕ_1 - ϕ_2) at each pixel of the primary and secondary images. The phase differences are represented by coloured 'fringes' and are a measure of the combined surface elevation and displacement in the radar LOS, as well as any errors. An example of an uncorrected, wrapped interferogram is shown in Figure 2.8.

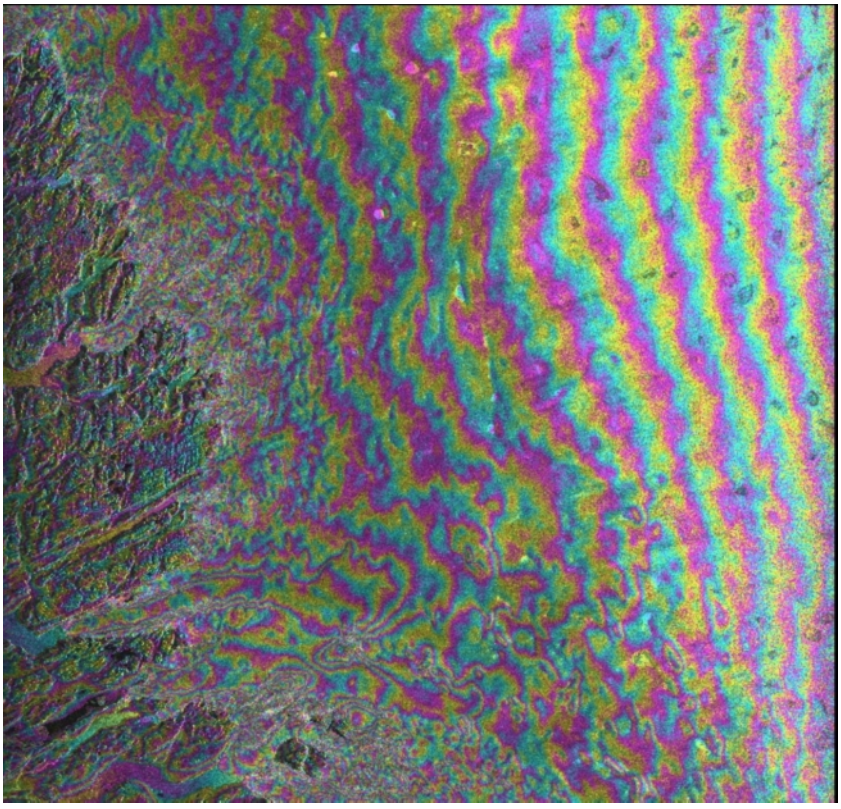

Figure 2.8. Wrapped interferogram (colour) showing fringes due to topography and ice motion over a SAR amplitude image (greyscale). Ice-free areas can be seen at the left

side of the image.

In the interferogram, a phase shift of one wavelength (5.6 cm for ERS) corresponds to half a wavelength of range displacement (due to the two-way journey of the radar signal). In the case of minimal surface relief or a near-zero baseline spatial baseline, each fringe can be converted directly to relative horizontal surface displacement. However, this is rarely the case and topography must be separated from displacement using double-differencing as described in section 2.3.

After multiplication, the resultant interferometric phase product is typically 'multi-looked'. By this process, the values of the phase of neighbouring pixels within a fixed window size are averaged. Multi-looking is an important step in facilitating the subsequent phase unwrapping as it reduces speckle, which degrades the phase measurement (Joughin and Winebrenner, 1994; Wegmuller et al., 2002). Multi-looking not only improves the SNR but also improves computational efficiency by creating smaller, more manageable data files. The disadvantage of multi-looking is that it results in degraded spatial resolution (to around 30 m using our method). Another limitation relates to possible under-sampling in cases where relatively high phase gradients are present. As such, multi-looking is more appropriate for smooth phase surfaces such as ice sheet interior regions (Wegmuller et al., 2002).

2.6.6. Spheroid-Earth phase removal and filtering

As shown in equation (2.1), the complex interferogram consists of several contributions. The flattening operation removes azimuth and range phase trends arising from Earth's curvature and the image pair baseline (ϕ_0) using *ph_slope_base.*

An adaptive filtering routine, *adf*, is typically used to reduce phase noise in order to optimise coherence (Kwok and Fahenstock, 1996; Wegmuller et al., 2002). This routine applies a nonlinear filter based upon the power spectrum to the data. For phase unwrapping it is necessary to have an estimate of the local fringe quality after filtering. Because of the degree of filtering varies over the image, *adf* estimates the local phase standard deviation after filtering and converts this to an effective correlation. The technique is presented in detail by Werner and Goldstein (1997). Flattened

interferograms are typically filtered with a window size of 32 then again with a window size of 8, though the optimal window size depends on the local terrain. When successful, filtering also results in a large reduction in the number of residues (see section 2.7), which can significantly reduce the complexity and increase the efficiency of phase unwrapping (Wegmuller et al., 2002). Disadvantages of filtering are that fringes can be lost in areas of high phase gradients such as shear margins, and phase discontinuities can be introduced in areas of layover, both of which which can lead to errors in phase unwrapping (Wegmuller et al., 2002).

Interferometric coherence is equal to the magnitude of cross-product of the two co-registered SLCs and is a fundamental measure of the quality of phase correlation in the resulting interferogram. The routine *cc_wave* can be used to calculate coherence or it can be generated when applying the *adf* routine.

2.7. Phase unwrapping

The complex interferograms produced by *interf_SLC*, contain 'wrapped' interferometric phase in modulo-2π format. To achieve unique values of phase, it is necessary to add the correct integer number of phase cycles to each sample. The process of solving this 2π ambiguity and recovering continuous phase information from the discrete wrapped phase is known as phase unwrapping. Where the phase field is simple and smooth, phase differences between adjacent samples lie within -π and +π and no discontinuities exist. Under these circumstances, the unwrapped phase can be obtained by a path-independent integration of the phase gradients over the entire dataset, starting from a reference location and with the assumption that all phase differences are in the interval –π to +π (Werner et al., 2002). In practice, phase discontinuities or local errors in the measured phase occur in areas of layover or discontinuous surface deformation, for example at ice/rock interfaces (Werner et al,. 2002). While flat areas of moderate or high coherence present few problems, a more considered approach is required when unwrapping areas of rugged terrain or low coherence. An example of an unwrapped interferogram and corresponding flag file can be seen in Fig. 2.9.

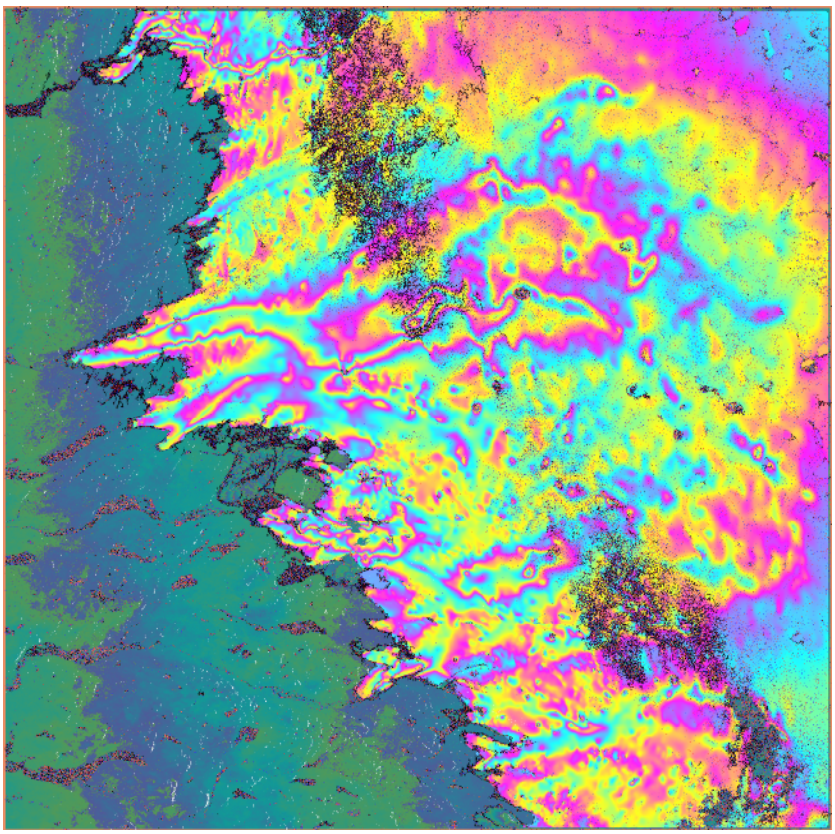

Figure 2.9. Phase unwrapped interferogram (colours) and flag file (greyscale) showing branch cuts and areas of low coherence. A phase ramp due to error in the baseline estimate can be seen at the left side of the image.

Using the Gamma ISP, we implement a 'branch-cut' region growing algorithm to perform the phase unwrapping as described by Rosen et al. (1994). The first step in this procedure is to mask areas of low coherence using the *corr_flag* routine. This routine generates a flag file which is updated by subsequent routines and which is used to unwrap the complex interferogram. 'Neutrons' occur when a pixel intensity is much greater than the average image intensity and help to guide the generation of phase unwrapping trees. The program *neutron* identifies neutrons from the intensity image, and adds their locations to the flag file. Inconsistencies in phase are identified using *residue*, which appends the locations to the flag file. Branch cuts are locations at which phase discontinuities due to layover are identified. To generate the branch cut structure, the program *tree_gzw* is used. This program uses the low-correlation areas, neutrons and residues contained within the flag file to construct the tree-like structure of branch cuts, which are added to the flag file. To implement phase unwrapping, the routine *grasses* uses the branch cuts in the flag file to guide the growth of continuous phase regions from a user defined starting point. We typically initiate phase unwrapping at an ice

divide or other topographic high point, and set the phase to zero at that location.

2.8. Baseline improvement

The quality of an InSAR-derived velocity or height map depends on the accuracy of the baseline estimate. The radial and across-track components of the positions of the SAR sensors at the time of data acquisition are known to within 5 cm and 20 – 30 cm respectively. This uncertainty leads to errors in the estimate of the interferometer (perpendicular) baseline, which introduces an erroneous phase ramp in the final velocity/topography solution, as well as a smaller topographic error.

A refined baseline can be estimated using a least squares fit to GCPs of known height or velocity. A text file containing the GCPs is generated using *gcp_ras*, which takes in a raster image of SAR backscatter intensity or interferometric phase. Best results are achieved by using at least 50 GCPs distributed as widely as possible across the image, preferably in areas of low slope. The interferometric phase corresponding to each GCP can then be calculated using *gcp_phase*. The least squares estimate of the interferometric is obtained by using the program *base_ls*. The procedure may not perform as desired due to inaccurate initial baseline estimate or poor selection of GCPs. Baseline corrections are typically less than 1 m.

2.9. Conversion of phase to height or motion

When forming an InSAR DEM, the unwrapped interferometric phase together with the precision baseline estimate is used to derive the topographic heights using the program *hgt_map*. In the case of velocity map generation, the isolated displacement phase can be converted to displacement in metres using the program *dispmap*. Using this routine, phase is converted to displacement and output in the horizontal, vertical or radar LOS directions.

The program *dispmap_vec* calculates the 3D displacement field based on the LOS displacement component and the ice flow direction calculated from the DEM smoothed over 10 - 20 ice thicknesses using *dem_gradient*. The routine *look_vector* is required to calculate the local radar LOS at each interferogram pixel. The output displacement field

of *dispmap_vec* is expressed as the normal vector, elevation angle and orientation angle, or though northing, easting and vertical components. The program *dispmap_vec2* is used with ascending- and descending-pass data to derive the full 3D velocity vectors, assuming surface parallel flow.

2.10. Interferogram geocoding

The geometrically calibrated interferogram consists of an array of pixels projected in a geometry corresponding to the acquisition parameters of the satellite. For the InSAR data to be compared with other datasets such as GPS or altimetry measurements, they must first be geocoded. The process involves assigning image pixels with ground coordinates and the subsequent transformation into a map projection.

We geocoded our InSAR-derived height maps with the Gamma routine *gc_insar*. This takes projection parameters from the DEM parameter file created using *create_dem_par* and orbital data contained in the ISP parameter files to generate a 'lookup table' containing slant range and corresponding map coordinates for each pixel. The routine *geocode* uses this lookup table to perform the coordinate transformation, while *geocode_back* is used to perform the reverse procedure. An example of a geocoded InSAR-derived DEM is shown in Figure 2.10.

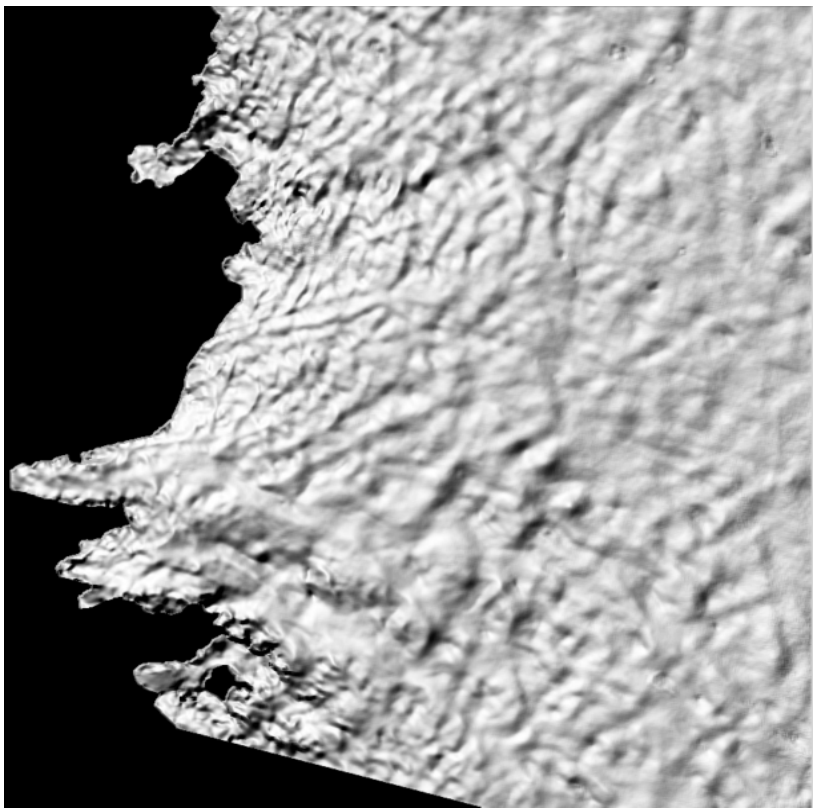

Figure 2.10. Vertically exaggerated shaded relief image of an InSAR-derived elevation model.

2.11. Removal of topographic phase

When the InSAR-derived DEM has been geocoded and calibrated to absolute values, it can be used to remove the topographic phase contribution from other interferograms where coverage overlaps using the method shown schematically in Figure 2.11. The DEM and complex inteferogram must be co-registered in slant range geometry; *interp_cpx* is used to transpose the interferogram into the geometry of the reference interferogram used to form the DEM while *geocode*_back is used to transform the map-projected DEM into the original slant range geometry. Topographic phase can then be simulated using the baseline information of the complex interferogram and the DEM in slant range using *phase_sim*. *Sub_phase* is used to remove the simulated topographic phase in order to isolate phase due to motion. The standard phase unwrapping, baseline improvement, conversion to velocity and geocoding routines described in the previous sections are then used to form geocoded velocity maps. GCPs of known velocity are required to derive absolute velocity measurements as dicussed in section 2.3. Widely distributed points of zero ice motion such as ice divides are typically used. It is possible to use independent point estimates of velocity, for example from GPS, though an

additional assumption of invariant flow over the time interval separating the InSAR and velocity control datasets is required.

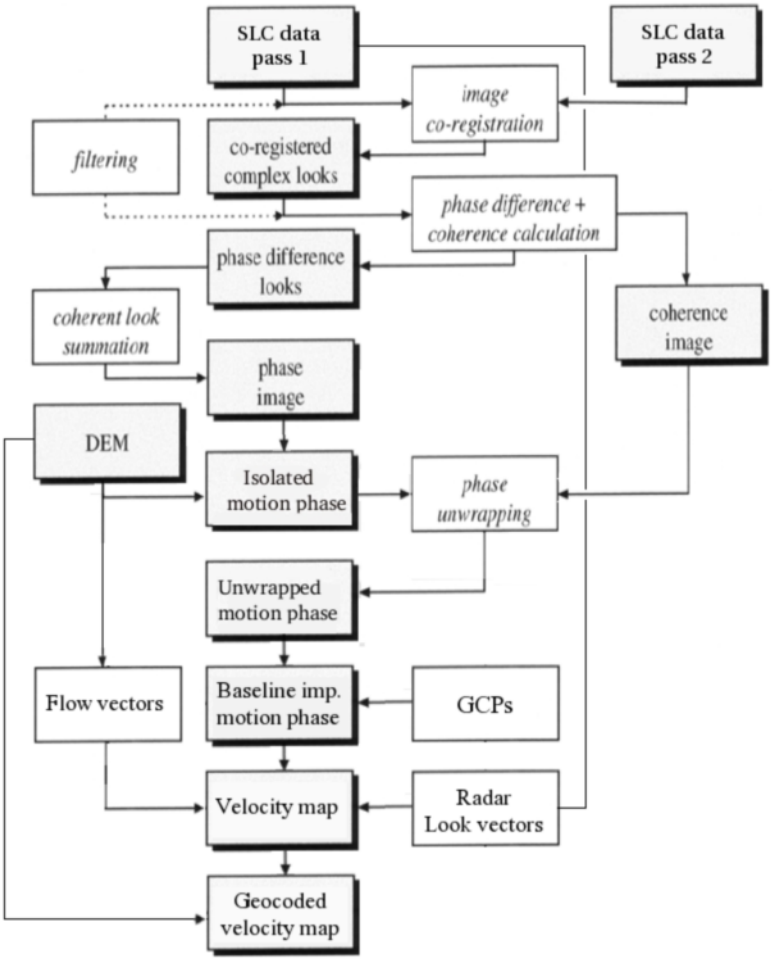

Figure 2.11. Schematic diagram showing steps taken to form a geocoded velocity map using the Gamma ISP.

Chapter 3: Ice velocity measurements of Langjökull, Iceland from InSAR.

This chapter describes the application of repeat-pass InSAR techniques from two look-directions in order to derive full 3D velocity vectors for the second largest ice cap in Iceland. This chapter has been published in Journal of Glaciology:

Palmer, S.J., Shepherd, A., Pálsson, F Björnsson, H, (2009), Ice velocity measurements of Langjökull, Iceland from InSAR. *Journal of Glaciology.*

I processed the InSAR velocity data, interpreted the results and wrote the manuscript. Shepherd assisted with the data processing, interpretation and formulation of the manuscript. Björnsson and Pálsson collected the GPS velocity and elevation data and constructed the DEM. Pálsson also contributed to the writing of the manuscript.

3.1. Abstract

We have computed the velocity of the Langjökull Ice Cap (LIC), Iceland, using interferometric synthetic aperture radar (InSAR) data acquired by the European Remote Sensing (ERS) satellite in 1994 and an ice surface elevation model derived from a GPS survey conducted in 1997. The velocity map covers 68 % of the 925 km^2 of the LIC. Eight principal outlet glaciers were identified, along which ice velocities increased from zero at the ice divide to a maximum of 75 m yr^{-1}. When the InSAR velocity dataset is compared to surface GPS measurements of ice flow determined in summer 2001 there is generally good agreement, suggesting inter-annual and seasonal stability for much of the ice cap during this period. However, non-zero ice velocities at the termini of 4 of the 8 glaciers surveyed suggest that these glaciers were advancing in 1994. Comparison of our GPS and InSAR velocities suggest that Sudurjökull experienced elevated velocity in late February 1994, which when other studies are considered, appears to be consistent with a glacier surge.

3.2. Introduction

At the end of the 20th century, the mass loss of glaciers and ice caps (excluding those of Antarctica and Greenland) is estimated to have formed the largest cryospheric component of the observed sea level rise of 3.1 ± 0.7 mm yr^{-1} (Lemke and others, 2007). Estimates of the 21st century sea level contribution due to glaciers and ice caps vary by a factor of two (Raper and Braithwaite, 2006; Meehl and others, 2007; van de Wal and Wild, 2001) depending on how the sensitivity of ice mass balance to future climate forcing is modelled. Because ice velocity is a factor in the estimation of glacier mass balance, knowledge of its seasonal and inter-annual variability is important to gain an improved understanding of the response of glaciers and ice caps to expected climate change.

About 11 % (11,200 km^2) of Iceland is covered by temperate ice (Figure 3.1), comprising roughly 4 % of the 272,200 km^2 of Arctic land-ice outside of Greenland (Dowdeswell et al., 1997). In the maritime Icelandic climate, snow accumulation is sensitive to winter temperature and the position of the paths of the North Atlantic low pressure weather fronts. As a consequence, the temperate glaciers of Iceland are

dynamically active and respond sensitively to climatic fluctuations (Björnsson, 1979). On the highest parts of the main ice caps, average annual temperatures are below freezing. Due to a steeply decreasing precipitation gradient from south to north, south-flowing glaciers tend to be steep and fast flowing, terminating at low altitude in areas of high ablation. Conversely, north-flowing glaciers have lower accumulation in their higher reaches, shallower slopes and terminate in broad fronts at higher altitudes. During the early 20th century there was a general recession of Icelandic glaciers which accelerated after the 1930s and slowed after the 1960s (Björnsson, 1979).

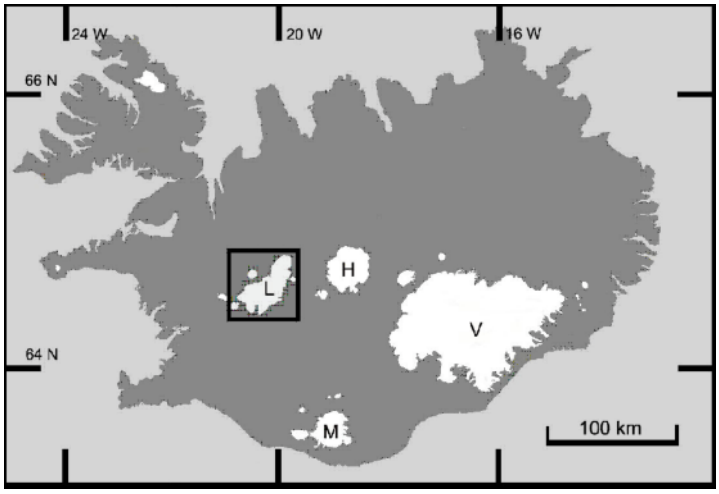

Figure 3.1. Location of Langjökull and other major ice caps in Iceland. Langjökull (L), Vatnajökull (V), Hofsjökull (H) and Myrdalsjökull (M).

With an area of 925 km^2, Langjökull is Iceland's second largest ice cap (Björnsson and Pálsson, 2008). Radio echo sounding has revealed a mean ice thickness of about 200 m and a maximum of 580 m (Björnsson et al., 2006). Total ice volume is estimated to be 195 km^3, which is equivalent to 0.5 mm of eustatic sea level rise (SLR). The southern outlet glacier of Hagafellsjökull Vestri flows down to an altitude of 500 m and following at least 40 years of quiescence, has experienced four separate periods of glacier surging between 1971 and 2002 affecting an area of 150 km^2 (Björnsson et al., 2003). The surface mass balance of Langjökull Ice Cap (LIC) has been measured at 22 stake locations since 1996. The net surface mass balance was negative from 1996-2001, resulting in a loss of 5.36 km^3 of ice or 3 % of the total ice cap mass. Although there is no simple relationship to explain the observed mass loss, the minimum winter surface mass balance in 2001 coincided with a precipitation minimum recorded at a nearby meteorological station (Hveravellir) and, in consequence, it would appear to have

meteorological origins (Björnsson et al., 2002).

In this study, we use interferometric synthetic aperture radar (InSAR) to determine the velocity of the LIC in 1994 and ground-based global positioning satellite (GPS) observations made in 2001 to investigate the extent to which velocity fluctuations may be responsible for recent mass trends.

3.3. Methods

A repeat-pass interferogram calculated from synthetic aperture radar (SAR) data records surface motion within the data repeat interval (Goldstein et al., 1993). If the perpendicular component of distance between sensor positions of the repeat pass data is non-zero, there is an additional topographic contribution to the interferometric phase which can be removed to isolate the motion contribution (Kwok and Fahnestock, 1996). A single interferogram measures only the component of motion in the satellite line of sight (LOS), orthogonal to the flight path. To estimate surface motion in three dimensions, interferograms from ascending and descending satellite orbits can be combined with the additional assumption of ice motion parallel to the ice surface (Joughin et al., 1998). In general ice does not flow parallel to the surface, instead, ice flow is inclined slightly upwards in the ablation zone and slightly downward in the accumulation zone (Paterson, 1994). For LIC, where slopes are low and both accumulation and ablation are modest, the assumption of surface parallel flow should not yield significant errors in estimates of vertical motion. Estimates of horizontal components of motion should be relatively unaffected by deviations from surface parallel flow because the SAR look direction is close to nadir (~24º) and because surface gradients of the LIC are low. In the absence of SAR data acquired from separate orbits, the ice flow direction can be estimated from the direction of maximum averaged (over an area with a radius of 10-20 times the ice thickness) downhill slope (Paterson, 1994).

Repeat-pass interferograms were derived from pairs of European Remote Sensing satellite-1 SAR images obtained from satellite passes sequentially 3 days apart in late February 1994 (Table 3.1). Data were acquired from both ascending and descending satellite orbits, providing InSAR data oriented in approximately orthogonal directions.

The SAR scenes were co-registered to sub-pixel accuracy using a cross-correlation of the detected single look complex data (Wegmüller et al., 1998). We removed the "spheroid-Earth" component arising from the Earth's curvature using precise orbit information (Scharroo and Visser, 1998). The phase-contribution due to topography was removed by subtracting a synthetic interferogram (Massonet and Rabaute, 1993) generated from a digital elevation model (DEM) of the LIC. This external DEM was constructed from a GPS survey conducted in April 1997, with values in the horizontal axes equally spaced every 200m and an estimated vertical accuracy of 2 - 5 m. After accounting for these topographic signals, the phase due to motion during the repeat-pass interval was unwrapped (Wegmüller et al., 1998) and from this we generated ice displacement maps in both ascending and descending geometries.

Satellite heading	Image dates	Satellite orbits	Interferogram perpendicular baseline (m)	Interferogram temporal baseline (days)
Descending	22/02/1994 25/02/1994	13625 13668	140	3
Ascending	24/02/1994 27/02/1994	13660 13703	80	3

Table 3.1. ERS SAR data used in this Chapter.

The LIC displacement maps formed from InSAR data acquired in ascending and descending satellite orbits were then combined with the surface DEM to derive the 3D surface-parallel ice velocity vector field for about 50 % of the ice cap (Figure 3.2). Ice velocity errors in areas with dual-look InSAR coverage were about 5 m yr^{-1} as estimated from the range of ice velocity values measured for stationary bedrock (RMS value is 4.5 m yr^{-1}). To improve spatial coverage, however, we augmented the 3D velocity field with estimates of ice motion derived from single-look InSAR displacement fields in other areas, excluding data for which the angle between sensor look direction and local aspect was greater than 72 degrees. This procedure introduced an additional error due to uncertainties in the ice flow direction, which we estimate to be ± 5 degrees. As the

southern part of the LIC was not covered by ascending-pass data, ice velocities were calculated in that location using descending-pass data only and we estimate errors for this area to be roughly 10 m yr^{-1} as estimated in the same way as the dual-look error (RMS value is 8.8 m yr^{-1}). The sensor LOS for ascending passes is almost perpendicular to the direction of ice flow, and is therefore insensitive to ice motion at the south-flowing glaciers in the southern part of the ice cap.

Finally, ice motion was determined at 22 stakes positioned across the LIC (Figure 3.2) during the summer of 2001 (April to October) over a period of 170 days using differential GPS. The error on the stake velocities was calculated by dividing the sum of the error in the position of the differential GPS measurements (2 x 50 cm) by the interval between measurements (170 days) to obtain a value of ± 2.2 m yr^{-1}.

3.4. Results and discussion

Our InSAR data represent the first detailed map of the LIC velocity field (Figure 3.2). Eight outlet glaciers are apparent from the InSAR velocity data, with the majority located in the Northern half of the LIC. Three glaciers flow to the West or Northwest, and the remainder flow to the East or Southeast. Although apparent from GPS measurements (locations 1 to 8, Figure 3.2), the Southward flowing outlet glacier of Hagafellsjökull Vestri is not obvious in the InSAR data due to the large angle between the ice flow direction and the radar look direction, a condition which is not favourable for detecting ice motion from single pass data. These 8 glaciers surveyed range in area from 18 km^2 to 71 km^2 (Table 3.2) and the maximum ice speed we recorded is 75 m yr^{-1} at the terminus of Sudurjökull in the Southeast part of LIC. Derived velocities are below the InSAR measurement error for 32 % of LIC and are omitted from Figure 3.2. The elevation at which the surveyed glaciers reach their maximum velocity varies between 1200 m for the Northeast glacier to 870 m for Kirkjujökull, with an average across all 8 outlet glaciers of 1000 m.

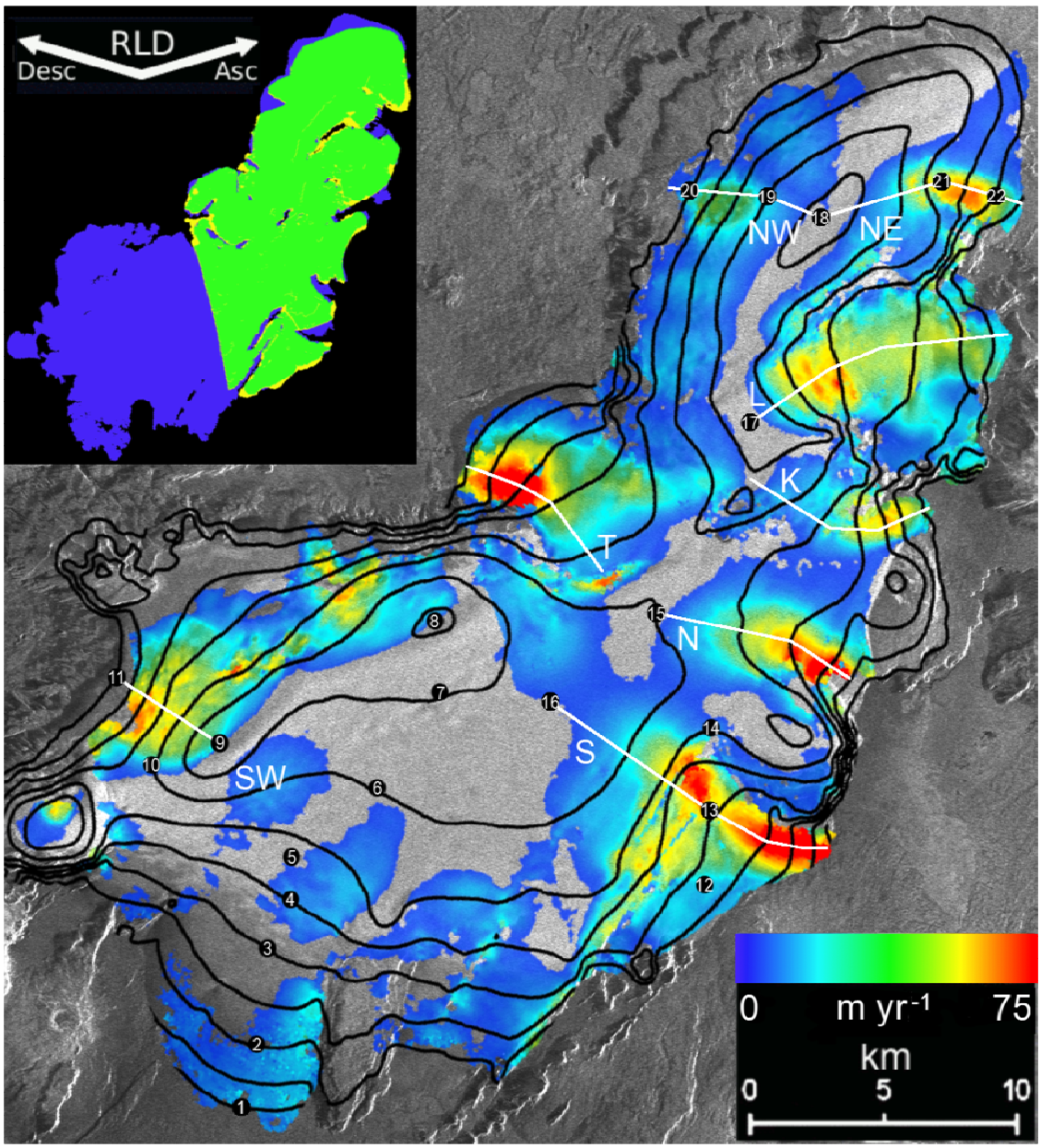

Figure 3.2. Ice velocity map with 100m elevation contours, GPS stake locations and data transects shown in figures 3.3 and 3.4, projected over SAR intensity image. Locations of data transects are shown in white: Northwest transect (NW), Northeast transect (NE), Leidarjökull (L), Kirkjujökull (K), Nordurjökull (N), Sudurjökull (S), Southwest transect (SW), Thristapajökull (T). Areas of 3D velocity (green), ascending-pass only (yellow) and descending-pass only (blue) are shown inset. Radar look direction (RLD) for ascending (Asc) and descending passes (Desc) are also shown.

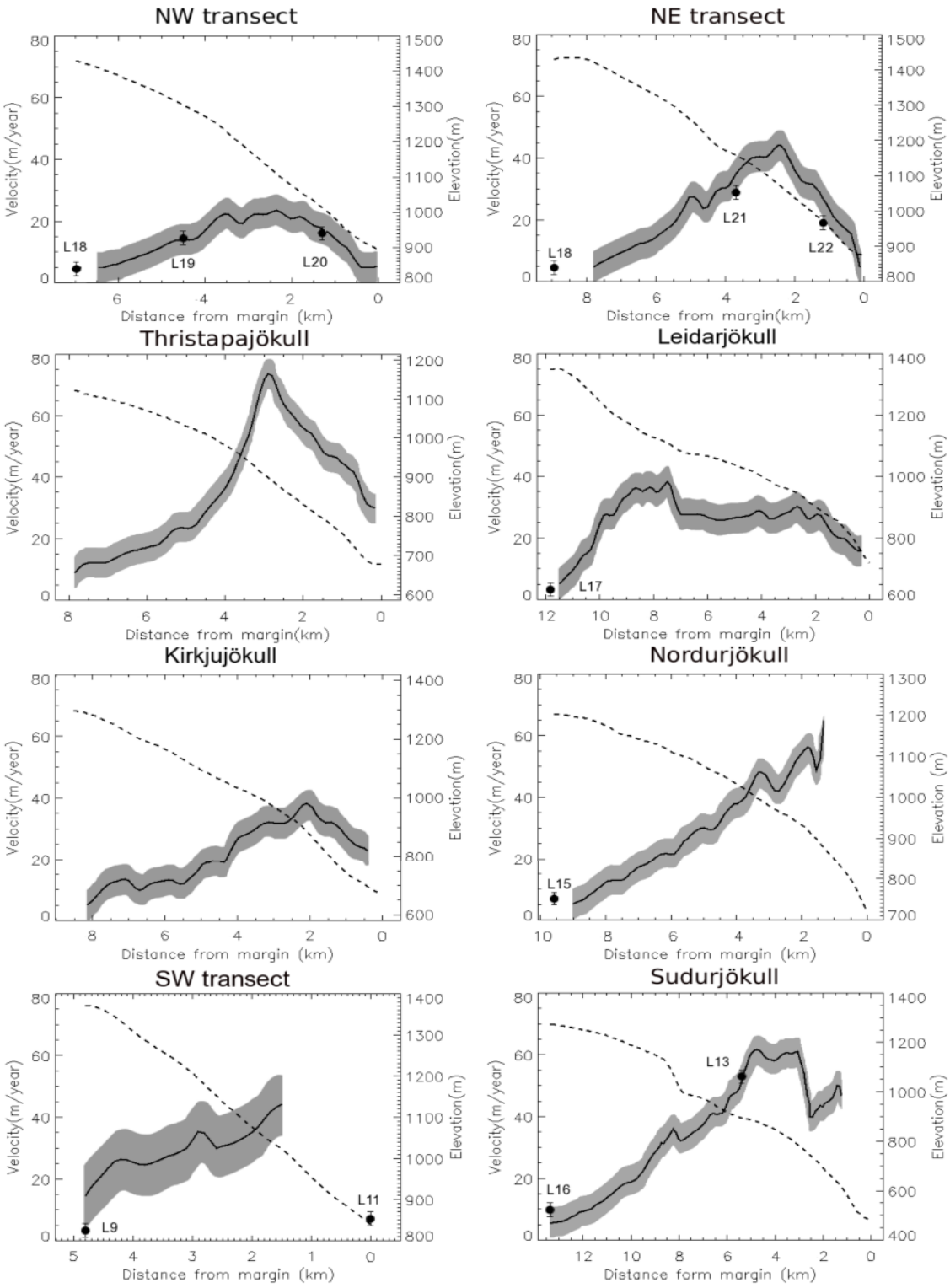

Figure 3.3. InSAR-derived velocity for winter 1994 (solid line), and 1997 ice surface (dashed line) for transects shown in figure 3.2. Solid points with error bars show 2001 summer velocity from stake measurements. Grey areas show error for InSAR velocity values.

We extracted InSAR velocity data along eight transects (see Figure 3.2) of the LIC that passed close to the centre of each principal glacier and linked by the GPS survey sites,

to allow for a more detailed comparison of the two datasets. A summary of the LIC geometry and flow along each transect is shown in Table 3.2. The glaciers can be grouped by the shape of their InSAR velocity profiles as shown in Figure 3.3. Along the Northwest, Northeast and profiles, ice velocity increases progressively from near-zero at the highest elevations to a maximum around 2.5 km from the ice margin at an elevation of around 1150 m, and decreases gradually thereafter to around zero at the terminus. The Southwest transect has similar characteristics though due to loss of coherence near the ice margin, InSAR velocity was not retrievable for the whole profile. Although Kirkjujökull exhibits a similar profile, ice velocity at the terminus is about 20 m yr^{-1}. At Thristapajökull, the ice velocity increases along the transect until it reaches its maximum value of 75 m yr^{-1} about 3 km from the margin. Below this, ice velocity decreases with a roughly constant rate to around 30 m yr^{-1} at the ice margin.

Transect	Length (km)	Max. speed (m yr^{-1})	Mean speed (m yr^{-1})	Mean elevation (m)	Position of max. speed (km)	Elevation of max. speed (m)	Glacier Area (km^2)
Northwest	7	25	14	1200	2.4	1100	18.5
Northeast	9	44	22	1180	2.5	1200	18.3
Thristapajökull	8	75	36	940	2.8	900	53.3
Leidarjökull	12	37	25	1065	7.5	1100	71.2
Kirkjujökull	7.5	38	20	1050	2.0	870	17.6
Nordurjökull	10	64	28	1040	1.7	880	37.4
Southwest	5	44	30	1125	1.5	1030	39.4
Sudurjökull	13.5	63	34	980	4.8	890	61.3

Table 3.2. InSAR velocity-transect attributes. Position and height of maximum speed is the distance from the margin and altitude, respectively, of where maximum ice speed occurs.

The three remaining transects exhibit markedly different behaviour from those above as well as each other (Figure 3.3). Ice velocity for Leidarjökull increases rapidly from the ice divide to a maximum of 40 m yr^{-1} within a short distance (4 km) of the ice divide. Thereafter, ice velocity remains approximately constant at about 30 m yr^{-1} before

decreasing to about 10 m yr^{-1} in the final 2 km. The lower part of the outlet covers a caldera where ice thickness is approximately 400 m. The central part of the surface profile has a shallower surface gradient, and a rough estimate of the deformation velocity (from surface slope and ice thickness) yields ~15 m yr^{-1}, which accounts for only half of the observed surface-flow. Calculations of basal water pressure based on radio-echo sounding studies of bedrock topography (Gudmundsson et al., 2009; Flowers et al., 2007) suggest that sliding at the bed is enhanced for Leidarjökull, which helps to explain the concave-up surface profile. At Nordurjökull, ice velocity increases at roughly a constant rate along the length of the profile, though due to coherence loss near the terminus, we were unable to retrieve InSAR velocity for the final 1 km. The lower slopes of this glacier are narrow and steep and the outlet flows into the Hvítárvatn lake. Though the terminus does not float, ice breaks-off at the margin into the lake and the presence of water is likely to reduce basal friction which may explain the high ice velocity near the terminus. Along Sudurjökull, ice velocity increases gradually down slope from the ice divide to around 60 m yr^{-1} where it remains roughly constant for ~ 2 km. At 3 km from the margin, ice velocity drops by 20 m yr^{-1} in 500 m horizontal distance although low coherence prevented retrieval of the final 1 km, it is likely that ice velocity at the terminus is around 40 m yr^{-1}. This area of high velocity on the lower slopes suggests that in February 1994, Sudurjökull was experiencing a surge. The record of GPS surveyed velocities at site L13 between summer 1997 and summer 2008 also suggests that another surge started in summer 1999 (the velocity in summer 1999 is 65 m yr^{-1}) and culminated in 2004; by 2005 the velocity had dropped to 40 m yr^{-1}. The positions of the terminus on maps from 1986, 1997 and 2004 show that the terminus must have advanced between 1986 and 1997 and again between 1997 and 2004 which is consistent with the above. There is anecdotal evidence that Sudurjökull has surged in the past (Björnsson et al., 2003) and it is also known from sediments in the lake in front of the terminus that Sudurjökull has been extremely dynamic (Geirsdottir et al., 2008).

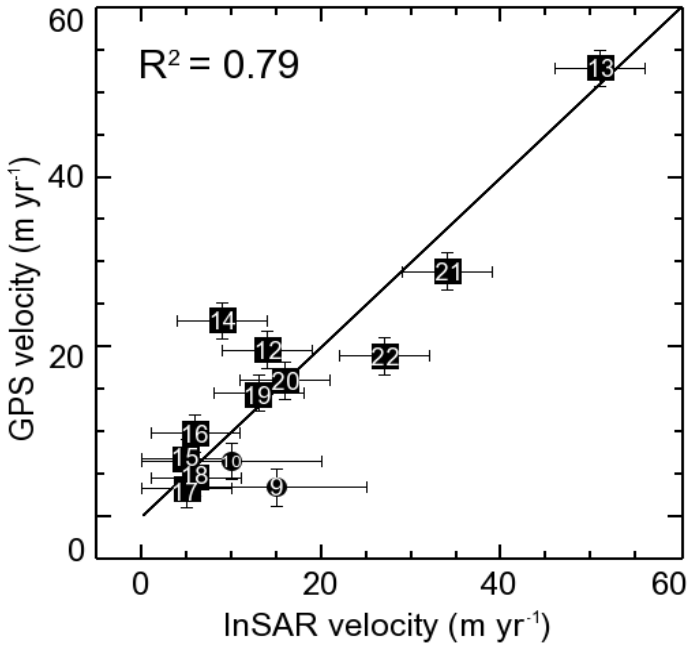

Figure 3.4. Comparison of InSAR and GPS derived ice velocities for 13 locations on the ice cap, numbered as in Figure 3.2. Data from locations covered by dual-look InSAR are shown as squares; those for single-look coverage are shown as circles. Stake locations on Hagafellsjokull Vestri (1 to 8) are omitted as agreement is not expected due to enhanced ice velocity in 2001 following a glacier surge in 1999 and the fact that the radar look direction is insensitive to flow. Location 11 was also omitted from the comparison as no InSAR data was available within 500 m.

The correlation between the InSAR and GPS data, shown in Figure 3.4, is 0.79 with a RMS difference of 5 m yr^{-1}. Observations at locations on Hagafellsjökull Vestri were omitted as ice flows in a direction for which the sensor had little sensitivity due to the acquisition geometry. In addition, the GPS data for this glacier show that in 2001, the glacier velocity peaked 9.4 km from the margin at an elevation of 950 m.a.s.l. and velocity was enhanced following a surge event of 1999, so agreement between the InSAR and GPS observations is not expected. That the smallest measurement uncertainties (± 5 m yr^{-1}) are at the level of the RMS difference between the InSAR and GPS velocities suggests that any seasonal or inter-annual variations in ice velocity between February 1994 and summer 2001 are modest.

3.5. Conclusions

This research provides the first ice velocity map for Langjökull ice cap, Iceland. The

velocity data were derived from ERS SAR interferometry, and the data were acquired between the 22nd and 27th February 1994. We have identified eight principal outlet glaciers and the maximum speed recorded was 75 m yr^{-1}. Eight down-glacier velocity transects were extracted, along three of which we were able to compare our InSAR results with sparse surface velocity measurements determined from a GPS survey undertaken over 170 days during Summer 2001. At six of the eleven locations included in both the GPS and InSAR data sets, ice velocity measurements were within error, indicating little change in ice velocity between February1994 and Summer 2001. The largest difference (47 ± 10 m yr^{-1}) between the InSAR and GPS velocity datasets occurred at Hagafellsjökull Vestri (L4) and is attributed to locally high InSAR measurement error and the fact that in 2001, ice velocity was elevated following a surge.

The close agreement between the GPS and InSAR datasets indicates that seasonal ice velocity variations at LIC are small, though non-zero velocities at the termini of 4 of the 8 glaciers surveyed suggest that these glaciers were advancing in February 1994. Our data, in addition to other studies, suggest that Sudurjökull was experiencing a surge in 1994.

Chapter 4: InSAR observations of ice elevation and velocity fluctuations at the Flade Isblink ice cap, eastern North Greenland.

This chapter describes the application of repeat-pass InSAR techniques to derive ice surface elevation and velocity for the largest independent ice cap in Greenland. This Chapter is in preparation for submission to Journal of Geophysical Research:

Palmer, S.J., A. Shepherd, A.Sundal, E. Rinne and P. Nienow (in preparation), InSAR observations of ice elevation and velocity fluctuations of the Flade Isblink ice cap, eastern North Greenland, *Journal of Geophysical Research.*

I identified the study area, processed the InSAR data, interpreted the results and wrote the manuscript. Shepherd assisted with the data processing, interpretation and writing of the manuscript. Sundal processed the feature-tracking data and contributed to the methods section of the manuscript. Rinne processed the ICESat data, performed the elevation data inter-comparison and contributed to the methods section of the manuscript. Nienow assisted with glaciological interpretation.

4.1. Abstract

The 8500 km^2 Flade Isblink Ice Cap (FIIC) (81° 15' N, 15° 0' W) is the largest ice cap in Greenland. We use repeat-pass Interferometric Synthetic Aperture Radar (InSAR) and Synthetic Aperture Radar (SAR) feature tracking techniques to investigate the form and flow of the FIIC. European Remote Sensing satellites (ERS-1 and ERS-2) data acquired in winter 1996 were used to form a 100 m resolution digital elevation model (DEM), which we constrained using Ice Cloud and Elevation satellite (ICESat) laser altimeter elevation measurements from 2007. This InSAR DEM was used to isolate the phase due to motion from 7 ERS-tandem (1-day) pairs of SAR scenes acquired between 15th August 1995 and 7th February 1996, to produce 2 wintertime and 2 summertime velocity maps. We derived separate velocity estimates by tracking features within summer and winter pairs of SAR amplitude imagery separated by 35-days, and compared these with our 1-day InSAR velocity estimates. Five of the eight major outlet glaciers draining the FIIC are marine-terminating and two terminate at a lake margin. A maximum ice velocity of 581 m yr^{-1} was observed in mid-August 1995. Five of the of the eight major outlet glaciers exhibit seasonal velocity variations between late-summer and winter and flow speeds vary by up to 20 % over a 10 day period in August 1995. Our findings show that while marine-terminating glaciers flow faster than land-terminating glaciers, there is no simple relationship between glacier type and seasonality of ice motion.

4.2. Introduction

The Flade Isblink Ice Cap (FIIC) is situated in Kronprins Christian Land, Eastern North Greenland (Figure 4.1) on Princess Dagmar Peninsula. With an area of 8 500 km^2, it is the largest independent ice cap in Greenland (Kelly and Lowell, 2009). The northern portion of the ice cap exhibits low surface slopes and reaches a maximum elevation of around 710 m. In contrast, the southern part overlays the Princess Elisabeth Alps and many nunataks are present. Surface gradients are generally steeper in the southern part of the ice cap and the maximum elevation is around 960 m. The earliest study of the FIIC (Mikkelsen, 1913) was restricted to ground-based observations of the basic geometry and extent of the ice cap. The FIIC was originally discovered in 1907 during

the ‘Danmark’ expedition led by Mylius-Erichsen, although it was not until the first aircraft surveys of this area in 1932 that the ice cap was discovered to be independent of the Greenland ice sheet (Koch, 1935). The ice cap was observed to slope evenly and crevasse-free towards the Arctic Ocean in most places except at Antarctic Bay, where the ice formed steep walls, behind which existed extensive crevasse systems. Helk and Dunbar (1953) observed that FIIC was apparently inactive with a stagnant East side and a Northern margin ‘disintegrating into flat-topped bergs’.

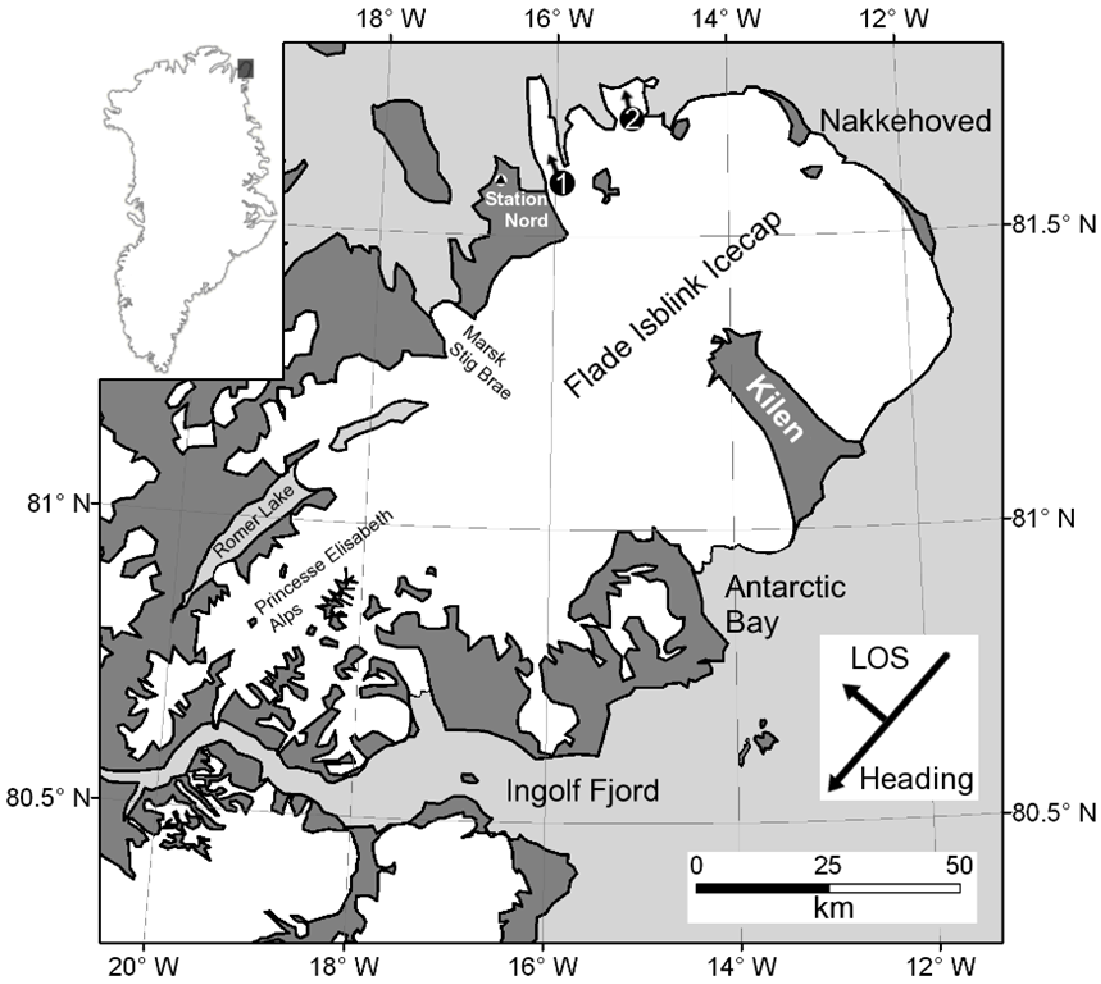

Figure 4.1. Location map of the Flade Isblink Ice Cap (FIIC), with satellite heading and radar line-of-sight (LOS) indicated. The locations (numbers 1 and 2) of previous velocity estimates (Higgins, 1991) discussed in the text are also shown.

More recently, remote sensing studies have provided sparse observations of ice velocity and surface elevation changes. Higgins (1991) used aerial photographs acquired in 1961 and 1978 to track features of the FIIC in order to estimate the mean velocity at 2 locations shown in Figure 4.1. A 25 km broad outlet to the East of Station Nord was

identified, extending northwards as a floating glacier tongue up to 20 km long, although no significant iceberg calving events were reported during the survey period (Higgins, 1991). Observed velocities were 360 m yr^{-1} at the western lobe (Figure 4.1, location 1) and 175 m yr^{-1} at the eastern lobe (Figure 4.1, location 2). Krabill et al., (2000) used aircraft laser altimeter observations from 1994 and 1999 to measure surface elevation changes at the FIIC. Mean thickening rates of 60 cm yr^{-1} were observed in the South and 40 cm yr^{-1} in the North, and up to 20 cm yr^{-1} of thinning occurred at the eastern margin. More recent ICESat observations showed a distinct longitudinal gradient in surface elevation change, with the western half of the FIIC having thickened by around 50 cm yr^{-1}, and the eastern half having thinned by around 20 cm yr^{-1} between 2003 and 2007 (Pritchard et al., 2009). A radio echo sounding survey of the FIIC carried out by the US Center for Remote Sensing of Ice Sheets and the Danish Niels Bohr Institute during May 2006 showed that ice near to the ice cap summit is around 535 m thick (C. Laing, unpublished data, 2009), though was also too wet for internal layers to be resolved. In addition, Hall et al. (2008) have compared satellite-based Moderate Resolution Imaging Spectroradiometer (MODIS) measurements of surface temperature to *in-situ* observations and found that there was no variation in surface temperature with elevation on 3 July 2001 and on 23 June 2004. Together, these two studies suggest that the entire ice surface of the FIIC is at or near to melting between May and July. Here we use InSAR techniques to form a new 100 m resolution elevation model and the first velocity maps of the FIIC, in order to investigate flow variations of the main outlet glaciers between summer1995 and winter 1996.

Date	Day number	Sensor	Orbit	Frames	B⊥ (m)	Use
20/7/95	201	ERS1	20983	1932	-	Summer tracking velocity
15/8/95	227	ERS1	21355	1939	-2	Summer InSAR velocity
16/8/95	228	ERS2	1682			
24/8/95	236	ERS1	21484	1920,1931	1	Summer InSAR velocity
25/8/95	237	ERS2	1811			Summer tracking velocity
2/1/96	367	ERS1	23359	1929,1939	8	InSAR DEM
3/1/96	368	ERS2	3686			Winter InSAR velocity
6/2/96	402	ERS1	23860	1929,1939	200	Winter tracking velocity
7/2/96	403	ERS2	4187			

Table 4.1.(previous page). SAR data used in this Chapter. Data used for summertime feature-tracking velocity estimates are highlighted in dark grey, data used for wintertime feature-tracking velocity estimates are highlighted in light grey.

4.3. Data

We use 15 ERS SAR images acquired between 20th July 1995 and 7th February 1996 (Table 4.1) to calculate the elevation and velocity of the FIIC. During this tandem-mission period, the ERS-2 satellite followed the ERS-1 satellite in a near-identical orbit, 1-day behind. The short time interval between acquisitions ensures that interferometric coherence is maintained as the surface changes little during the intervening period. SAR data acquired during the ERS tandem mission have proved to be a key dataset for studies of the cryosphere and have been used to map velocity over large areas (e.g. Shepherd et al., 2001), grounding line retreat (e.g. Rignot, 1998) and melting at the base of floating ice (e.g. Joughin and Padman, 2003). We obtained raw SAR scenes and processed them to single-look, complex (SLC), slant-range image data for our interferometric analysis (Werner et al., 2000). These image frames typically cover 100 km by 100 km. The data were recorded during descending satellite orbits, when the satellite ground track was almost parallel to the long axis of the FIIC (see Figure 4.1), resulting in a favourably-oriented radar look direction for 7 of the 8 outlet glaciers observed. From these data, we were able to assemble 4 pairs of SAR images separated by 1 day that were suitable for interferometry and 2 pairs that were suitable for SAR feature-tracking.

We use point-measurements of elevation acquired by the Geoscience Laser Altimeter System (GLAS) instrument onboard NASA's Ice Climate and Elevation satellite (ICESat) (Zwally et al., 2003) to constrain and validate our interferometric dataset (see methods section 4.5). The GLAS provides measurements of elevation along the satellite ground-track of 65 m spatial resolution at 172 m spacing (Zwally et al., 2002b; Pritchard et al*.,* 2009). The elevation measurements are repeated along nearly-identical tracks every 91 days. We use GLAS- Level-1B elevation data (GLA06) recorded in 2007, which includes corrections for atmospheric propagation delays and the effect of solid Earth tides (Brenner et al., 2003), to provide an improved estimate of the interferometric baselines and to validate an elevation model that we produce from InSAR. We also use

an existing, coarse resolution DEM of the GrIS, gridded at 1 km horizontal spacing (DiMarzio et al., 2007) as part of the validation exercise. This DEM was produced from data acquired during the first seven operational periods (from February 2003 through June 2005) of the GLAS instrument.

Finally, we use local air temperature measurements to aid our interpretation of the FIIC velocity dataset (see discussion section 4.7.2). Daily maximum air temperature measurements were acquired at Station Nord (81° 36' N, 16° 41' W) automatic weather station (AWS) between January 1986 and May 2009 (www.tutiempo.net). The dataset provides a near-continuous record of air temperature in the vicinity of the FIIC, although no data were available for the periods September 1988 to January 1989, September to November 1999, September 2003 to September 2005, November 2005 and March to July 2007.

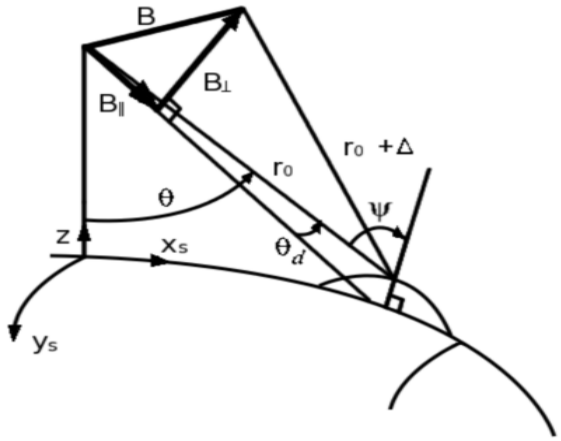

Figure 4.2. Schematic showing repeat-pass InSAR geometry. After Joughin et al. (1998).

4.4. Interferometry Background

By interfering two SAR images, a measure of the interferometric phase (ϕ) is obtained. ϕ can be considered to be a linear combination of independent contributions due to several terms (Bamler and Hartl, 1998), including imaging geometry (the spheroid-Earth phase) ϕ_0, local topography ϕ_{topo}, surface motion ϕ_{motion}, atmospheric (tropospheric and ionospheric) propagation delays ϕ_{atm} and system noise ϕ_{noise}, where:

$$\phi = \phi_0 + \phi_{topo} + \phi_{motion} + \phi_{atm} + \phi_{noise} \quad (4.1)$$

As our study area is at high-latitudes where the atmosphere is thinnest, and because the SAR data were acquired at a time of minimal solar activity (Lang, 1999), the atmospheric phase contribution ϕ_{atm} is likely to be a fringe or less. As this is much smaller than the phase contribution due to ice motion ϕ_{motion} (on the the order of 100 fringes for the fastest flowing ice), the ϕ_{atm} component is sufficiently small to be ignored. By selecting interferometric image pairs of suitable coherence, ϕ_{noise} is minimized such that ϕ can be rewritten, after the spheroid-Earth correction is applied, as a function of the topographic- and motion-contributions alone:

$$\phi_{unwrap} = \phi_{topo} + \phi_{motion} \quad (4.2)$$

where ϕ_{unwrap} denotes the unwrapped interferometric phase difference achieved by processing to remove the modulo-2π ambiguity (Werner et al., *2000*). For repeat-pass interferometry, the range difference between passes, Δ, is estimated by using:

$$\Delta = \frac{\lambda}{4\pi}\phi_{unwrap} \quad (4.3)$$

where λ is the radar wavelength. Referring to the geometry of repeat-pass satellite interferometry (Figure 4.2), the interferometer baseline (their separation in space) and range difference due to topography Δ_{topo} are related by:

$$B_{\perp}\sin\theta_d + B_{\text{II}}\cos\theta_d = -\Delta_{topo} - \frac{\Delta_{topo}^2}{2\overline{r_0}} + \frac{B^2}{2\overline{r_0}} \quad (4.4)$$

where $B\perp$ and $B_{\parallel}$ are the normal and parallel components of the baseline B, relative to the radar slant range vector r_0. Applying (4.2) and (4.3), the phase due to topography is solved for as:

$$\begin{aligned}\phi_{topo} &= \frac{4\pi}{\lambda}\left[-\bar{r_0} + \sqrt{\bar{r}_0^2 - 2\bar{r}_0\left(B_\perp \sin\theta_d + B_{\text{II}} \cos\theta_d\right) + B^2}\right] \\ &\approx -\frac{4\pi}{\lambda}\left(B_\perp \sin\theta_d + B_{\text{II}} \cos\theta_d - \frac{B^2}{2\bar{r_0}}\right)\end{aligned} \tag{4.5}$$

The contribution to the phase from surface motion ϕ_{motion} is given by:

$$\phi_{motion} = \frac{4\pi}{\lambda}\left(\Delta_{motion,xs} \sin\varphi - \Delta_{motion,z} \cos\varphi\right) \tag{4.6}$$

where $\Delta_{motion,xs}$ denotes the component of displacement tangiential to the surface of a reference ellipsoid and directed orthogonal to the satellite ground track, $\Delta_{motion,z}$ denotes displacement directed normal to the ellipsoid, and φ denotes the local surface slope (see Figure 4.3). For steady motion during the interferograms acquisition interval, the phase is related to the surface velocity by:

$$\phi_{motion} = \frac{4\pi}{\lambda}\left[\delta T\left(v_{xs} \sin\varphi - v_z \cos\varphi\right)\right] \tag{4.7}$$

where δT is the time interval between acquisition of images, v_{xs} is the across-track component of velocity and v_z is the component of velocity directed normal to the ellipsoid.

Separation of the topographic and motion terms using only SAR data may be achieved by the double-differencing technique (e.g. Rignot, 1998). The procedure involves differencing two interferograms of differing baselines in order to cancel the phase contribution from surface motion and therefore isolate the phase contribution from topography. This method relies on the assumption that surface motion is the same during each of the acquisition intervals. Equation 4.2 shows that the unwrapped interferometric phase ϕ_{unwrap} contains contributions from both topography and motion toward or away from the sensor in the SAR LOS (Joughin et al., 1996c). The phase from two interferograms from four passes (1, 2, 3 and 4) can be written:

$$\Delta\phi_{12} = \frac{4\pi}{\lambda}\left[B_{12} \sin\left(\theta - \alpha_{12}\right) + v\delta T \cdot \bar{r_0}\right] \tag{4.8}$$

and

$$\Delta\phi_{34} = \frac{4\pi}{\lambda}\left[B_{34}\sin(\theta - \alpha_{34}) + v\delta T \cdot \overline{r_0}\right] \tag{4.9}$$

where α is the tilt of the baseline with respect to the horizontal. Although the flow of outlet glaciers and ice sheet margins can and does change with time (e.g. Joughin et al., 2008) motion is in general least variable in winter, and we assume that the 35-day interval between our winter interferograms is short enough for the assumption of invariant flow to be valid. As the duration of observation δT is also equal for both acquisitions, the phase due to motion, $(4\pi/\lambda)v\delta T \cdot \boldsymbol{r_0}$, is a constant and differencing the two interferograms yields a single interferogram with the contribution of the displacement field to the phase removed:

$$\begin{aligned}\Delta\phi_{12-34} &= \Delta\phi_{12} - \Delta\varphi_{34} \\ &= \frac{4\pi}{\lambda}\left[B_{12}\sin(\theta - \alpha_{12}) - B_{34}\sin(\theta - \alpha_{34})\right]\end{aligned} \tag{4.10}$$

The interferometric sensitivity to the variation in ice sheet topography now depends on the difference between the two interferometer baselines B_{12} and B_{34}. To form a differential interferogram with high sensitivity to topography, the difference between B_{12} and B_{34} should be large. This topography-only interferogram can then be scaled to the appropriate baseline length and subtracted from the remaining mixed interferograms in order to isolate the phase contribution due to ice motion. Assuming that ice flows parallel to the surface and in the direction of steepest slope (Paterson, 1994), the motion-phase (ϕ_{motion}) can be used to estimate the relative ice velocity (e.g. Kwok and Fahnestock, 1996).

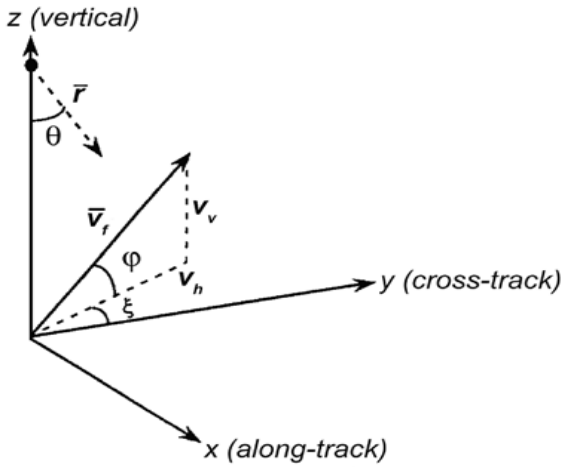

Figure 4.3. Schematic showing the effect of surface relief on observed LOS velocity (Kwok and Fahnestock, 1996).

In order to isolate phase due to displacement, the topography-only interferogram, $\Delta\phi_{12\text{-}34}$, is subtracted from the original mixed interferogram e.g.:

$$\Delta\phi_{34} - k\Delta\phi_{12-34} = 2kv\delta T \cdot \overline{r_0} \tag{4.11}$$

where k is the factor scaling the $B_{12\text{-}34}$ fringe pattern into that of the B_{12} interferogram which is essential to compensate for the difference in sensitivity to topography due to the different baselines.

The LOS displacement measured by InSAR is a function of the radar look angle θ, the surface slope φ and the angle (in the x-y-plane) formed between the look direction projected onto the x-y-plane and in the ice flow direction ξ [*Kwok and Fahnestock*, 1996] (see Figure 4.3). From this geometry, the component of the ice surface velocity vector in the radar LOS (slant range) direction V_r is given by:

$$V_r = \frac{\phi\lambda}{4\pi\delta T} + V_0 \sin\theta\cos\xi \tag{4.12}$$

where V_0 is the spatially constant component of the surface velocity. The first term is based on the satellite-derived difference due to ice-surface displacement between image acquisitions, and represents the spatial variability in velocity. This is only a relative rather than absolute velocity as it includes no spatially constant velocity. The absolute

displacement offset is typically estimated using ground control points (GCPs) (Joughin et al., 1998). The second term is analogous to a baseline velocity, with sine and cosine functions projecting the constant ice surface velocity into the direction of the radar LOS. The ice surface velocity in the direction of actual flow V_f can then be written (Kwok and Fahnestock, 1996):

$$V_f = \frac{V_r}{\cos\xi\cos\varphi\sin\theta - \cos\theta\sin\varphi} \tag{4.13}$$

As the measurement of velocity requires observations at two or more points (i.e. from two or more look-directions), the radar look angle θ and the angle between the radar look and actual ice flow direction ξ change with one measurement of V_f. In the above relationships, the surface slope is taken to be in the direction of flow, with the implicit assumption that the flow vector is tangential to the surface topography. $V_v = V_f\sin\varphi$ and $V_h = V_f\cos\varphi$ are the vertical and horizontal components, respectively, of the velocity vector in the flow direction (Figure 4.3), and both are present in the InSAR-derived ice motion. The fact that a repeat-pass interferometer is sensitive to surface displacement directed along the LOS only (Joughin et al., 1998) has the effect of emphasizing vertical relative to horizontal displacement (Joughin et al., 1995). As a result, it is not possible to unambiguously separate the mixed vertical and horizontal displacement signals in the interferogram without additional information or assumptions (Joughin et al., 1998).

4.5. Methods

We processed 15 ERS tandem SAR scenes to determine the elevation and velocity of 90 % of the FIIC. From these data, we formed 2 winter and 2 August interferograms, which were sensitive to both surface movement in the radar LOS during the acquisition period and to the topography of the ice cap surface (Joughin et al., 1998). Differential-InSAR was used to produce a topography-only interferogram (Kwok and Fahnestock, 1996) which was then calibrated to absolute heights (Joughin et al., 1998) using ICESat elevation measurements (Zwally et al., 2003). This InSAR DEM was used to remove topographic phase from the remaining interferograms in order to isolate the velocity signal (Kwok and Fahnestock, 1996). The methods for each step are described in detail below.

4.5.1. Raw data processing.

The raw ERS data were processed to SLC format using a commercially available SAR processor (Werner et al., 2000) and precise orbit data (Scharoo and Visser, 1998). Corrections were made to compensate for the antenna gain patterns, non-zero doppler centroids and variations in doppler frequency along-track caused by squint (Werner et al., 2000). We extended the near- and far-range in each SAR dataset to form images 2808 range pixels wide. Range compression, azimuth auto-focusing and azimuth compression were then applied. The SAR images were multi-looked to reduce speckle noise by 2 in the range direction and10 in the azimuth direction (Werner et al., 2000). Each SAR image pair was co-registered to within a few pixels using precision satellite state-vector data (Gens and van Genderen, 1996), followed by fine co-registration to a fraction of a pixel by comparing roughly corresponding areas and solving for a set of local transformation parameters (Massonet and Feigl, 1998). Complex interferograms containing both the amplitude and phase information were then formed by multiplying each complex pixel of the primary image by the complex conjugate the corresponding pixel in the secondary image.

4.5.2. InSAR DEM

We differenced the 2 winter interferograms to form a topography-only interferogram with an effective baseline of 192 m. We calculate the altitude of ambiguity, which is a measure of the sensitivity to topography, to be 45 m. This differential interferogram was corrected for the effect of Earth's curvature and filtered with a window size of 32 then again with a window size of 8 to reduce phase noise. As the interferometric phase is measured in modulo 2π, phase unwrapping was applied to covert to continuous phase at each point as described by Rosen et al. (1994). The unwrapped interferometric phase, together with the precision baseline estimate is then used to derive the topographic heights. Absolute surface elevation can only be retrieved with the use of tie-points of known elevation (Mohr, 1997). As InSAR-derived height maps contain relative values only, they require calibration to yield absolute values. We achieved this by applying least-squares fit of the unwrapped phase at ~500 points of known elevation measured by ICESat in 2007, and an improved estimate of the interferometric baseline was achieved

in the same way (Joughin et al., 1998). The data were then geocoded into UTM zone 28N to form a new DEM of the FIIC posted at 100 m.

Surface catchments were derived from the InSAR DEM using a hydrologic model (Maidment, 2002). Local topographic minima were filled and flow direction for each cell was then calculated from the direction of steepest slope. Stream segments were defined and grouped into individual catchments, which were used to derive glacier boundaries. Figure 4.2 shows the InSAR DEM and surface-derived surface catchments for the 8 major outlet glaciers.

4.5.3. InSAR velocity

We used the InSAR DEM to subtract topographic phase from other interferograms in order to isolate displacement in the radar LOS. As with the computation of topography, phase was unwrapped from modulo-2π to generate a continuous phase field. Calibration was achieved by a least-squares fit for phase values at the ice divide, which were assumed to have zero motion. Assuming surface-parallel flow in the direction of steepest slope, we were able to convert LOS displacements to ice velocity estimates over the FIIC for the dates of our interferograms (Joughin et al., 1996). To compute the ice flow direction, we averaged the elevation model over 2000 m, which is equal to approximately 10 times the mean ice thickness (Paterson, 1994). In all cases, the phase coherence was sufficiently high to allow phase unwrapping all the way from the summit ice divide, to the glacier margin or edge of the scene. Therefore, in-situ measurements of velocity were not necessary to constrain the velocity estimation. In this way we were able to estimate the average rate of ice motion over 24-hours for day numbers 228, 237, 368 and 403.

The baselines associated with the SAR image pairs used to estimate ice speed were all below 10 m, resulting in interferograms which were insensitive to topographic errors (Goldstein et al., 1993; Joughin et al., 1996c). By calculating ice speed over 1200 km^2 of ice-free ground adjacent to the FIIC on day-237, we estimated the error in our measurements of ice speed to be 7 m yr^{-1} (RMS value is 6.9 m yr^{-1}). Even with reliable independent knowledge of the ice-flow direction, the accuracy of the resultant velocity estimate may be poor when this direction is close to orthogonal to the radar LOS

direction, for which there is no sensitivity to displacement. The orientation of the radar LOS was oriented parallel to the direction of ice flow away from the central ice divide of the FIIC, thereby minimizing errors for these glaciers. The error in the velocity estimates at glacier C is likely to be larger due to the unfavorable radar LOS. Table 4.2 indicates the suitability of the radar LOS for minimizing errors in velocity measurements.

4.5.4. Feature-tracked velocity

We used SAR feature-tracking to provide estimates of ice speed over a longer time period in order to investigate the temporal variability of ice motion and also to validate our InSAR results. Feature tracking provides estimates of surface displacement fields by tracking motion between image pairs (Scambos et al., 1992; Bindschadler and Vornberger, 1998). The technique has been successfully used with SAR data for the study of ice flow (e.g. Strozzi et al., 2002; Luckman et al., 2006; Nakamura et al., 2007). Unlike conventional InSAR, feature tracking measures displacement in the range and azimuth directions simultaneously. The technique relies on cross-correlation of SAR backscatter amplitude images and the estimated offsets are unambiguous values, which means that phase unwrapping is not required (Werner et al., 2001). However, feature-tracking is less accurate and produces velocity maps with lower spatial resolution than InSAR, and errors cannot be identified without manual inspection. It has been found that a combination of feature tracking and InSAR provide the most efficient way to determine the motion of a glacier (Strozzi et al., 2002).

We applied the SAR feature-tracking method of Strozzi et al. (2002) to 2 pairs of ERS SAR images separated by 35 days; 1 pair acquired during summer 1995 and 1 pair acquired during winter 1996 (Table 4.1). The orbital offsets were determined by fitting a bilinear polynomial function of offset fields computed globally from the SAR images assuming no displacement for most parts of the image. The local offsets were determined by correlating peak intensities within regularly spaced image patches; we used patch sizes of 128 by 256 pixels. Correlation signal-to-noise ratios were used to reject poor matches, and the resulting velocity fields were transformed to map coordinates using our InSAR-derived elevation model. Using the method of estimating errors from the motion values for ice-free areas in the work of Pritchard et al., (2005),

we estimate the errors in the feature-tracking speed to be ± 18 m yr^{-1} for the winter data and ± 12 m yr^{-1} for the summer data.

4.6. Results

4.6.1. InSAR DEM

The InSAR DEM was generated with a ground-resolution of 100 m (Figure 4.4), and covers the majority (7 700 km^2, equivalent to 91 % of the ice area) of the FIIC. To estimate the accuracy of the DEM, we compared it to ~40 000 point-measurements of elevation determined by the ICESat satellite laser altimeter during the period 2003 to 2009 (Zwally et al., 2003), excluding data from 2007 which was used to calibrate the InSAR DEM. The RMS difference between the InSAR DEM and the ICESat point-measurements of elevation was 12 m (Figure 4.5). For comparison, we also computed the rms difference between the ICESat point-measurements of elevation and an existing DEM formed from ICESat data (DiMarzio et al., 2007), and this was 10 m (Figure 4.5). Areas with surface slopes greater than 5 degrees were omitted from the comparison due to the poor performance of the GLAS instrument over steep terrain (Zwally and Brenner, 2001).

The InSAR DEM (Figure 4.4) covers the vast majority of the FIIC and is of comparable accuracy to an existing DEM (DiMarzio et al., 2007), though is posted at 10-times finer spatial resolution. The InSAR DEM reveals small-scale features that the previous ICESat DEM is too coarse to resolve, including nunataks in the southern part of the FIIC and the location of the ice margin. The maximum elevation of the FIIC is estimated to be 960 m. Ice thickness at the central summit has been measured to be 535 m (C. Laing, unpublished data, 2009). We estimate the surface elevation to be 710 m at the same location and so the ice cap is grounded 175 meters above sea level (m.a.s.l.) here.

We examined the InSAR DEM and the SAR amplitude imagery to establish which glaciers of the FIIC were land- and which were ocean-terminating. The surface elevation of glaciers A, B, C and D (Figure 4.6) decreases to zero at the terminus, which suggests that they are marine-terminating. This was confirmed by examining the SAR amplitude backscatter images. Elevation observed at the terminus of glacier E is around 70 m.

Surface elevations at the termini of glaciers F, G and H are well above the RMS error of our DEM and therefore land-terminating.

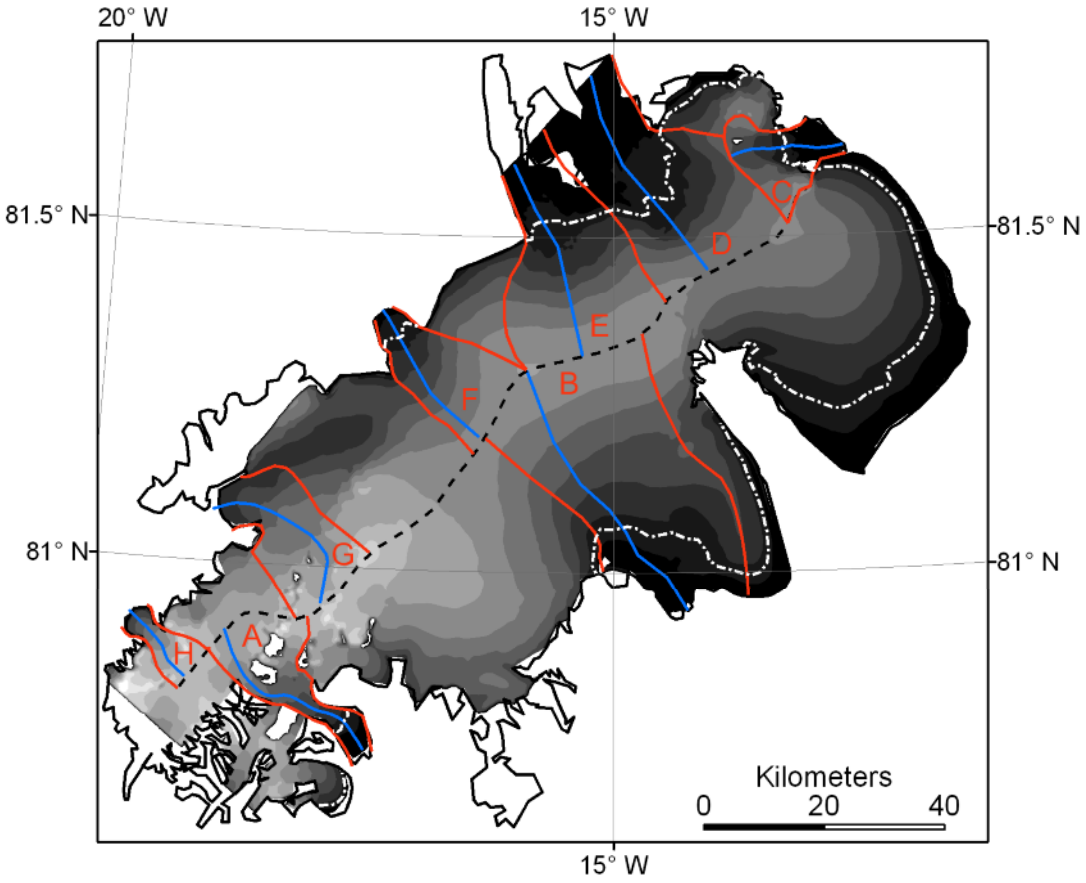

Figure 4.4. InSAR-derived DEM of the FIIC at 100 m intervals (greyscale) showing summit ridge (dashed black line), major surface catchments (red) and locations of outlet glacier transects (blue) shown in Figure 4.6. Also shown is the approximate position of the equilibrium line (dot-dashed white line) as predicted by Zwally and Giovinetto (2001).

We extracted elevation profiles from the InSAR DEM along the centre-lines of 8 outlet glaciers (Figure 4.6) of the FIIC in order to investigate the geometry of each glacier. While surface slopes at glaciers A, B and C are almost constant along their entire length, glacier D exhibits a distinct break in slope 9 km from the ice divide (Figure 4.6d). Above this break in slope, the topography of glacier D follows a convex profile from the ice divide at 600 m.a.s.l. down to the slope-break at 200 m.a.s.l. and the average slope of this section of the glacier is 2.5 degrees. Below the break in slope, the topography of glacier D follows a different profile; there is an abrupt change to an undulating surface of low slope (Figure 4.6d) down the ice front at a distance of 37 km from the ice divide. There are also several local topographic maxima along this section of the profile, most

notably at 31 km from the ice divide. The surface elevation of transect E (Figure 4.6e) shows a similar bi-modal profile to transect D; a break in slope after 14 km at 270 m.a.s.l. elevation separates the smooth and steep terrain exhibiting a convex profile at higher elevations and undulating low-gradient terrain at lower elevations. Glacier H (Figure 4.6h) exhibits the steepest mean slope of 3 degrees; elevation decreases from around 860 m.a.s.l. down to 150 m.a.s.l. at the glacier terminus 13.5 km from the ice divide.

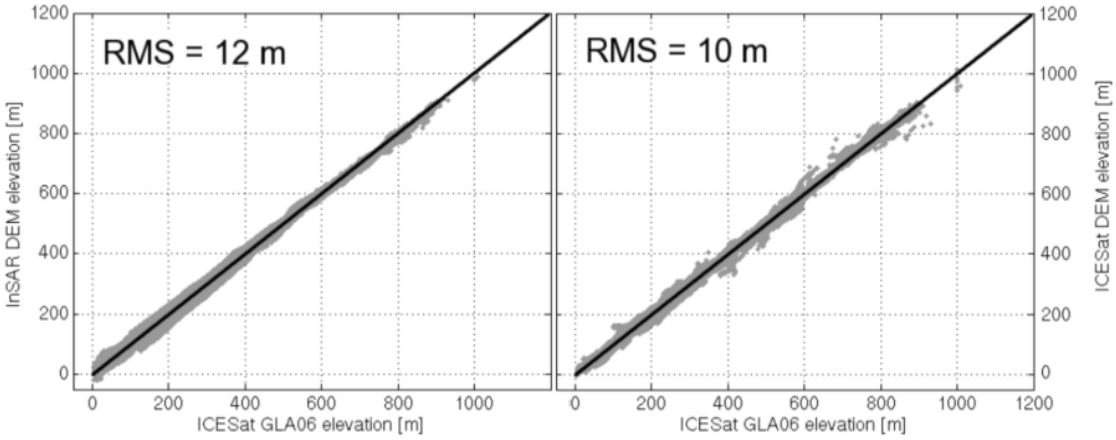

Figure 4.5. Comparison of ICESat point elevation data with (a) InSAR-derived DEM elevation and (b) ICESat DEM elevation (DiMarzio et al., 2007).

Finally, the InSAR DEM was used to delimit 8 glacier surface drainage basins, which range in area from 83 km^2 to 1048 km^2 (Table 4.2 and Figure 4.4). The largest catchments (glaciers B, D and E) flow perpendicularly away from the NE-SW oriented summit divide and are found in the central parts of the FIIC, while the smallest catchments (A, C and H) are located at the northern and southern limits of the ice cap. The drainage basins of tidewater glaciers have a mean area of 571 km^2; more than double the mean basin areaof the land-terminating glaciers (260 km^2).

4.6.2. Velocity data

We compared the InSAR ice speed estimates to feature-tracking speed estimates in order to investigate temporal variability in ice motion and to validate the InSAR dataset. Along each of the glacier centre flow-lines shown in Figure 4.4, we extracted InSAR and feature tracking velocity estimates (Figure 4.6). We assumed that errors for InSAR and feature tracking were independent and normally distributed and so we combined

them in quadrature when we compared velocity estimates. We defined differences to be significant when they are above the ~95 % confidence (2σ) level. Wintertime velocity was estimated from both InSAR and 35-day feature tracking data for 3 glaciers and typically agreed to within 5 ± 19 m yr^{-1} (Table 4.2, Figure 4.4). Agreement at glacier G was lower, but within the 95 % confidence interval at 28 ± 19 m yr^{-1}. Glacier A had the most complete coverage from feature-tracking data, which we show in Figure 4.7. There was agreement to within 6 ± 19 m yr^{-1} between the observed winter InSAR and tracking velocities over the interval 11 – 16 km and to within 3 ± 19 m yr^{-1} for the intervals 20 to 25 km and the final 5 km of the transect (Figure 4.6). Summer tracking velocities (day 201 – 237) were also calculated over the final 5 km of the transect and were found to be higher than the day-237 InSAR velocities by 43 ± 14 m yr^{-1} (Figures 4.6 and 4.7). Wintertime tracking data at glacier G for the interval 21.5 km to 23.5 km gave a mean value of 121 ± 18 m yr^{-1}; 21 ± 19 m yr^{-1} lower than the InSAR wintertime value over the same section which within 2σ of the error (Figure 4.6).

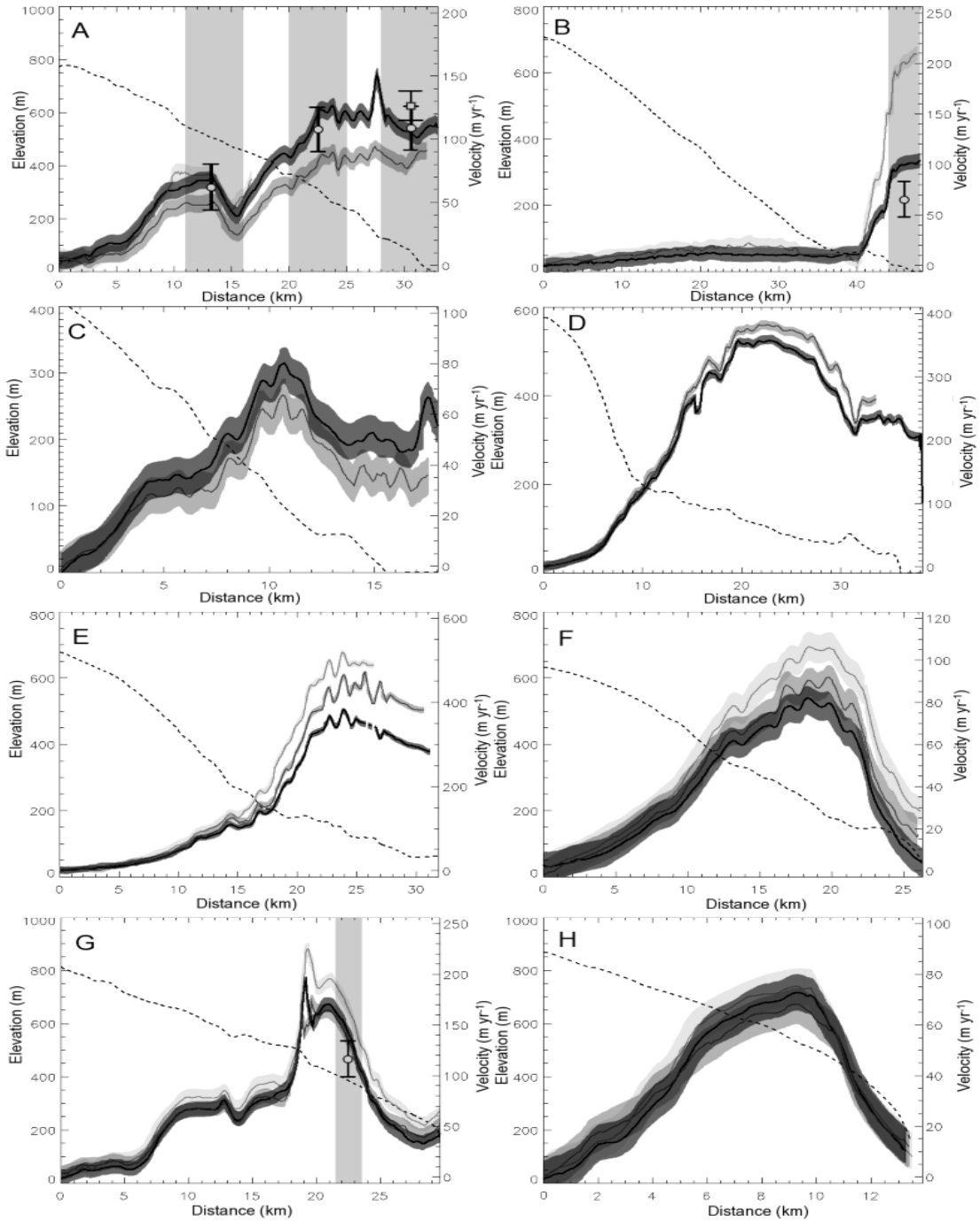

Figure 4.6. Along-transect InSAR-derived elevation (dashed line), wintertime velocity (thick black line), day-228 velocity (light grey line) and day-237 velocity (mid grey line) for catchments A to H shown in Figure 4.4, with associated error bounds shown as shaded areas. Where available, wintertime (open circle) and summertime (open square) velocities with error bars estimated from 35-day SAR feature tracking are also shown. Values are averaged over the width of the shaded column.

We compared the InSAR velocities to point measurements of ice motion derived from feature tracking of aerial photos taken in 1961 and 1978 (Higgins, 1991) to investigate

inter-annual variations in ice speed at FIIC. Previous observations of the two fastest glaciers (Higgins, 1991) were made at two locations (see Figure 4.1). The 17-year mean velocity observed at locations 1 and 2 were 360 m yr^{-1} and 175 m yr^{-1} respectively. We observe corresponding velocities of 290 ± 7 m yr^{-1} and 220 ± 7 m yr^{-1} during winter 1996, and a velocity of 375 ± 7 m yr^{-1} on day-237 at location 1. The ice velocity determined by Higgins (1991) was intermediate between our winter and August observations at glacier E and ~45 m yr^{-1} (20 %) lower than our InSAR estimates of winter velocity at glacier D.

Winter InSAR velocity estimated at the FIIC is shown in Figure 4.7a. The winter velocity dataset covers 90 % of the FIIC; the mid-August (day-228) velocity dataset covers 60 % of the FIIC and the late-August (day-237) velocity dataset covers 82 % of the FIIC. A maximum winter velocity of the FIIC of 434 ± 7 m yr^{-1} was observed at glacier E, which rises to 581 ± 7 m yr^{-1} at the same location on day-228. Flow averaged over the area of the catchment is highest for the adjacent catchment D (~100 m yr^{-1} km^{-2}), and shows seasonal variations of less than 5 %. Slowest flow occurs during winter at glaciers C and H, while the slowest area-averaged flow is at catchment B (9 m yr^{-1} km^{-2}). Velocity measured along the centre-line of glacier G has an unusual profile shape as shown in Figure 4.6g. The winter InSAR velocity peaks sharply to 200 ± 7 m yr^{-1} at 19 km, after which it decreases to 150 ± 7 m yr^{-1} at 20 km and after which there is a second broader peak in ice speed of 170 ± 7 m yr^{-1} at 21 km. Below this there is a decrease to 30 ± 7m yr^{-1}, 2 km from the ice margin, then an increase to 40 ± 7 m yr^{-1} at the ice front. The sharp peak in velocity at 19 km corresponds to a section of steep slope as shown in the elevation profile (Figure 4.6g).

We investigated the extent to which land- and marine-terminating glaciers exhibited differing velocity profiles. Peak velocity at tidewater glaciers occurred at a mean elevation of 100 m, compared with 400 m for land-terminating glaciers (Table 4.2, Figure 4.6). At glacier B, peak velocity occurs at the glacier terminus while at glacier D it occurs roughly halfway down the glacier. Peak velocity at the remaining glaciers occurred at an intermediate position and was on average at a location 0.7 of the glacier length from the ice divide. Velocities at the terminus were on average about 200 m yr^{-1} for marine-terminating glaciers in contrast to 30 m yr^{-1} for land-terminating glaciers.

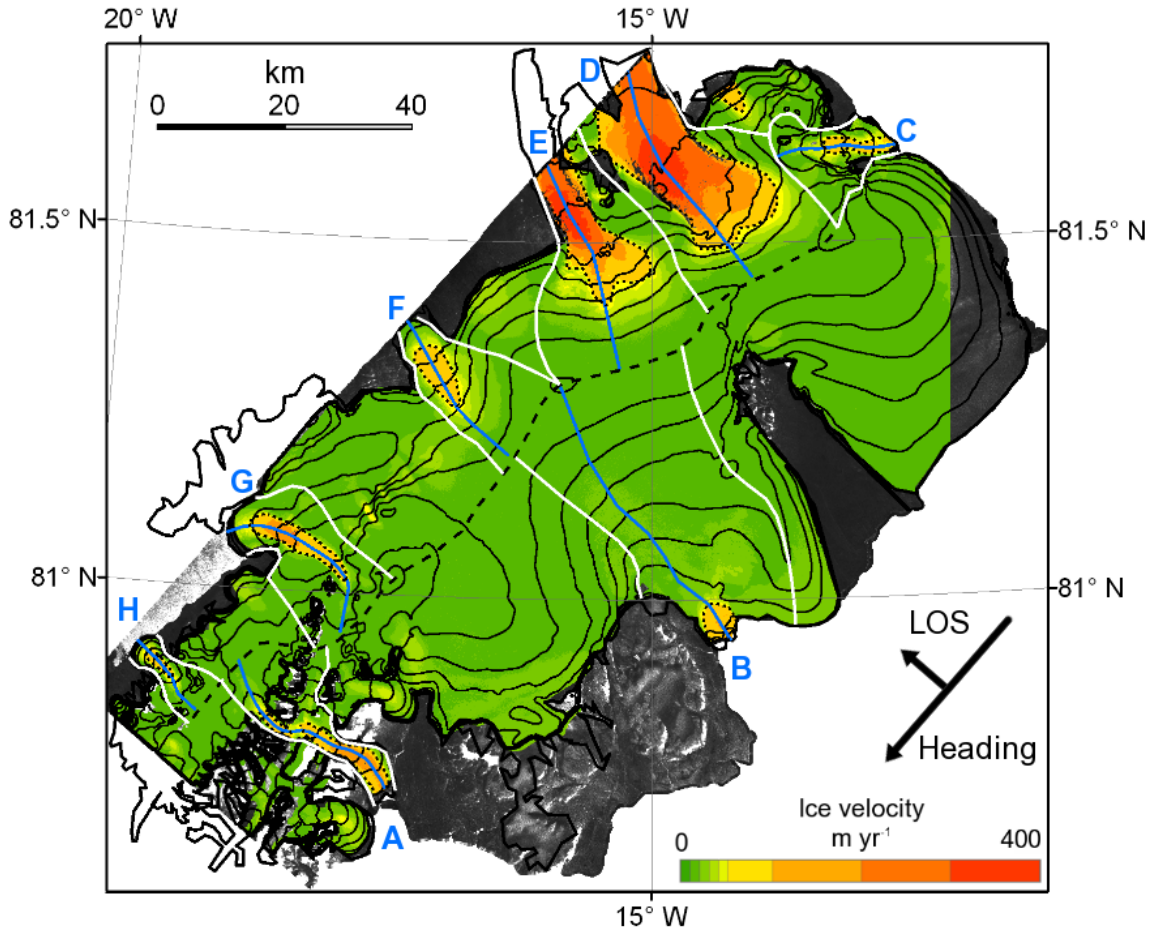

Figure 4.7.(a) Wintertime velocity measured during Winter 1996. Elevation contours at 100 m intervals and ice cap margin are shown in black. Shown inset are the directions of satellite heading radar and line-of-sight (LOS).The background is a SAR backscatter amplitude image.

4.6.2.1. Ice speed temporal change

Ice flow speeds at the majority of the FIIC are similar or greater in late-summer than in winter. For example, ice flow speeds on days-228 and-237 (Figures 4.7b and 4.7c) exceeded wintertime rates by 10 m yr^{-1} or more for 39 % and 30 % of the ice cap, respectively. In contrast, 0.5 % and 2 % of the surveyed area was observed to be flowing at speeds of less than 10 m yr^{-1} below the wintertime rates. Within catchments A and C, we observe slower ice speeds in late-summer than in winter (Figures 4.7a and 4.7c). Although

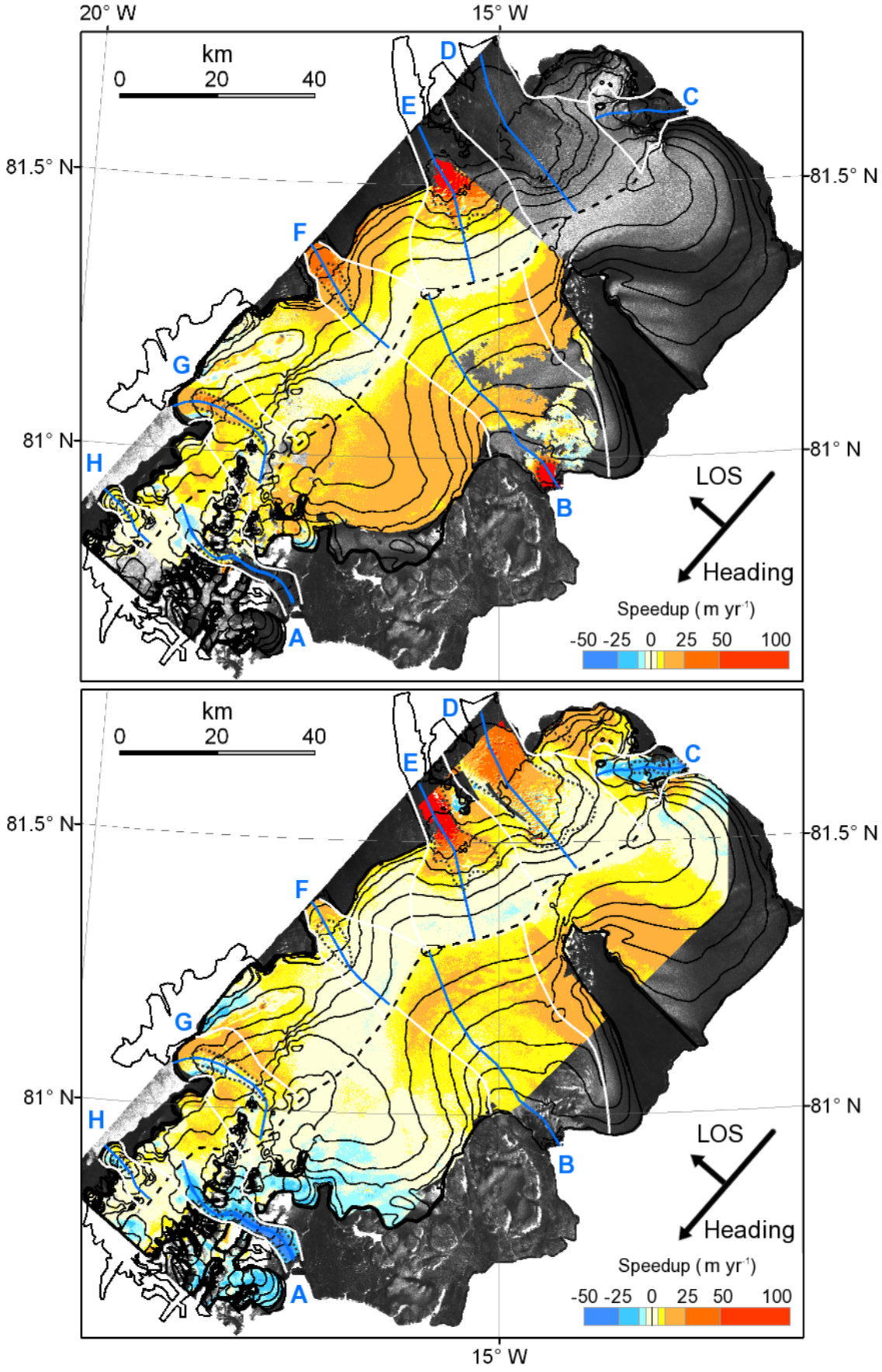

Figure 4.7. (b) speedup above winter speeds for day-228 and (c) day-237.

temporal fluctuations in velocity are observed at all glaciers, those recorded at glaciers C, G and H are of comparable magnitude to the estimated measurement error of ± 10 m yr^{-1}. The outlet glaciers of the FIIC exhibit a range of temporal fluctuations in ice flow speed which we broadly group into (i) glaciers exhibiting seasonal variations in ice flow speeds, and (ii) glaciers showing no significant temporal variation in flow speeds and discuss further below.

Glacier A exhibits significant temporal variations in ice flow speeds (Figure 4.8). The observed velocity on day-228 reaches a maximum of 75 ± 7 m yr^{-1} 10 km from the ice divide, 15 ± 10 m yr^{-1} faster than the winter speed at this point (6 months later), though this difference is not statistically significant. Day-228 data was unavailable below 16.5 km from the ice divide. Velocity observed 9 days later on day-237 follows a similar profile to winter, though 30 ± 10 m yr^{-1} slower, peaking at 95 ± 7 m yr^{-1} at 27.5 km.

Glaciers B, D and E also exhibit significant temporal changes in ice flow speed. At glacier E, speeds observed on both the day-228 and day-237 are higher and exhibit similar along-glacier profiles to winter. On day-228, the difference above winter (6 months later) reaches a maximum of 150 ± 7 m yr^{-1} at the peak velocity of 530 ± 7 m yr^{-1}, which occurs 24 km from the ice divide. On day-237, the maximum difference above winter velocity (6 months later) of 100 ± 10 m yr^{-1} occurs at 25.5 km from the ice divide, where a maximum speed of 480 ± 7 m yr^{-1} was observed. Although mid-August data does not extend over the whole of glacier D and late-August data does not extend over the whole of glacier B, we include both glaciers in this group. Transect B shows that day-228 velocity remains around 20 ± 7 m yr^{-1} up to 40 km from the divide, where it increases to 200 ± 7 m yr^{-1}, roughly double the winter rate (measured 6 months later). Ice speed measured at glacier D on day-237 exhibits a similar profile shape to winter and the difference in speed increases with along-transect distance. Ice speed reaches a maximum of 385 ± 7 m yr^{-1} at a distance of 23 km (25 ± 10 m yr^{-1} greater than winter speed measured 6 months later), and is around 30 ± 10 m yr^{-1} faster than winter speed over the final few kilometers.

At glacier F, both day-228 and day-237 velocity follow a similar profile to winter velocity, with a maximum of 105 ± 7 m yr^{-1} at 18.5 km and a maximum of 92 ± 7 m yr^{-1} at 20 km, respectively. Velocity differences above the winter at the terminus are 25 ± 10

m yr^{-1} (terminus speed of 28 ± 7 m yr^{-1}) on day-228 and 12 ± 10 m yr^{-1} (terminus speed of 15 ± 7 m yr^{-1}) on day-237, the latter being within the 95% confidence interval of measurement error.

Glaciers C, G and H exhibit temporal fluctuations in speed within the error of ± 10 m yr^{-1} and we classify them as having no significant temporal changes in ice flow speed. Along transect G, day-228 speed shows a similar profile to that of winter, and is typically 10 ± 10 m yr^{-1} faster, reaching a peak of 230 ± 7 m yr^{-1} at 19 km and a terminus velocity of 65 m yr^{-1}. Velocity observations from day-237 are similar to winter though without the peak at 19 km. Glacier H shows little variation from winter velocities during late-summer, and the maximum velocity difference between mid-August and late-August is a decrease of 10 ± 10 m yr^{-1}. Velocity measured on day-237 agrees well with the winter velocity up to 3 km from the ice divide, after which it shows a similar shape though 10 ± 10 m yr^{-1} slower. Ice within the final few kilometers shows a higher variability in ice speed in late-August than in winter.

Basin	Area (km^2)	Length (km)	Type	Velocity (m/y) Winter 1996		Velocity (m/y) Day 228		Velocity (m/y) Day 237		Position of max velocity	
				mean	Max.	mean	max.	mean	max.	Distance from ice divide (km)	Elevation (m)
A	219	33	M	28	193	15*	96*	21	118	27.5 (0.83)	140
B	1048	48	M	9	158	18	256	20*	37*	48 (1.00)	0
C	203	19	M	15	83	-	-	14	84	10.5 (0.55)	100
D	751	42	M	101	399	-	-	104	423	22.5 (0.54)	100
E	636	32	M	55	434	57*	581*	55	532	24 (0.75)	150
F	299	26	L	19	87	32	124	18	90	18.5 (0.71)	220
G	398	30	L	26	237	25	272	20	241	19 (0.63)	500
H	83	13.5	L	15	83	22	87	14	73	9.5 (0.70)	550

Table 4.2. Outlet glacier statistics and attributes. Asterisks denote values from datasets without partial coverage of the glacier catchment. Abbreviations in the 'Type' column refer to marine- (M) of land-terminating (L)

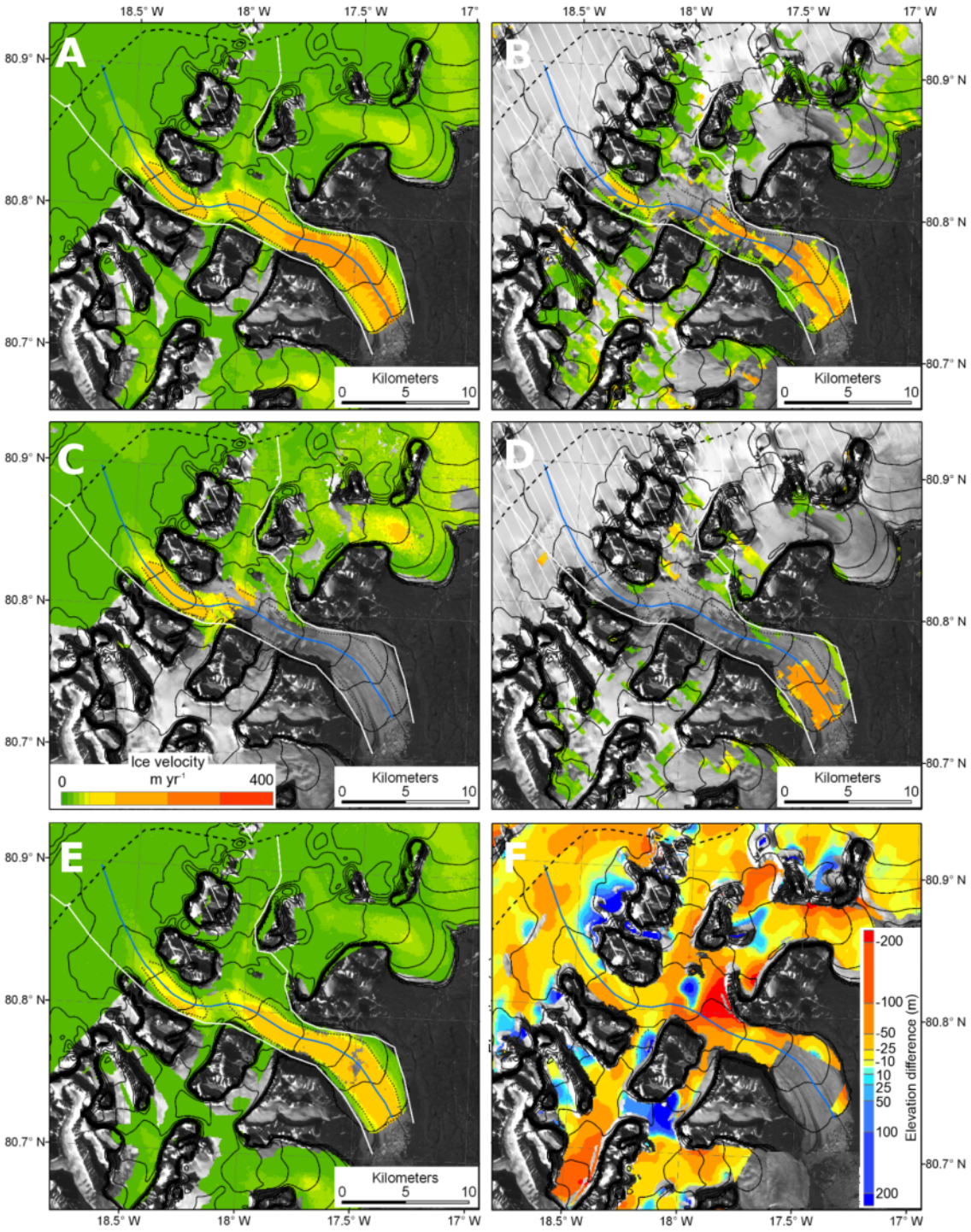

Figure 4.8. Enlargement of catchment A (Figure 4.4) showing velocity estimated from (a) InSAR during Winter 1996, (b) feature tracking during Winter 1996, (c) InSAR during day-228, (d) feature tracking during Summer 1995 and (e) InSAR during day-237. Also shown in panel (f) is elevation difference between the InSAR and ICESat DEMs (DiMarzio et al., 2007) shown in Figure 4.9.

4.7. Discussion

4.7.1. InSAR DEM

We examined in detail the apparent differences in elevation of the InSAR DEM with respect to external datasets. We compared the InSAR DEM with a previous ICESat-derived DEM (DiMarzio et al., 2007) of the ice cap (Figure 4.9). The RMS difference between the InSAR DEM and the ICESat DEM is 30 m, and 12 m between the InSAR DEM and the ICESat point measurements (Figure 4.5). Differences between our InSAR DEM and the ICESat DEM are due to a combination of errors in the ICESat and InSAR data, measurement of different surfaces due to penetration of SAR signal and detection of real changes in the geometry of FIIC between 1996 and 2003-2008. A previous comparison of the GLAS/ICESat laser altimetry Greenland DEM to a 5 km gridded radar altimetry DEM data set (Zwally and Brenner, 2001) indicated that the mean elevation difference of regions with surface slopes of 0.1° to 1.0° slopes is -24 ± 20 m, though this increases with local slope. An independent evaluation of the ICESat DEM (NSIDC, unpublished data, 2007) concluded that the horizontal spatial resolution of the DEM is approximately 7.5 km, despite the finer gridding scale for the data. At elevations above 600 m, our InSAR DEM consistently yields lower elevations than the ICESat GLAS (Figure 4.9). This is consistent with previous estimates of C-band radar penetration of dry snow in the percolation zone of up to ~15 m (Hoen and Zebker, 2000; Dall, 2001). Previous observations made between 1994 and 2007 suggest an elevation change rate of up to 60 cm yr^{-1} (Krabill et al., 2000; Pritchard et al., 2009) suggesting that differences in elevation between the 1996 InSAR DEM and the 2003-2007 ICESat flightline data of up to 5 m can be attributed to changes in the geometry of the FIIC.

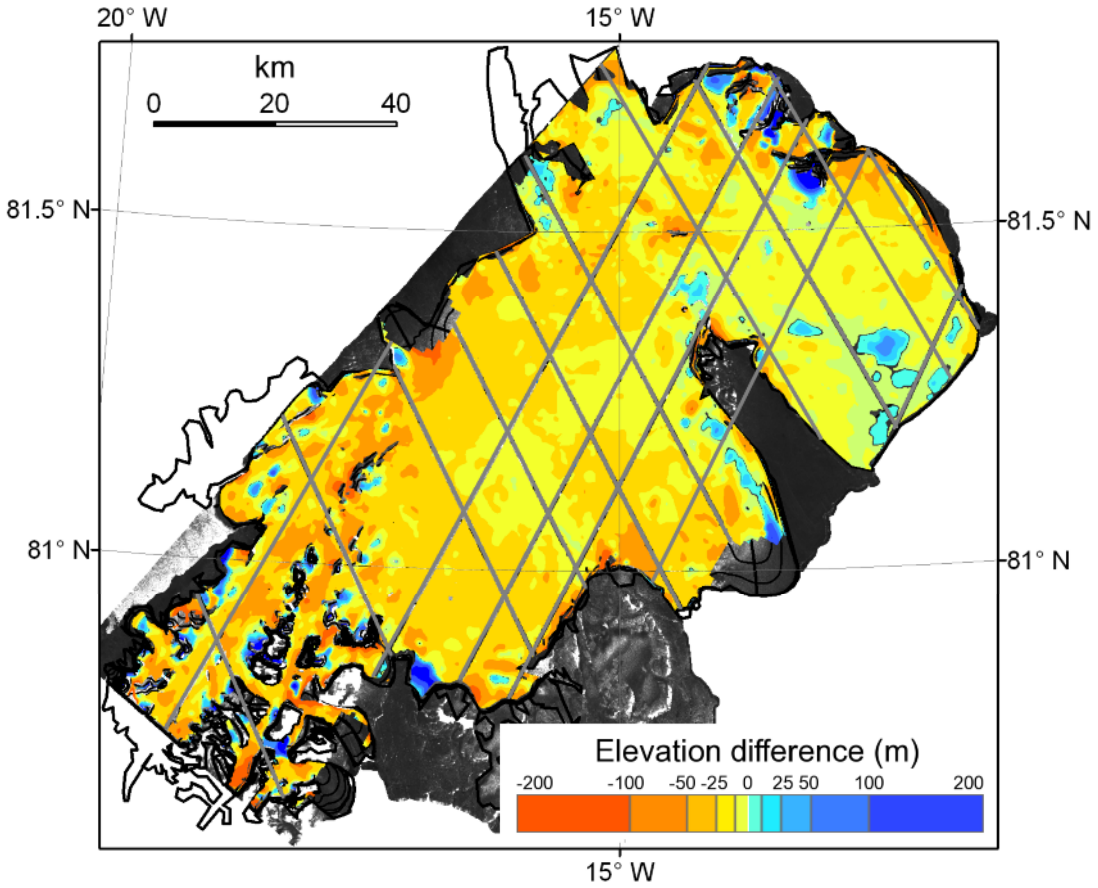

Figure 4.9. Differences in elevation estimated from the InSAR and ICESat DEMs (red to blue). Locations of ICESat point data flightlines used for calibrating the InSAR DEM are shown in grey. A SAR backscatter amplitude image is shown in the background and the ice margin is shown as a thick black line.

4.7.2. Ice velocity

We examined the extent to which there is agreement between the speed estimates derived from InSAR, feature-tracking and previous observations from aerial photos. During wintertime, the 1-day InSAR and 35-day feature tracking estimates of velocity agree within the 95 % confidence interval at all of the 5 locations. We estimated both summertime and wintertime velocity using 35-day feature-tracking over the final 5 km of transect A. While the wintertime InSAR and feature-tracking estimates agree within error, we found disagreement greater than 2σ of the error near the terminus of glacier A between the summertime tracking and InSAR velocity estimates of 40 ± 14 m yr^{-1} suggesting that ice speed at this location is more variable in late summer than in winter. Similar variability in late-summer ice speed has been observed for parts of the GrIS (Joughin et al., 2008) and may be related to seasonal changes in the subglacial drainage

system (e.g. Bingham et al., 2003). As glacier A is marine-terminating, there is the additional possibility that this variability in summertime flow could be due to tidally-forced vertical motion or tidal modulation of horizontal flow (Bindschadler et al., 2003). We observe faster flow at glacier D than was observed by a previous study (Higgins, 1991) suggesting that the glacier was flowing at around 45 m yr^{-1} (~20 %) faster in 1996 than it was during the period 1961 to 1978. However, it is important to point out that the large differences in the observation periods, which makes comparisons less meaningful – cyclical changes in ice flow speeds could be aliased. According to a recent study of ICESat elevation data, the lower reaches of catchment D have thinned by around 40 cm between 2003 and 2007 (Pritchard et al., 2009). This thinning is anomalous when compared to changes observed at the remainder of the western half of the FIIC, which thickened by around 2 m over the same period (Pritchard et al., 2009). We suggest these observations are consistent with the occurrence of surges at glaciers D and E at the time of the InSAR observations.

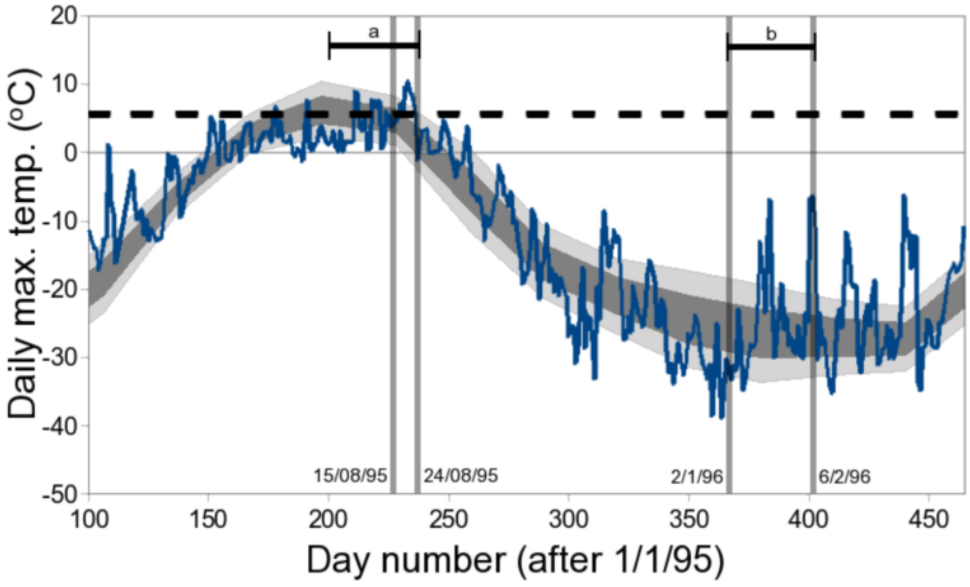

Figure 4.10. Daily maximum temperature at Station Nord (elevation 36 m.a.s.l.) (blue), plotted over the monthly mean of daily maximum temperatures for the period January 1986 to June 2009 ± 1 standard deviation (SD) (dark grey) and ± 2 SD (light grey). Vertical bars show the acquisition dates of the SAR data used to produce the InSAR velocity maps. Horizontal bars show periods over which we used feature tracking to estimate ice velocity.

Together with the results of a previous study (Higgins, 1991), our data provide evidence

for both seasonal and inter-annual fluctuations in the rate of ice flow at the FIIC. Glacier A showed highest velocities in winter and mid-August slowest flow in late-August. Glaciers B, D and E showed slowest flow in winter, fastest flow in mid-August and intermediate velocities in late-August. We show that glacier E exhibited small (5%) variation in velocity between winter and August. Glacier F sped-up in mid-august but returned to winter velocity at the end of August. No significant seasonal velocity differences were observed at glaciers C, G and H.

Other authors (Iken and Bindschadler, 1986; Bingham et al., 2003; Boon and Sharp, 2003) have observed changes in the rate of ice motion at Arctic glaciers and these have been attributed to seasonal variations in the amount of meltwater available for basal sliding. Similar observations have been made at the western margin of the GrIS (Zwally et al., 2002a; Das et al., 2008). Figure 4.10 shows that at the time of the fastest observed flow (day-228, 16th August 1995), the daily maximum air temperature measured at Station Nord (elevation 36 m.a.s.l.) was 4.5 °C (mean daily temperature was 4.2 °C), which is typical for this time of year. Using an August atmospheric lapse rate of 0.5 °C 100 m^{-1} (Steffen and Box, 2001), the melting level was at 900 m.a.s.l., meaning that almost the entire ice cap was above freezing and melted water was available to enhance sliding across all catchments. Slower-than-winter ice speeds observed during late-August at glacier A could be explained by the unusual meteorological conditions around the time of the August observations. Figure 4.10 shows that between day-228 and day-237, daily maximum temperatures measured at Station Nord were unseasonably high; up to 10.4 °C with 5 of the 9 intervening days having a daily mean air temperature above 5 °C. However, temperature measured on day-237 had a mean value of -1.2 °C and a maximum of -1 °C at Station Nord, representing an unseasonal 'cold-snap'. This warm period followed by a cold period when the day-237 velocities were observed may explain why ice speed was lower on day-237 than in winter. The many nunataks surrounding glacier A sugges that it is more confined by topography than most of the other outlet glaciers which may explain why the seasonality of ice motion differs form the other outlet glaciers.

It is possible that the apparent variability in flow speeds may be explained by measurement uncertainties, and so we investigated locations at which the variability is less than the estimated measurement error. Glaciers C, G and H show no variation in

flow above the estimated error between winter and August, though may have been flowing faster earlier in the year. Catchments C and H are the smallest catchments and therefore have the smallest runoff available to enhance basal sliding (Zwally et al., 2002*a*).

4.8. Conclusions

We have used InSAR techniques to produce a fine-resolution digital elevation model of the Flade Isblink ice cap in eastern North Greenland, and also to produce the first ice velocity maps of the ice cap. Each of the 2 summertime and 2 wintertime velocity maps represent 24-hours of motion and were acquired between 15th August 1995 and 3rd February 1996. We also estimated ice speed over 2 35-day periods in summer 1995 and winter 1996 using SAR feature-tracking techniques.

Our InSAR DEM is of 100 m resolution and of comparable accuracy to a widely used DEM of this area (DiMarzio et al., 2007). Our DEM has an accuracy of 12 m and covers 91 % of the FIIC. It reveals ice surface geometry in detail and provides information on the characteristics of the 8 major outlet glaciers, for example, that the marine-terminating glacier E is grounded. The highest slope was 3 degrees at a glacier in the southern part of the FIIC which was flowing into a lake. The DEM is used to delineate ice surface drainage basins, which range in area from 83 km^2 to more than 1000 km^2. Tidewater glaciers have on average twice the area of land-terminating catchments. There are differences (RMS difference is 30 m) between our DEM and a previous DEM (DiMarzio et al., 2007), which we suppose arise due to a combination of radar penetration in the percolation zone, detection of surface elevation changes and inherent errors in each of the elevation models.

We mapped velocity of 90 % of FIIC in winter 1996, 82 % in mid August 1995 and 60 % in late-August 1995. The velocity data reveal that the FIIC is drained by a mixture of land- and marine-terminating glaciers. Summer velocities were observed to be more variable than winter velocities at one of the outlet glaciers. We observe 20 % faster ice flow in winter 1996 than the mean flow observed between 1961 and 1978 in a previous study (Higgins, 1991), although the observation periods varied in duration. Our

observations are consistent with the occurrence of glacier surges at catchments D and in 1995/1996. A greater variation in the position of peak velocity is observed for marine-terminating glaciers than for land-terminating glaciers. Peak velocity occurred roughly 0.7 of the distance between the ice divide and terminus for two thirds of the glaciers, at the terminus for one marine-terminating glacier and halfway between the ice divide and terminus for another. Peak velocity also occurred at lower elevations (~100 m) for marine-terminating glaciers than for land-terminating glaciers (~400 m). Each glacier can be classified based on its temporal variations in flow speeds into one of four distinct groups. No variations greater than 2σ above the measurement error was observed for three of the smallest glaciers. Our results reveal a large range of seasonality in the glaciers draining the FIIC and suggest that there is no simple relationship between glacier type and seasonality of motion. We suggest that detailed study of individual outlet glaciers is required to improve our understanding of the processes governing the ice dynamics of similar ice masses.

Chapter 5: High variability in seasonal acceleration of the Greenland ice sheet due to routing of surface water.

This Chapter describes the application of repeat-pass InSAR techniques in order to derive ice elevation and velocity for a land-terminating sector of the Greenland ice sheet. This chapter has been submitted for publication to Geophysical Research Letters:

Palmer, S.J., Shepherd, A., Nienow, P., Joughin, I. (Submitted), High variability in seasonal acceleration of the Greenland Ice Sheet due to routing of surface water. *Geophysical Research Letters.*

I processed the InSAR velocity data, interpreted the results and wrote the manuscript. Shepherd assisted with the data processing, interpretation and formulation of the manuscript. Nienow contributed to the interpretation of the results. Joughin provided the feature tracking data used to calibrate the InSAR velocities.

5.1. Abstract

We use interferometric synthetic aperture radar data from western Greenland to quantify temporal variations in ice sheet flow and to characterise the ice sheet surface hydrology. Our data reveal a non-uniform pattern of late-summer velocity increase that extends over 100 km inland. Spatial variations in velocity are correlated with the routing of supraglacial water, and the magnitude of late-summer speedup is positively correlated with modelled runoff ($r = 0.78$). At this time, ice beneath the largest catchment flows on average 48 % faster than in winter; beneath smaller catchments changes are less pronounced. Our results provide a basis for modelling the dynamical response of the Greenland ice sheet as the degree of melting at the surface evolves - a process that has been often considered for Alpine glaciers. If the routing of supraglacial water affects ice velocities throughout the remainder of summer, ground-based experiments to study seasonal velocity fluctuations should be sited with care to avoid sampling areas which exhibit modest variability.

5.2. Introduction

The Greenland Ice Sheet (GrIS) moves through a combination of internal deformation and basal motion. Previous studies have shown that ice motion in western Greenland exhibits seasonal variability of up to 100 % (Joughin et al., 2008; van de Wal et al., 2008; Zwally et al., 2002) and it has been suggested that direct coupling between surface melting and ice dynamics provides a mechanism for this effect (Zwally et al., 2002). The link between surface melting and enhanced ice motion, resulting from high basal water pressures, has long been recognised in temperate glaciers (Iken and Bindschadler, 1986). More recent observations have shown that surface water can reach the base of thick, cold ice via crevasses and moulins (Bingham et al., 2003; Das et al., 2008). In Greenland, seasonal accumulation of water in supraglacial lakes (McMillan et al., 2007) is a potential factor in establishing such conduits through hydrofracture (van der Veen, 2007), and those that form at the base of drained lakes often lie near the confluence of melt-water streams so will continue to route surface meltwaters to the bed after lake drainage (Das et al., 2008). However, both the extent to which water melted at the GrIS

surface modulates ice flow and the structure and stability of its englacial and subglacial drainage systems are poorly understood.

Fluctuations in the flow of ice sheets affect their mass through a number of processes, including changes in the discharge rates of marine-terminating glaciers (Rignot and Kanagaratnam, 2006) and changes in the hypsometry of land-terminating glaciers which may, in turn, lead to altered rates of accumulation and ablation. Although the most recent assessment of the Intergovernmental Panel on Climate Change (Meehl et al., 2007) did not account for the impact of potential increases in the degree of melt-induced acceleration on the future sea level contribution of the GrIS, an earlier attempt to parameterise the effect (Parizek and Alley, 2004) predicted a 10-25 % greater rate of ice loss over the next century. However, our ability to incorporate melt-induced acceleration into dynamical models of the GrIS and thereby simulate its evolution in a warming climate is limited by a lack of knowledge of the extent and structure of the hydrological forcing.

5.3. Data and methods

We processed seven synthetic aperture radar (SAR) interferograms acquired between 11th August 1995 and 2nd May 1996 by the European Remote Sensing (ERS) satellite to derive ice sheet topography and motion (Goldstein et al., 1993) across 1-day intervals. Wintertime interferograms were differenced and combined with sparse elevation measurements acquired by airborne laser altimetry (Krabill et al., 1995) to form a new digital elevation model (DEM) of a 9 800 km^2 sector of the GrIS (Figure 5.1). Using this DEM, we removed the topographic phase signal from each interferogram and, from the adjusted data, we estimated ice movement. Surface motion was typically 5 to 10 times greater than that due to rates of ice uplift measured in this area of the GrIS during summer (Shepherd et al., 2009), and therefore we suppose they are associated with horizontal ice flow. We estimated flow rates (e.g. Figure 5.1) assuming that ice moved parallel to its surface and in the direction of maximum slope (Joughin et al., 1998) using sparse estimates of ice motion derived from 24-day radar speckle tracking (Figure 5.3) as an absolute reference. The velocity maps ranged in extent between 4 000 and 9 300 km^2, due to variations in interferometric coherence and interferogram coverage.

To characterise spatial variations in the routing of supra-glacial water, we estimated the degree of ice melting using a positive degree day (PDD) model (Reeh, 1991), and we delimited the principal features of surface hydrological catchments (boundaries, streams, and lakes, see Figure 5.2) using the InSAR-derived DEM. We used surface air temperatures recorded at Kangerlussuaq airport during the period 1995 to 2006 and a time-varying atmospheric lapse rate (Steffen and Box, 2001) to model PDDs across the survey area. From these data, and an estimate (300 mm $year^{-1}$ water equivalent) of winter snow accumulation (Hanna et al., 2005), we modelled runoff rates across the survey region. To establish how surface water was routed, local topographic minima (sinks) were filled and we assumed that flow was in the direction of maximum surface slope. We estimated the quantity of runoff accumulated within each catchment (Table 5.1) by considering the integrated flow through adjacent grid cells upstream.

5.4. Results

5.4.1. Ice velocity variations

The velocity data (Figure 5.1) show that large portions of this sector of the GrIS margin sped-up during late-summer 1995, but also that other portions did not. Although our InSAR data cover a smaller fraction of the ice sheet margin and are more sparsely sampled than previous surveys (Rignot and Kanagaratnam, 2006; Joughin et al., 2008), they are of finer spatial and temporal resolution and extend much farther inland. The fastest period of ice flow was recorded on 11th August 1995 (day-223, relative to 1st January 1995), followed by a rapid deceleration over 19 days to speeds that remained approximately constant throughout the remainder of winter (Figure 5.3). During early May 1996, ice velocities were moderately greater than those observed during the preceding winter period. We were unable to recover data for the area between the ice margin and the 900 m elevation contour. This was due to loss of phase coherence caused by changes in the scattering volume between SAR data acquisitions. Given the time of year, these changes are most likely due to surface melting below 900 m elevation.

The timing of ice velocity fluctuations is consistent with seasonal changes in the rate of ice melting at the surface of the GrIS (Figure 5.3) and, although our InSAR data are of

high accuracy and are spatially extensive, their temporal resolution is not sufficiently fine to determine the duration of enhanced flow with confidence. In 2006, however – a year during which melting in Greenland was comparable to that in 1995 (Box et al., 2006; Hanna et al., 2005) – sparse estimates of ice velocity close to the ice sheet margin derived from radar speckle tracking (Figure 5.3) (Joughin et al., 2008; Shepherd et al., 2009) show that the period of enhanced summer motion lasted from around day-130 to day-235, a range that is consistent with our observations.

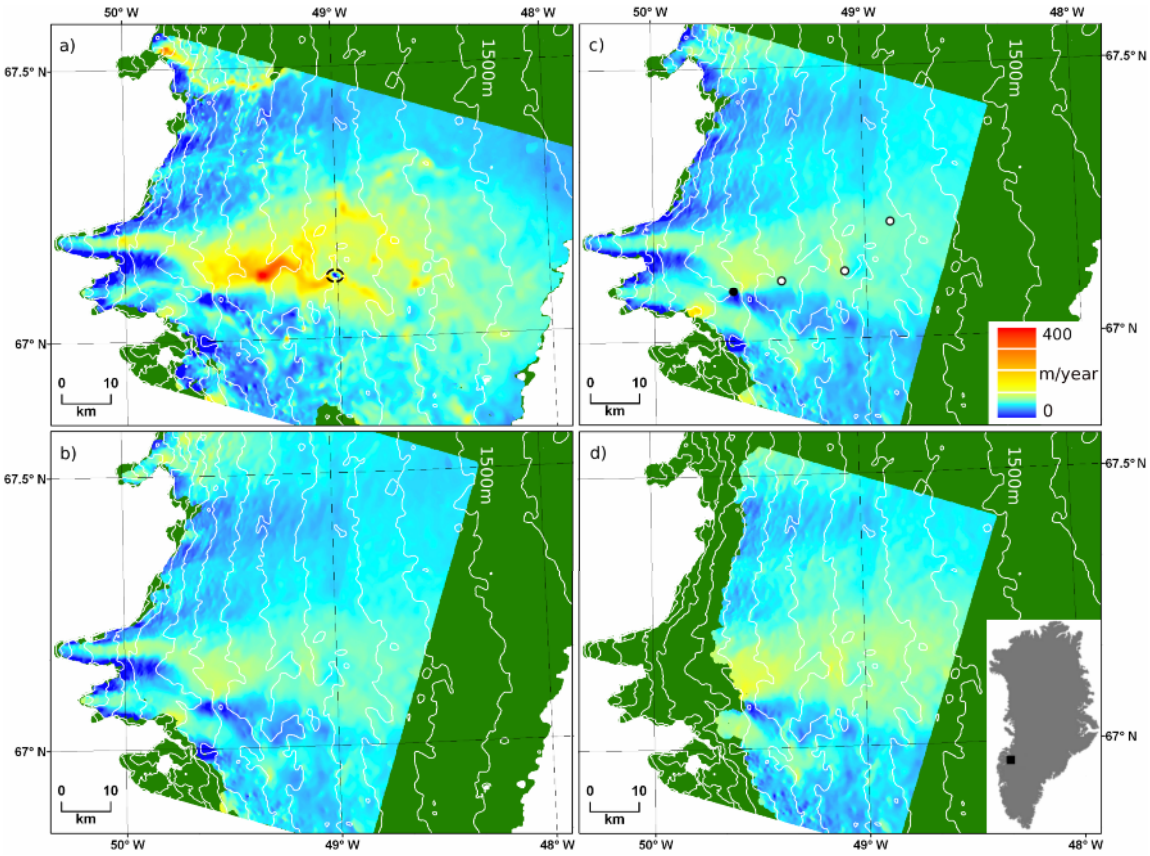

Figure 5.1. Speed of a land-terminating sector of the Greenland Ice Sheet (inset) determined using InSAR in late-summer (a) (11-12 August, 1995) and (b) (30-31 August, 1995); winter (c) (20 October 1995 – 3rd February 1996); and spring (d)(2-3 May, 1996). Elevation contours at 100 m intervals (white) and locations used to determine absolute values of ice motion (white circles in (c)). The data in Figure 5.3 was extracted at the location of the black circle in panel (c). Also shown in panel (a) is the location of a site of possible vertical motion discussed further in chapter 6.

Although late-summer velocities were enhanced across much of the 7 000 km^2 velocity-

survey region and extend far inland, our data show that the speedup is not uniform and at many locations there is no variability at all. The maximum observed speedup was 304 m $year^{-1}$ (360 %) at a location 31 km from the ice sheet margin. However, just 2 % of our study area showed a doubling of ice velocity in late-summer, and no significant (10 % or less) change was observed in 15 % of the survey area. Our data also show that the majority of sites included in a recent GPS survey of the ice sheet motion (van de Wal et al., 2008) show no significant speedup in late-summer (see Figure 5.2).

Catchment	Area (km^2)	Summer speedup (%)	Number of sinks	Runoff (10^6 m^3)
Inugpait quat (INU)	430	47	19	52
Avangnardleq (AVA)	1500	31	40	81
Qigssertaq (QIG)	98	17	1	12
Kautorissat isuat (KAU)	140	18	4	13
Akuliaruserssuq North	900	25	22	58
Akuliaruserssuq South	130	17	3	18
Isunnguata sermia (ISU)	2400	48	45	154
Russell Glacier (RG)	1200	32	28	105
Orkendalen (ORK)	60	1	1	9
Perserajut (PER)	110	1	3	18
Total/average	6968	35	166	522

Table 5.1. Basin area, average late-summer speedup, number of sinks and modelled runoff accumulated during the 5 days preceding the late-summer velocity observations or each of the catchments shown in Figure 5.2.

5.4.2. Routing of surface water

We investigated the extent to which the pattern of seasonal acceleration was correlated with spatial variations in the degree of surface melting. Our analysis (Table 5.1 and Figure 5.2) shows that there are 10 major drainage catchments. Although a number of the hydrological catchments are incomplete due to limitations in the extent of the InSAR elevation model, our data cover almost all of the area in which ice melting occurs (the equilibrium line is located at ~1500m (van de Wal et al., 2008)). A straightforward

comparison shows that the speedup of ice in August is greatest in the largest catchments (Table 5.1), and there is a positive correlation ($R^2 = 0.61$) with the quantity of runoff accumulating within each catchment during the 5 days prior to each InSAR image pair (Table 5.1). We choose 5 days as a rough estimate of the period during which water resides in the hydraulic system, although similar correlations exist when considering runoff accumulated over shorter and longer time intervals. That the glaciers with larger quantities of runoff generated within their hydrological catchments exhibit the largest increases in late-summer ice velocity changes is suggestive of a close link between surface hydrology and ice dynamics, and supports similar conclusions based on localised ground-based surveys (Zwally et al., 2002; Shepherd et al., 2009).

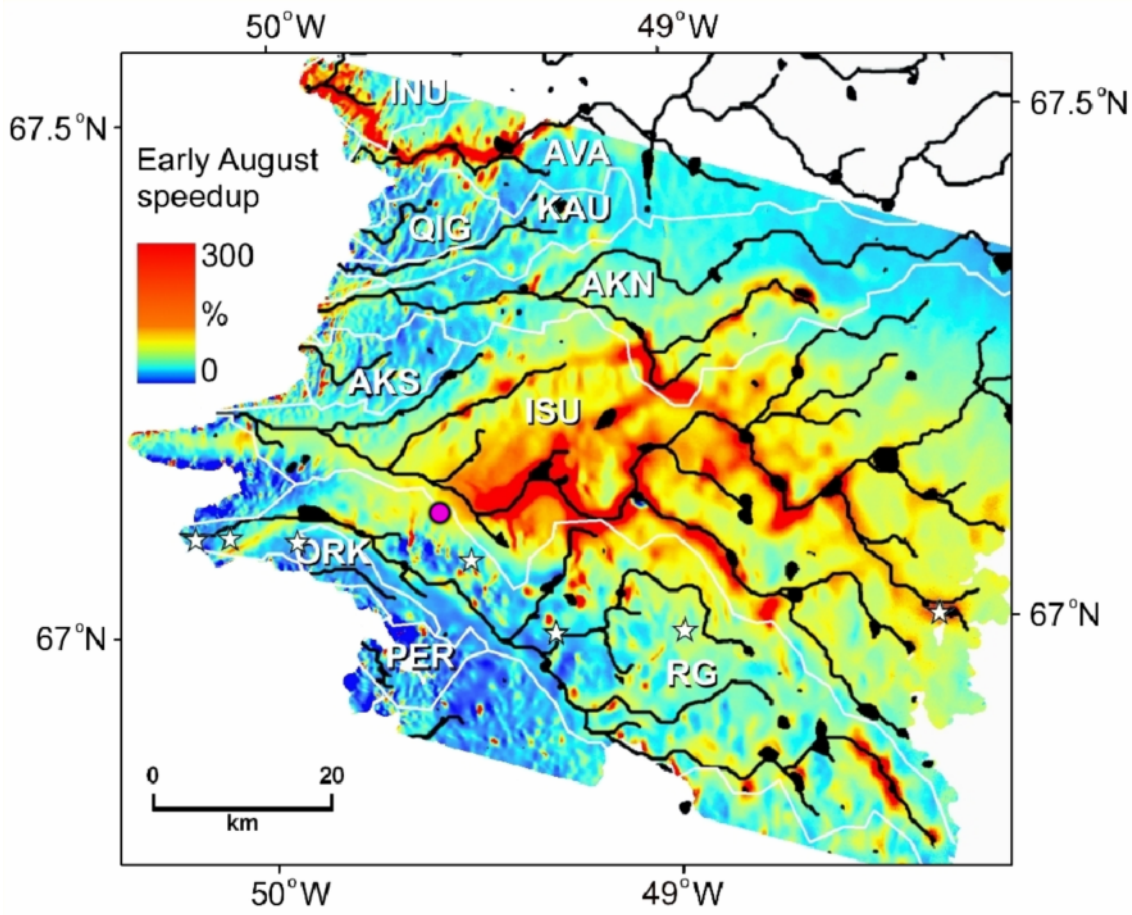

Figure 5.2. Supra-glacial hydrological catchments (white lines, Table 5.1) superimposed on a map of seasonal (late-summer minus winter-average) velocity change (colour scale). Also shown are melt-water streams (black lines), topographic sinks (coloured black), and the location of the K-transect (van de Wal., 2008) (white stars). Ice speed data presented in figure 5.3. were acquired at the location marked with

a purple circle.

There is also a positive correlation ($R^2 = 0.62$) between the degree of ice speedup and the distribution of topographic sinks (Figure 5.2) across the ice sheet surface – features that correspond to the location of supra-glacial lakes on the ice sheet surface (McMillan et al., 2007). These sites have been identified as potential sources of conduits allowing water to travel from the ice sheet surface to its base (Das et al., 2008). A more detailed understanding of the link between surface melting and ice acceleration will require a consideration of the dates on which supra-glacial lakes drain (e.g. Sundal et al., 2009).

5.5. Discussion

We suggest that around the time of our late-summer observations, the channelized subglacial drainage system was overwhelmed by a large input of surface water, resulting in elevated basal water pressures, reduced basal friction and faster ice flow (Zwally et al., 2002). Other factors will affect the extent to which surface water causes localised ice acceleration, such as the potential routing of water at the ice sheet base according to the bedrock geometry (Wingham et al., 2006). A notable example of such behaviour is the flow of Inugpait Qaut (Figure 5.2), where the main flow in August originates in the supraglacial hydrological catchment of the neighbouring Avangnardleq. We suppose that the junction at which ice flow crosses surface hydrological catchments coincides with the routing of water, subglacially, associated with a gradient in hydraulic potential governed by changes in bedrock elevation. The piracy of surface water from a neighbouring supra-glacial catchment explains also the relatively poor correlation between catchment area and speedup for this glacier (Table 5.1).

Fluctuations in the flow of ice sheets can affect their mass in numerous ways. Although most of the reported doubling of ice discharge from the GrIS over the past ~10 years (Rignot and Kanagaratnam, 2006) is apparently driven by processes occurring at the ice sheet margin (Joughin et al., 2008), it is estimated (Joughin et al., 2008) that the lubricating effects of increased summer melting account for only a few percent increase in mass loss from the ice sheet annually. Given that the degree of surface melting at the GrIS is expected to increase progressively over the coming century (Meehl et al., 2007),

however, even a slight imbalance would compound. In addition to affecting the discharge of marine-terminating glaciers, flow variations driven by surface melting will affect the ice sheet surface mass balance through a progressive change in hypsometry; the sectors of the GrIS that do not experience melting will diminish over time. Changes in the GrIS geometry would also affect the number and distribution of supra-glacial lakes (McMillan et al., 2007), features that are known to factor in the process of basal lubrication (Das et al., 2008). Finally, if the marine-terminating sectors of the GrIS progressively retreat, the role of land-terminating sectors will govern the longer-term evolution of the ice sheet mass so a detailed understanding of their response to warming is of importance.

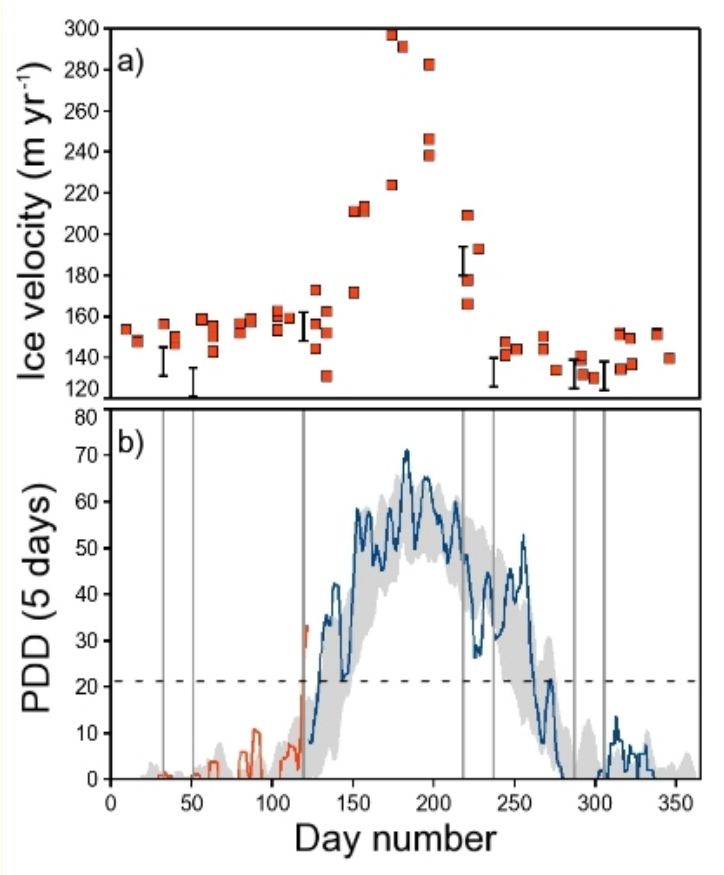

Figure 5.3. (a) Ice speed at a location (black circle, Figure 5.1) where InSAR (black) and radar speckle-tracking (orange squares) were both available. Error bars for the InSAR velocity values are ± 5 m yr^{-1} s. e. m. (b) Positive degree-days recorded at Kangerlussuaq airport integrated over five-day periods in the years of our InSAR survey (1995, blue; 1996, orange) and over the 11-year period of the temperature observations (1995-2006, grey). Also shown (dashed line) is the approximate PDD offset to account for reduced air temperatures at the elevation of the velocity observations.

Although the correspondence between flow-variability and the routing of supraglacial water is striking in late-summer (Figure 5.2), it is possible that such a relationship does not hold at other times. While other data (e.g. Figure 5.3a) confirm that the seasonal variations in flow are common in this sector of the GrIS, the relationship can be complicated by sudden events, such as the drainage of nearby supra-glacial lakes (Joughin et al., 2008, Das et al., 2008, Shepherd et al., 2009). Moreover, the extent to which the structure of Figure 5.2 is representative of the manner in which velocity variations occur during the remainder of summer is not certain. Ground-based data, for example, are equivocal: although GPS observations (Shepherd et al., 2009) recorded near to the centre of Isunnguata Sermia (circles, Figure 5.1) reveal diurnal velocity

fluctuations amounting to a degree of seasonal variability that is comparable to that of our InSAR data, other data (van de Wal et al., 2008) recorded along a transect of Russell Glacier (stars, Figure 5.3) show seasonal variability in a region where the InSAR data record little apparent change. A more extensive InSAR dataset (including early summer) would help to clarify the relationship between surface melting and ice flow.

5.6. Conclusions

We have used InSAR to produce an elevation model of a 10 000 km^2 and 7 ice velocity maps of a 7 000 km^2 sector of the GrIS. Our results from late-summer in 1995 show that ice velocity was enhanced far (100 km) inland by up to 360 % over the average winter rate. The degree of ice speedup is correlated with many aspects of the ice sheet surface hydrology, including the area and quantity of runoff generated within surface hydrological catchments, and the distribution of supraglacial lakes. We conclude that the observed seasonal velocity fluctuations are controlled by surface melting. In contrast to a previous study (Joughin et al., 2008), our InSAR data shown that there is significant spatial variation in the incidence of late-summer ice speedup and that the effect extends to great distances inland. The areas of largest speedup are closely correlated with large scale melt-water channels on the ice sheet surface (Figure 5.2) and we suppose that water is routed sub-glacially directly below these features.

Because the degree of seasonal flow variability appears to be so variable, it is important to consider in detail the siting and interpretation of ground-based ice velocity measurements. In consequence, it may be premature to conclude that that a warming climate will have limited implications for the evolution of the GrIS. The non-uniform distribution of seasonal ice velocity variations also indicates that a complexity exists in the relationship between melting rates, drainage conditions and ice motion. Because variations in ice flow affect the mass balance of ice sheets in numerous ways, our data show that an improved understanding of the evolution of the GrIS over the coming century requires that simulations of the ice sheet response to expected climate warming include an appreciation of the coupling between surface and basal hydrology.

Chapter 6: Synthesis and conclusions.

6.1. Introduction

This thesis has investigated the utility of interferometric synthetic aperture radar (InSAR) techniques for detecting temporal fluctuations in the flow of land- and marine-terminating glaciers over timescales that are sufficient to illuminate the underlying physical processes that govern such changes. An incomplete understanding of the physical processes that control ice dynamics has been identified as a major uncertainty in current predictions of the response of Arctic land ice to climate change (Solomon et al., 2007). In order to address these uncertainties, I determine the velocity of ice caps and glaciers across seasonal and inter-annual timescales (chapters 3, 4 and 5), and I use these data to analyse the complex temporal fluctuations in ice motion exhibited by a range of individual glaciers. In chapter 5, I reveal seasonal changes in the flow of a land-terminating sector of the Greenland ice sheet (GrIS), and I investigate the role of surface melting as a control on the observed patterns of motion. More specifically, this thesis has achieved, through the application of satellite InSAR techniques, the following research objectives:

1. to derive the first ice velocity map of the 925 km^2 Langjökull ice cap (LIC), a land-terminating ice cap in Iceland, using repeat-pass, dual-azimuth InSAR, and to compare these observations with independent GPS measurements of ice velocity to investigate inter-annual variations in rates of ice flow (Chapter 3).
2. to derive the first ice velocity map of the 8500 km^2 Flade Isblink ice cap (FIIC), an ice cap in eastern North Greenland drained by a mixture of land- and marine-terminating glaciers, using repeat-pass InSAR, and to investigate seasonal variations in rates of ice flow (Chapter 4).
3. to measure seasonal variations in rates of ice flow up to 100 km inland at a 7000 km^2 land-terminating sector of the western GrIS using repeat-pass InSAR, and to investigate the role that surface meltwater plays in the summertime speed-up (Chapter 5).

This Chapter presents a summary and a synthesis of the main thesis conclusions obtained through completion of the objectives outlined in Chapter 1. Section 6.2 provides a summary of the principal conclusions drawn from studying temporal fluctuations of the flow of the LIC, FIIC and the WGrIS. Section 6.3 presents a synthesis of the collective findings and highlights the implications of each in turn. Section 6.4 discusses the results presented in this thesis in the context of efforts to assess the impacts of climate warming on ice dynamics (e.g. Solomon et al., 2007). In section 6.5 I discuss the limitations of this work and how it could be improved. Finally in Section 6.6 I outline potential directions for future research at each of the three study areas, and consider the possibilities that may arise through data from planned satellite missions.

6.2. Summary of main conclusions

6.2.1 Langjökull, Iceland

In chapter 3 I presented the first ice velocity map for LIC, Iceland. The velocity data, derived from ERS SAR interferometry, were acquired between the 22nd and 27th February 1994. I identified eight principal outlet glaciers with a maximum speed of 75 m yr^{-1}. Eight down-glacier velocity transects were extracted, along three of which I compared our InSAR estimates with sparse surface velocity measurements determined from a GPS survey undertaken over 170 days during Summer 2001. At six of the eleven locations included in both the GPS and InSAR datasets, ice velocity measurements were within the estimated error, indicating little change in ice velocity between February1994 and summer 2001. The largest difference between the InSAR and GPS velocity datasets occurred at Hagafellsjökull Vestri, where the 2001 GPS velocity estimate was 47 ± 10 m yr^{-1} faster than 1994 InSAR velocity estimate. This difference is attributed to locally high InSAR measurement error and the fact that in 2001, ice velocity was elevated following a surge. The close agreement between the GPS and InSAR datasets indicates that seasonal and inter-annual ice velocity variations at LIC are small. My data, in addition to other studies, suggest that Sudurjökull was experiencing a surge in 1994.

6.2.2. Flade Isblink ice cap, eastern North Greenland.

In chapter 4, I used InSAR techniques to produce a fine-resolution digital elevation model (DEM) of the FIIC in eastern North Greenland, and the first ever maps of the ice cap velocity. Each of the 2 summertime and 2 wintertime velocity maps represent 24-hours of motion and were acquired between 15th August 1995 and 3rd February 1996. I also estimated ice speed over the same period by applying feature tracking techniques to summertime and a wintertime pairs of SAR images separated by 35 days. My InSAR DEM is of 100 m horizontal resolution, agrees with independent surface elevation measurements to within 12 m and covers 91 % of the FIIC. Comparison with a widely-used DEM of this area (DiMarzio et al., 2007) highlighted elevation differences (RMS difference is 30 m) that we suggest arise from a combination of radar penetration in the percolation zone, detection of surface elevation changes and inherent errors in each of the elevation models. The InSAR DEM reveals ice surface geometry in finer detail than the previous best DEM, and provides information on the characteristics of the 8 major outlet glaciers, for example, that the marine-terminating glacier E is grounded. The InSAR DEM is used to delineate ice surface drainage basins, which range in area from 83 km^2 to more than 1000 km^2; tidewater glaciers have twice the area of land-terminating catchments on average. I mapped velocity of 90 % of the FIIC in winter 1996, 82 % in mid August 1995 and 60 % in late-August 1995. The radar look direction was favourable for surveying the velocity at all but 2 glaciers, and poor at 1. A greater variation in the position of peak velocity is observed for marine-terminating glaciers than for land-terminating glaciers. Peak velocity occurs at around 0.7 of the distance from the ice divide to the terminus for two thirds of the glaciers, at the terminus for one marine-terminating glacier and halfway between the ice divide and terminus for another. Peak velocity also occurs at lower elevations (~100 m) for marine-terminating glaciers than for land-terminating glaciers (~400 m). Summer velocities were observed to be more variable than winter velocities. We observe 45 ± 7 m yr^{-1} (~20 %) faster ice flow in winter 1996 than the mean flow observed previously between 1961 and 1978 (Higgins, 1991). There was no obvious correlation between glacier type and the seasonality of ice motion. Observed velocity variations were within 2σ above the measurement error at three of the smallest glaciers.

6.2.3. Western Greenland ice sheet

In chapter 5 I described how we used InSAR to produce an elevation model and 7 ice velocity maps for a 7 000 km^2 sector of the GrIS. My results from late-summer in 1995 show that ice velocity was enhanced far (100 km) inland from the ice margin by up to 360 % over the average winter rate. The degree of ice speedup is correlated with aspects of the ice sheet surface hydrology, including the area and quantity of runoff generated within surface hydrological catchments, and the distribution of supraglacial lakes. I conclude that the observed seasonal velocity fluctuations are controlled by surface melting and the delivery of this meltwater to the glacier bed. In contrast to a previous study (Joughin et al., 2008), our InSAR data shown that there is significant spatial variation in the incidence of late-summer ice speedup and that the effect extends to great distances inland from the margin. The areas of largest speedup are closely correlated with large scale melt-water channels on the ice sheet surface and we suppose that water is routed from the surface to the bed directly below these features.

While I show that ice flow speeds increase in early August (relative to winter) up too ~100 km from the margin, I am unable to discern for how long ice speeds are elevated, although my results show that ice speeds have returned to winter levels by the end of August. The pattern of speedup strongly suggests that the mechanism is closely linked to the penetration to the bed of surface meltwater near to the locations of supraglacial streams and lakes. The relationship between the volume of surface meltwater reaching the bed and the degree of ice speedup via enhanced basal sliding is complicated. For example, other studies (Sundal et al., in preparation) suggest that in years of high annual melt volume, annually averaged ice speeds are actually slightly lower than for years of low melt volume, presumably due to an efficient subglacial drainage system being developed more quickly in high melt years. While my results reveal the complex spatial pattern of late-summer speedup in a high melt year (1995), the data are too temporally sparse to infer changes in annual flow speeds due to changes in meltwater volume produced.

6.3. Synthesis

It is shown that:

- Spatial variations exist in the rates of ice motion at all three study areas;
- Larger glaciers flow faster than smaller glaciers;
- In general, the spatial distribution of flow is constant over time;
- On finer spatial scales, temporal fluctuations in speed do exist;
- Variations in the seasonality of flow exist on spatial scales of ~10 km;
- Variations in the seasonality of flow exist on timescales of ~10 days;
- Several localised areas of especially high seasonal flow variability exist.

Below I present the specific results in support of these findings and discuss their wider implications.

6.3.1. Spatial variations in rates of flow.

Winter velocity for each of the study areas is shown in Figure 6.1a. The LIC is drained by 8 land-terminating outlet glaciers which flow on average around 30 m yr^{-1} faster than the surrounding ice during winter. Each of the outlet glaciers is 2-3 km wide and around 10 km from the ice divide to the terminus. The FIIC (Figure 6.1b) covers nearly 10 times the area of the LIC and is drained by 5 marine-terminating and 3 land-terminating outlet glaciers. Winter flow speeds are typically around 100 m yr^{-1} faster at outlet glaciers than the surrounding ice. Typical widths and lengths of the FIIC outlet glaciers are 5 km and 30 km respectively. The western GrIS (Figure 6.1c) shows spatial variations of ~ 50 m yr^{-1} both as a function of latitude (i.e. perpendicular to the ice margin) and elevation.

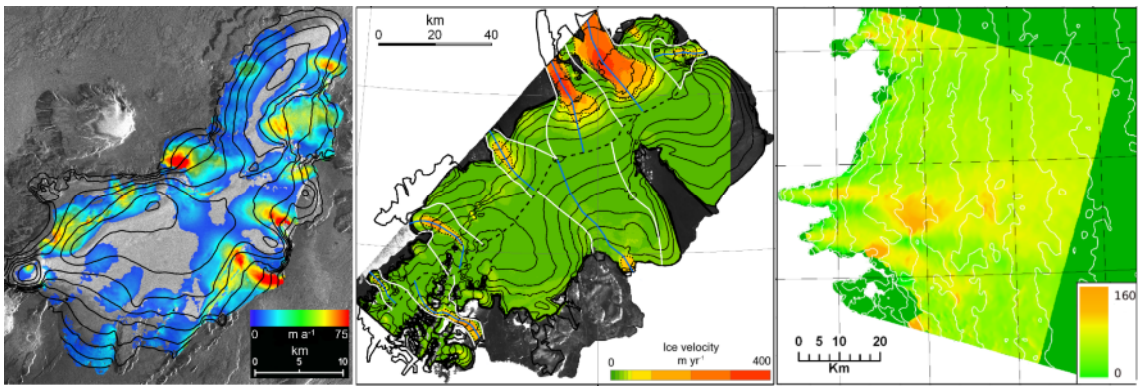

Figure 6.1. Wintertime velocity for the three study areas showing non-uniform ice flow.

This finding implies that similar processes of faster ice flow occur at the different study areas. Our results point to a topographic control on the locations of faster-flowing ice though in the absence of bed topographic information, this cannot be confirmed.

6.3.2. Larger glaciers flow faster than smaller glaciers.

At the LIC and the FIIC, larger glacier catchments are associated with faster ice flow, as shown in Figure 6.2. This can be explained by the larger mass of snow accumulating in the larger catchments and implies a topographic control on the positions of the outlet glaciers.

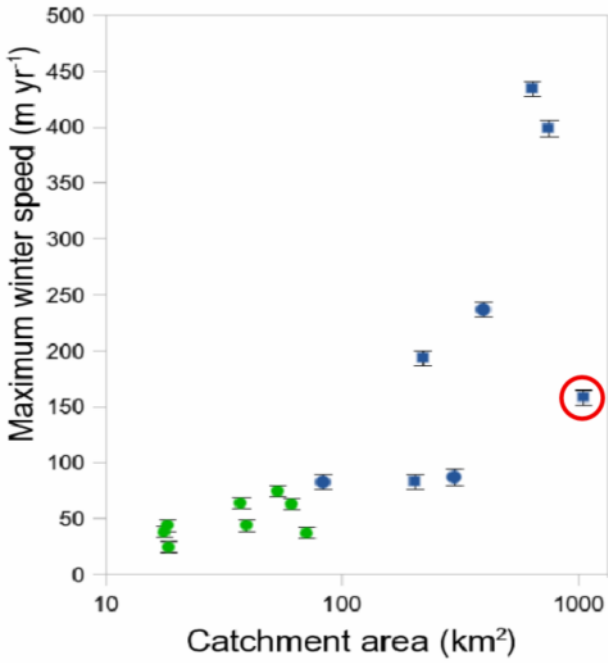

Figure 6.2. Plot showing the relationship between catchment area and winter speed for the LIC and the FIIC. Blue points show FIIC data (land-terminating as circles, marine-

terminating as squares), green shows LIC data. R^2 value for the correlation is 0.85 if erroneous catchment B data (within red circle) is excluded. (R^2 = 0.27 with B included). R^2 for both distributions (excluding point B) is 0.91.

6.3.3. Persistent large-scale distribution of flow

I observe close agreement between estimates of velocity from 1994 and 2001 at the LIC (Figure 3.4). At the FIIC and the western GrIS, the areas of fastest wintertime ice flow are the same areas of summertime ice flow (Figures 4.8 and 5.1). The general distribution of flow is the same for all datasets which implies that the same mechanisms of flow operate all-year round and from year to year.

6.3.4. Seasonal variations in speed at individual catchments.

My results show that there were significant seasonal variations in ice flow speeds between summer 1995 and winter 1996 in two widely separated areas of Greenland. At the FIIC, I observed that the flow speeds of 5 of the 8 outlet glaciers show significant differences between Winter and August. While larger catchments show larger maximum velocity increases between winter and August, correlation between catchment size and magnitude of speedup is weak (R^2 = 0.43). Marine-terminating glaciers at the LIIC show a wider range of seasonality than land-terminating glaciers (Figure 6.3). Only 1 land-terminating glacier showed seasonal variations in flow greater than 2σ above the error.

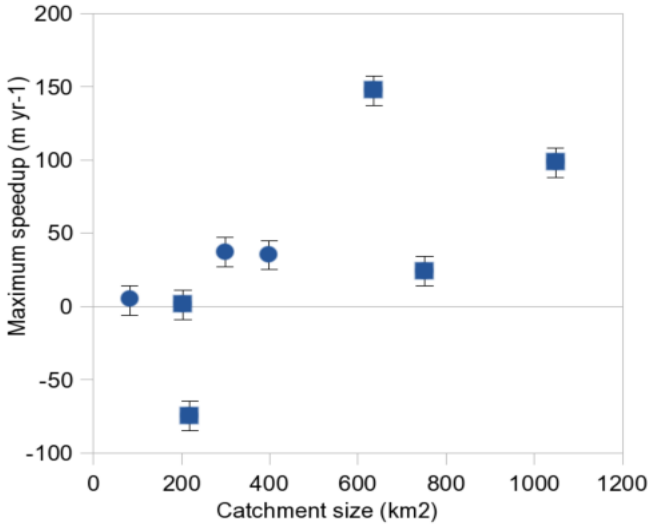

Figure 6.3. Maximum ice speedup for each glacier of the FIIC. Land-terminating

glaciers are shown as circles, marine-terminating glaciers as squares.

At the western GrIS, I observed summertime speedups of up to ~50 % above the mean winter rate. The relative size of speedup is strongly correlated ($R^2 = 0.76$) with the natural logarithm of surface catchment area showing that the catchments with larger surface area experience larger speedups (Figure 6.4.).

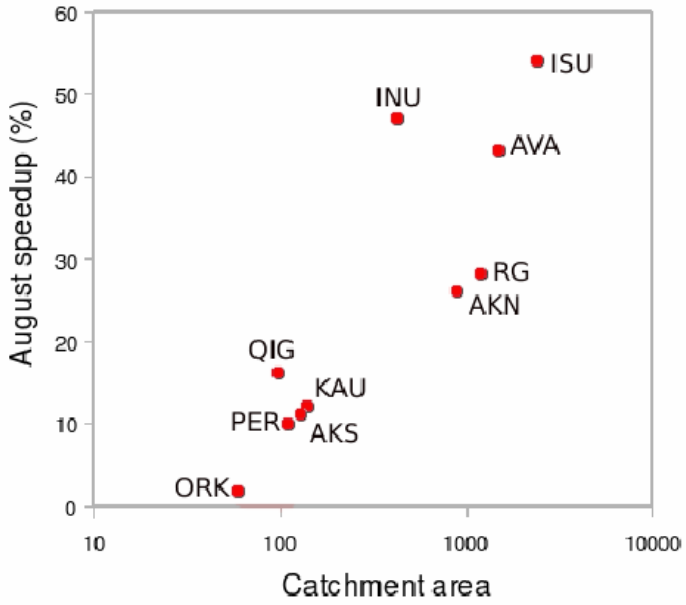

Figure 6.4. Correlation of catchment area with magnitude of August speedup at the western GrIS ($R^2 = 0.76$).

Drainage of surface water to the ice bed has previously been linked to velocity variations in other Arctic glaciers (Boon and Sharp, 2003; Bingham et al., 2005). My observations of fluctuations in ice velocity suggest that seasonal variations in meltwater availability play a role in modulating flow. The lack of significant seasonal variation in flow speeds of the smallest FIIC outlet glaciers and the smallest catchments of the western GrIS may be due to the fact that they have the smallest availability of meltwater to enhance sliding at the bed. My results support previous observations that the relationship between surface melt and ice velocity is not a simple one (Kamb, 1987; Truffer et al., 2005).

6.3.5. Spatial variations in seasonality of flow over ~10 km.

I observed different seasonal behaviour over distances of ~ 10 km at FIIC and the western GrIS as shown in Figure 6.5. It is clear that there is a high degree of spatial variability in the extent and amplitude of seasonal speedup when we compare wintertime velocity with late-summertime velocity. It is important to point out that these late-summertime observations represent behaviour on one day in August 1995, and may not represent flow at other (similar) times of year.

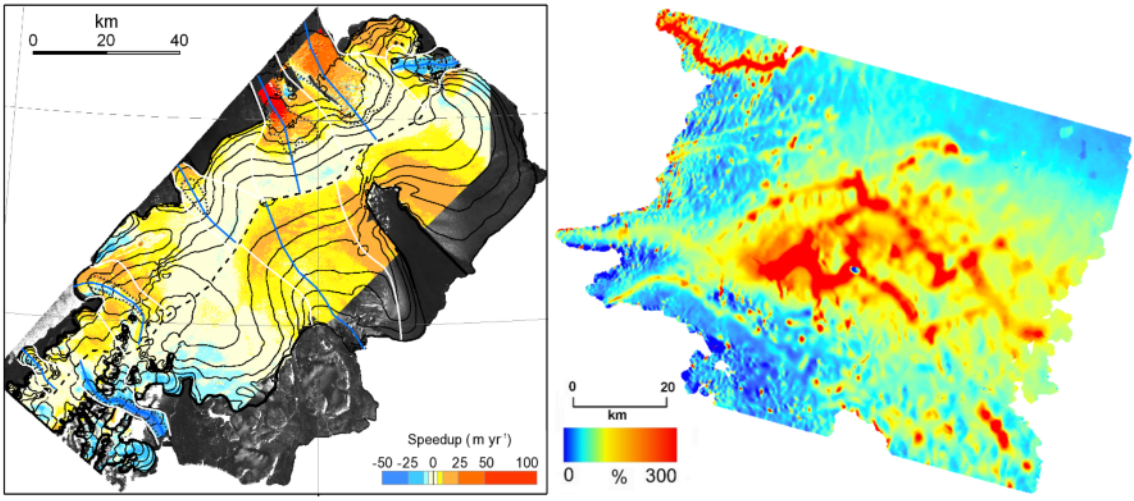

Figure 6.5. Maps of velocity difference between (left) winter and 24th August 1995 at the FIIC; and (right) between winter 1996 and 11th August 1995.

The highly non-uniform distribution of seasonal ice velocity variations indicates that a previously unseen complexity exists in the relationship between melting rates, drainage conditions and ice motion. My results at the western GrIS have implications for the 17-year record of annual ice motion measurements made by Van de Wal et al., (2008). The areas in which their measurements have been made may have been affected by progressive routing of subglacial water to adjacent areas, which would help to explain their observed negative trend in ice flow speeds. Because the magnitude of seasonal speedup shows large variations within relatively small areas, it is important to consider in detail the siting and interpretation of ground-based ice velocity measurements. In consequence, it may be premature to accept the claims of Van de Wal et al., (2008) that a warming climate will have limited implications for the evolution of the GrIS.

6.3.6. Temporal variations in seasonality of flow over ~10 days.

Figure 6.6. shows the variability in flow during late-Summer at the FIIC and the WGrIS. Maximum differences at the FIIC over 9 days in August were around ± 50 m yr^{-1} and were up to 300 m yr^{-1} over 19 days at the WGrIS.

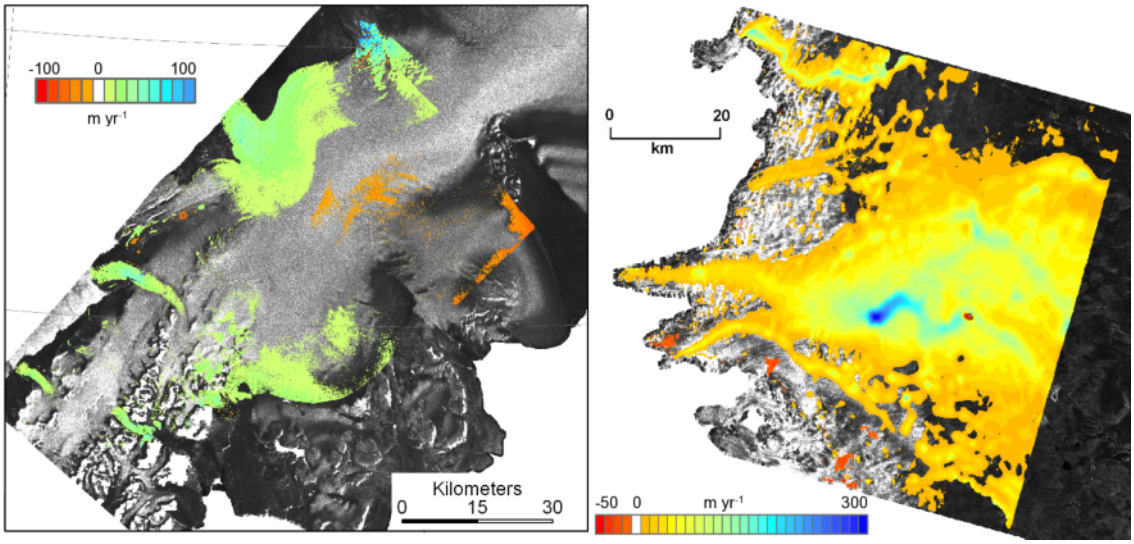

Figure 6.6. Differences in flow speeds above the estimated error (left) during the period 15th - 24th August 1995 at the FIIC; and (right) during the period 11th - 30th August 1995 at the western Greenland Ice Sheet, showing that ice flow in both areas slowed down in places during August. Differences within the estimated error are shown as transparent.

This finding implies that changes in meltwater production and flow respond to temperature changes on timescales of a few days and that closure of subglacial tunnels follows rapidly after a reduction in subglacial water flux. Smaller conduits will lead to less efficient drainage of meltwater produced thereafter, and may explain the large variability in late-summer ice flow speeds documented here and elsewhere (e.g. Joughin et al., 2008).

I would expect the drainage systems beneath faster flowing ice to be re-worked more quickly than those beneath slower flowing ice due to the high higher vertical velocity gradient at the ice sheet base. This suggests that in late-summer, when air temperatures and therefore the daily volume of melt produced at the ice surface is decreasing, subglacial tunnels excavated by the passage of surface meltwater reaching the bed will close more quickly than under slower flowing ice. An unusually warm day in late-summer, resulting in surface melting, will be more potent at increasing subglacial water

pressures for faster flowing ice than for slower flowing ice due to the re-worked and inefficient drainage system at the bed. I would expect this to lead to a higher degree of variability in ice flow speeds for faster outlet glaciers than for slower outlet glaciers. It may be that my results from early August capture just such a period of high variability and that the high velocities I observe are not representative of speeds at this, or any other time of year.

6.3.7. Localised seasonal flow features

Other features exhibiting large seasonal changes in velocity are observed at the western GrIS. My summertime 1995 velocity data show features which reveal details about the subglacial drainage of meltwater. Figure 6.7 shows one of these features - a 200 m wide 'filament' of apparently faster flow oriented roughly perpendicular to the margin and extending about 30 km inland from the margin. These features cross surface hydraulic catchments boundaries (Figure 5.3.) which implies they are controlled subglacially, as opposed to supraglacially. My velocity data indicate that ice at these locations flow more rapidly in early August than in winter by ~100 m yr^{-1} and ~100 m yr^{-1} faster than the surrounding areas. It is possible that these features represent the locations of subglacial conduits draining meltwater to the margin of the GrIS. This is supported by field observations (Bartholomew, personal communication; Mernhild and Hasholt, 2009), which indicate that the location at which one the features intersects with the ice margin corresponds to the location at which a subglacial drainage tunnel emerges from the ice sheet (Figure 6.8). If these subglacial conduits contain pressurised water, they will presumably decouple the ice from the bed and result in enhanced sliding as has been observed elsewhere (e.g. Boon and Sharp, 2003; Zwally et al., 2002).

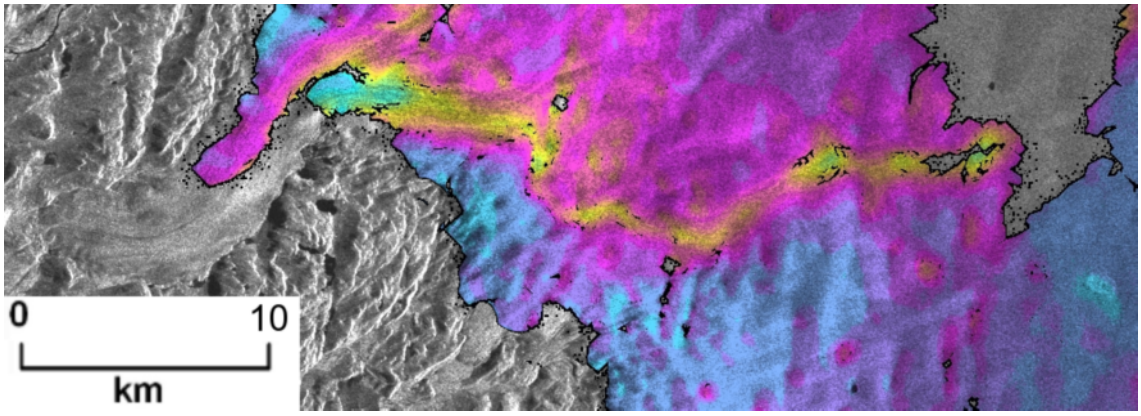

Figure 6.7. One of the two faster-flow features observed at the western GrIS in August 1995.

Figure 6.8. Subglacial drainage tunnel emergent at the western margin of the GrIS. Photograph by Ian Bartholomew.

6.4. Wider implications

6.4.1. Inter-annual speedup at the FIIC

The infrequent sampling of my data makes it difficult to make confident statements about inter-annual velocity variations. However, my results at the FIIC suggest that the second fastest flowing outlet glacier, which drains 9 % of the FIIC, has accelerated by at least 20 % between 1978 and 1996, though this could be an artifact of the differing observation periods. Surges have been observed at many Arctic glaciers and it is possible that our 1996 observations of elevated ice speed are due to just such a surge. This hypothesis could be tested by examining other datasets and is discussed in section 6.5.2. An alternative explanation for the speedup from 1978 to 1996 we observe for

catchment D could be that accumulation-driven changes in the geometry of the ice cap since 1992 have altered the magnitude of the gravitational driving stresses at the ice cap. Burgess et al., (2009) modeled the annual accumulation across Greenland for the period 1958-2007 and estimated that the accumulation rate anomaly was largest for the period 1992-2007 (the period of our InSAR measurements) and smallest for the period 1965-1971 (the period partially spanning the observations of Higgins (1991)). Further evidence of an increase in accumulation is provided by observations of thickening of the FIIC over the last decade (Pritchard et al., 2009; Krabill et al., 2000). If this speedup was due to a regional increase in accumulation causing geometric changes to the ice cap, we would expect to observe it at more than one outlet glacier. Revisiting the aerial photos used by Higgins (1991) may yield velocity estimates for other glaciers draining the FIIC, which could be used to support or refute this hypothesis. The observed speedup and pattern of elevation change may be explained by the observed negative trend in the extent (Meier et al., 2007) and thickness (Farrell et al., 2009) in Arctic sea-ice, which reduces ice-buttressing of the glacier tongue while providing additional potential for evaporation of seawater and subsequent snowfall at higher elevations. Reduced sea ice in summer may also be a factor in the faster summertime flow speeds observed in marine-terminating catchments B and E.

6.4.2. Seasonal melt-induced flow variations

Previous studies have revealed a relationship exists between surface melting of the GrIS and ice dynamics. Microwave backscatter observations have shown that the total melted area in Greenland has increased by ~16 % between 1979 and 2002, with widespread melting above 2000 m elevation in 2002 and 2005 (Steffen et al., 2004; Hanna et al., 2005). Recent ICESat observations have shown thinning extending further north and to higher elevations (Pritchard et al., 2009). Zwally et al. (2002) proposed a mechanism which provides a causal link between melting and thinning and which has since been supported by *in situ* observations (Das et al., 2008) and modelling studies (Parizek and Alley, 2004; Van der Veen 2007). Previous observations of melt-induced changes in ice motion have been confined to marginal areas (e.g. Joughin et al., 2008) or to sparse point measurements (e.g. Van de Wal et al., 2008) due to limitations in the data coverage from other techniques. Joughin et al. (2008), found that the seasonal summer ice

acceleration at the western GrIS was spatially consistent when averaged over 24 days and suggests that dynamic thinning caused by ice acceleration is likely to be uniform. The authors estimate the magnitude of summertime speedup to be 50 % above the winter rate.

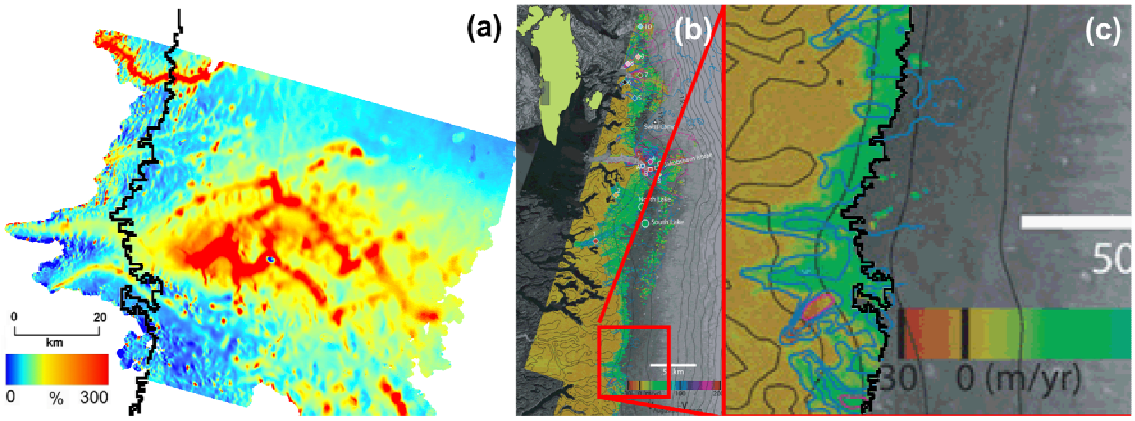

Figure 6.9. Comparison between Greenland August speedup presented in Chapter 5 (a) and Joughin et al., (2008) (b,c) from speckle tracking. The extent of data in (b,c) is highlighted with a black line, which is also shown in (a) for comparison. As InSAR offers superior accuracy (1 m yr^{-1} versus 20 m yr^{-1}), coverage (~100 km inland versus ~ 10 km inland) and time resolution (1 day versus 24-days) compared to speckle tracking, widespread and non-uniform variations in flow are resolved in (a) that are not apparent in (b,c).

In contrast to previous studies, my results cover a large area (7 000 km^2), reach higher elevations (1 600 m) and area of a finer spatial (100 m) and temporal (1 day) resolution. My observations imply that water melted from the ice sheet surface is reaching the ice sheet bed at many locations and promotes a seasonal enhancement of ice flow at elevations up to 1 600 m.a.s.l.; higher and farther inland than was previously considered (e.g. Joughin et al., 2008). The melted area of Greenland during the year of our summertime data (1995) was just above the annual average for the period 1979 - 2005 and I assume that similar patterns and magnitude of speedups occur in years with similar amounts of melting. My findings suggest that increased intensity of melting will affect ice dynamics and also that higher variability in the amount of melting will cause the drainage system to adjust between episodes of water input to the bed, resulting in a higher variability in rates of ice flow. Although a large supply of water is required for

surface water to reach through 1000 m of cold ice via the hydro-fracture mechanisms (Van der Veen, 2007), such a supply is available during summer in the from of supraglacial lakes, which have previously been observed (Das et al., 2008) to drain to the bed. Due to decreasing surface gradient with elevation, modest atmospheric warming is required for the melted area to be extended to higher elevations as observed by Steffen et al., (2004). At higher elevations, the ice sheet has a lower surface gradient and the potential exists for more - and larger - lakes to form (Sundal et al., 2009). Future warming could result in more lakes forming, or cause more of the lakes that currently form, to drain.

There has been much discussion of the relative importance of melt-induced and ice-buttressing on ice dynamics. It is clear that as ice continues to retreat, there will be fewer marine-terminating sectors. My findings support the notion that further increase in melted area will be accompanied by more widespread delivery of surface water - and heat - to the bed, which could thaw ice frozen to the bed, allowing faster flow through enhanced basal sliding or through sub-glacial sediment deformation. This mechanism is presumably applicable to regions of both land and marine-terminating ice. Sole et al., (2008) suggest that marine-terminating outlet glaciers may be inherently more sensitive to changes in basal water pressure than land terminating outlet glaciers since their termini are often already at or near the flotation point. The authors argue that an identical increase in surface meltwater input to the bed would be more likely to raise subglacial water pressure to values approaching overburden pressure across other areas of the bed at a marine-terminating terminus, with correspondingly larger ice acceleration and dynamic thinning. If this were the case, a forcing from surface melting may reduce significantly once the GrIS retreats beyond the ocean (Sole et al., 2008).

6.5. Limitations

While my results show that InSAR observations can be used to gain an understanding of the physical processes controlling ice dynamics, a consideration of errors is desirable as it helps us apply a level of confidence to our findings and highlights any limitations in data quality. In Section 6.5.3 I estimate errors for the FIIC and the western GrIS, which I intend to apply as a correction to chapters 4 and 5.

6.5.1. Insufficient temporal sampling

A major limitation of this work is the poor temporal sampling of data. While the fine resolution of the InSAR data shows complexity hitherto unseen, it is not available at sufficiently regular intervals or over a sufficiently long period for us to develop correlations between climate variables and fluctuations in ice motion. Future missions (discussed in section 6.6.2) may provide the long-term and regular observations required.

6.5.2. Invalid surface parallel flow assumption

With the single look-direction data used in Chapters 4 and 5, it is necessary to assume that ice flows parallel to the surface and in the direction of steepest slope averaged using a length-scale ~10 times the local ice thickness (Paterson, 1994). With dual-look data as used in chapter 3, there is no need to prescribe the azimuth of the ice flow vector but the assumption of surface parallel flow is still required. In reality, ice rarely flows exactly parallel to the surface and flow vectors can be inclined steeply with respect to the ice surface, especially in areas of high accumulation or ablation (Paterson, 1994).

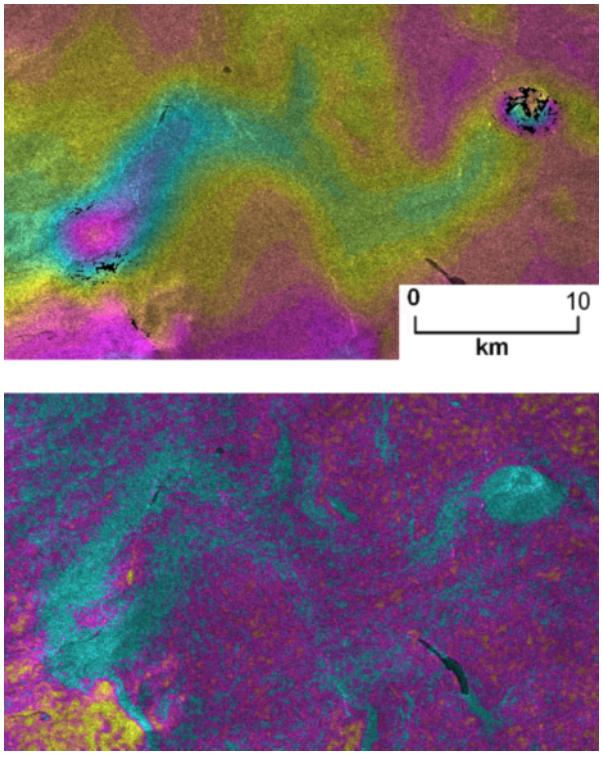

Figure 6.10. 'Dipole' feature observed at the western GrIS. (Top) August displacement map and (Bottom) Interferometric coherence scaled from low (0.1) in blue to high (0.5) in yellow. Coherence in a measure of surface change – lower coherence occurs due to higher surface change within the data acquisition interval.

A limitation of this work is the ambiguity that exists in the derived ice motion field in areas where the assumption of surface parallel flow is invalid. An example of this is the 'dipole' velocity anomaly observed at the western GrIS (Fig. 6.10) which consists of an area of apparent speedup 40 km from the margin of ~200 m yr^{-1} greater than the surrounding area and an area of apparent slowdown 18 km further inland of 200 m yr^{-1} less than the surrounding area. I have previously assumed that ice flow is directed parallel to the surface but it seems likely that there is a vertical component of motion in many locations. While the near-zero spatial baseline associated with the interferogram precludes the possibility that this feature represents topographic change between winter and summer, the steep ERS radar LOS (24º to the vertical) means that the interferogram has roughly 2.5 times higher sensitivity to vertical motion over the SAR image pair acquisition interval (1 day) as compared with horizontal motion. We calculate that ~50 cm of vertical motion over the 24-hour SAR acquisition interval could cause the apparent horizontal velocity changes. The low coherence observed at the feature (Figure 6.10) support the idea that these areas have undergone change such as fracturing during the data acquisition interval. The early August data was acquired following an unseasonably warm period which peaked around day-215 (Figure 5.4) and it is possible that this feature structures represents 'slumping' of a subglacial void following a reduction in surface melting and therefore subglacial water flux.

Similar features showing vertical motion have been observed in East Antarctica (Wingham and Shepherd, 2005; Fricker et al., 2007) and indicate the movement of water between subglacial lakes. In these previous studies, however, the 'upstream' site lowers and the 'downstream' rises, as water moves along a path of decreasing hydro-potential. Assuming the hydo-potential decreases from inland regions to the ice margin, I observe what appears to be the opposite behaviour; the site closer to the margin lowered at the same time as the inland site rose. A possible explanation is that the topography of the bed in this area is such that the basal hydo-potential gradient is

oriented directly away from the margin towards the interior of the GrIS. If this were the case, my observations would be consistent with the movement of water along a subglacial hydraulic pathway as observed by Wingham and Shepherd (2005).

Another possible explanation requires the drainage of a surface lake at the inland site immediately prior to the acquisition of the SAR data. In this case, the upwards movement of the inland site could be due to the delivery of a large amount of water to the ice bed following the rapid drainage of a surface lake, as has been observed by Das et al., (2008). This is supported by the SAR backscatter amplitude and coherence images (Figure 6.4.) which clearly show that a lake existed at the inland location and that the surface underwent change during the data acquisition interval. The two areas coincide with the location of the same supraglacial stream apparent from the SAR backscatter amplitude image and which is predicted by the surface hydrology model (Figure 5.2.). I assume that the location of this surface stream is determined by surface expressions of the underlying topography such that the surface depression is correlated with a 'low' in topography of the bed. If this is true then the two sites should also be linked by a subglacial hydraulic pathway and water at the inland site will flow towards the site close to the margin. In this case, we might also expect the surface motion at the downstream location to be directed upwards, not downwards as we observe. If the downstream location coincided with the location of a subglacial lake which was nearly full at the time of the upstream supraglacial lake drainage, it is possible that the delivery of additional water caused the subglacial lake to breach its dam and drain catastrophically. We would then observe the downwards motion of the surface following evacuation of the lake.

The discussion above shows that these localised features represent ambiguity in the data and there is more than one way to explain the observations. A satellite capable of acquiring data from 3 different look directions is required to remove the need for the surface parallel flow assumption.

6.5.3. Inaccuracies in velocity estimates

Errors in our velocity estimates limit our ability to detect small changes in flow with

confidence. I estimated error for the FIIC and western GrIS by analysing the distribution of displacement values calculated for ice-free areas, and weighting this error by the relative alignment of the radar look and local ice flow directions. Figure 6.11 shows histograms of displacement values for ice free areas and the RMS value of the line of sight (LOS) error for the FIIC (6.8 m/y) and the western GrIS (1.4 m/year). The difference in these values is due to the fact that unlike for the western GrIS, I was unable to remove the phase ramp due to errors in the interferometric baseline estimate for the FIIC data as an accurate external dataset of height values for ice free areas was unavailable.

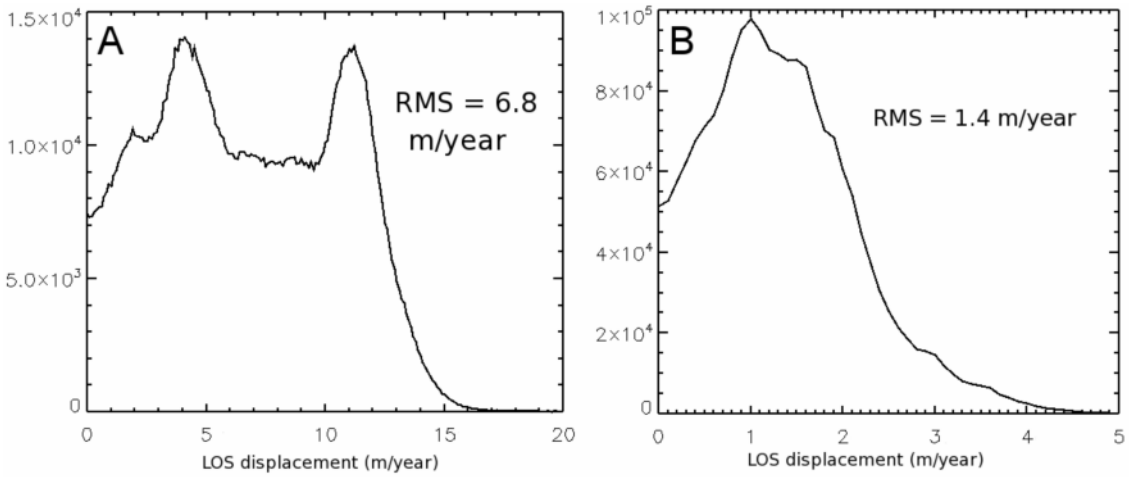

Figure 6.11. Distribution of calculated displacement values for (A) the FIIC and (B) the western GrIS. The root mean square (RMS) value of each distribution is also shown.

In order to weight the error as a function of the suitability of the radar look direction for observing displacement, I divided the LOS error by the cosine of the difference between the radar LOS and the local ice flow vector so that the error increases dramatically as the radar LOS is close to being orthogonal to the local ice flow direction. Error maps for the western GrIS and the FIIC are shown in Figure 6.12.

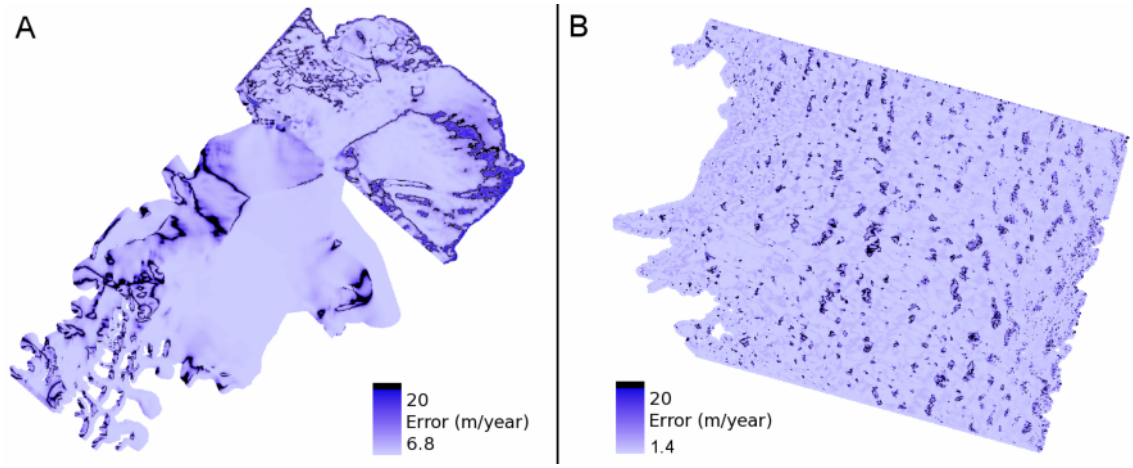

Figure 6.12. Error maps for (A) the FIIC and (B) the western GrIS. The error at the level of the calculated LOS error where the radar look direction is favourably oriented relative to the local ice flow direction, but increases where the angle between the two vectors approaches 90 degrees.

6.6. Future research

InSAR is suitable for testing other glaciological hypotheses such as the the cause of speedup of tidewater glaciers in Greenland, the onset of ice streaming in Antarctica, subglacial transport of water, and the cause of the break-up of ice shelves surrounding the Antarctic Peninsula. However, further development is required before the full potential of InSAR is realised (Massom and Lubin, 2006). There is a clear need for long-term acquisition of SAR data from satellites with a short-revisit time in order to minimise the loss of interferometric coherence. Here I summarise emerging techniques and future satellite missions, before outlining potential directions for further work at each of the three study areas.

6.6.1. Emerging techniques

There are currently several satellites in operation equipped with SAR instruments, including Europes's Environmental Satellite (Envisat), Japan's Advance Land Observation Satellite (ALOS) and Canada's Radarsat-2. However, the respective repeat periods of 35-days, 46-days and 24-day mean that all suffer from loss of coherence due to temporal decorrelation when applied to InSAR studies of ice motion. While the SARs on-board Envisat and Radarsat both operate at around 5.6 cm, ALOS Phased Array type

L-band Synthetic Aperture Radar (PALSAR) operates at 24 cm. Longer radar wavelengths offer superior temporal coherence on snow and ice due to their deeper penetration (Dall et al., 2001). In spite of this, the 46-day repeat interval is still to large to maintain the level of interferometric coherence required for conventional InSAR. However, Rignot, (2008) recently demonstrated the use of 'speckle tracking' techniques (tracking of coherent noise within the SAR images) with PALSAR data in order to map ice velocity in West Antarctica. Rignot (2007) has also demonstrated cross-platform interferometry using a combination of ERS-2 and Envisat ASAR data at a site where data acquired during the ERS-Tandem mission was unable to produce useful results (Rignot, 2007). Using an interferometric baseline of ~2km and a temporal baseline of 30 minutes, Ringot (2007) produced an interferogram of Jakobshavn Isbræ, western GrIS. The data was acquired after the end of the summer melt-season and while interferometric coherence is lost on snow and firn, it is is maintained over ice. For this temporal baseline, 1 fringe represents 1 km $year^{-1}$ flow at C-band (5.6 cm) so this method is only suitable for the fastest flowing outlet glaciers. Due to the large interferometric baseline, 5-6 m of elevation change results in 1 fringe of topographic phase necessitating topographic correction accurate to ~ 1 m in order to isolate the velocity signal. This technique may provide insights into glacier flow variability on sub-hour time scale such as stick-slip motion, sliding, calving (Rignot, 2007), though the requirement of precise topographic knowledge and the stringent temporal and interferometric baseline requirements restricts the use of this technique to a handful of SAR scenes.

It appears that new satellite data with which to apply InSAR will not be acquired for at least 2 years. In the meantime, novel techniques are being developed to yield novel results from data already archived. One such technique is Multiple-Aperture InSAR (MAI) which uses split-beam InSAR processing to extract components of the displacement in the along-track direction as well as along the line of sight (Bechor and Zebker, 2006). The first application of this technique to the cryosphere uses the same SAR data as used in Chapter 3 of this thesis and has yielded additional velocity measurements (Gourmelen et al., submitted).

Another new technique is ground-based interferometry (Mecatti et al., 2007). In a recent

study, a ground-based SAR interferometer was deployed on Belvedere glacier, Italy. During 2007, the sensor was used to form a deformation map of the glacier surface about every 30 minutes almost continuously for one month. Although affected by local weather conditions, the radar sensor was able to measure motion of up to 10 cm per day (Noferini et al., 2007). A DEM of the illuminated part of the glacier was generated and compared with an available topographic map from July 2005. Large differences in the ice surface height were apparent from the comparison and the reduction in ice mass was quantified (Noferini et al., 2007). The study demonstrated the potential of ground-based interferometry for studying short-term changes over smaller glaciers which may be unsuitable for monitoring using satellite data due to its coarser spatial resolution.

6.6.2. Future satellite missions

While this thesis shows that there are still novel findings being made from archived ERS-Tandem data, forthcoming satellite missions will provide new datasets for glaciological research. Future missions should be designed with the capability of maintaining the interferometric baseline in a specified range to supply larger and more consistent datasets and enable efficient application of the data. Here we outline selected future missions.

6.6.2.1. TerraSAR-X and TanDEM-X

The German TerraSAR-X satellite was launched in June 2007 into an 11-day repeat orbit and is designed to acquire high-resolution (1-5 m) SAR data (Adam et al., 2007). Despite the relatively short repeat-period, the short radar wavelength (3 cm) means that temporal decorrelation of interferometry data is still a problem for dynamic areas of snow and ice. Due for imminent launch is the TanDEM-X satellite, which will join the nearly identical TerraSAR-X satellite in a 'HELIX' orbit (Figure 6.13.) for at least 3 years of joint operation (Krieger et al., 2007). Although the primary objective of the TanDEM-X mission is to form accurate (less than 10 m vertical), 12 m horizontal resolution DEMs, along-track interferometry can be performed by adjusting the along-track distance between satellites from zero to several kilometres. While it is not yet clear what the maximum along-track and therefore temporal separation will be, Moreira et al. (2004) state that that the mission is required to measure sea-ice drift around 0.01 m s^{-1}.

This corresponds to an ice flow velocity of ~300 km yr^{-1} so, although unsuitable for many ice flow applications, there may be potential for monitoring short-duration speedups such as stick-slip motion or glacier surges.

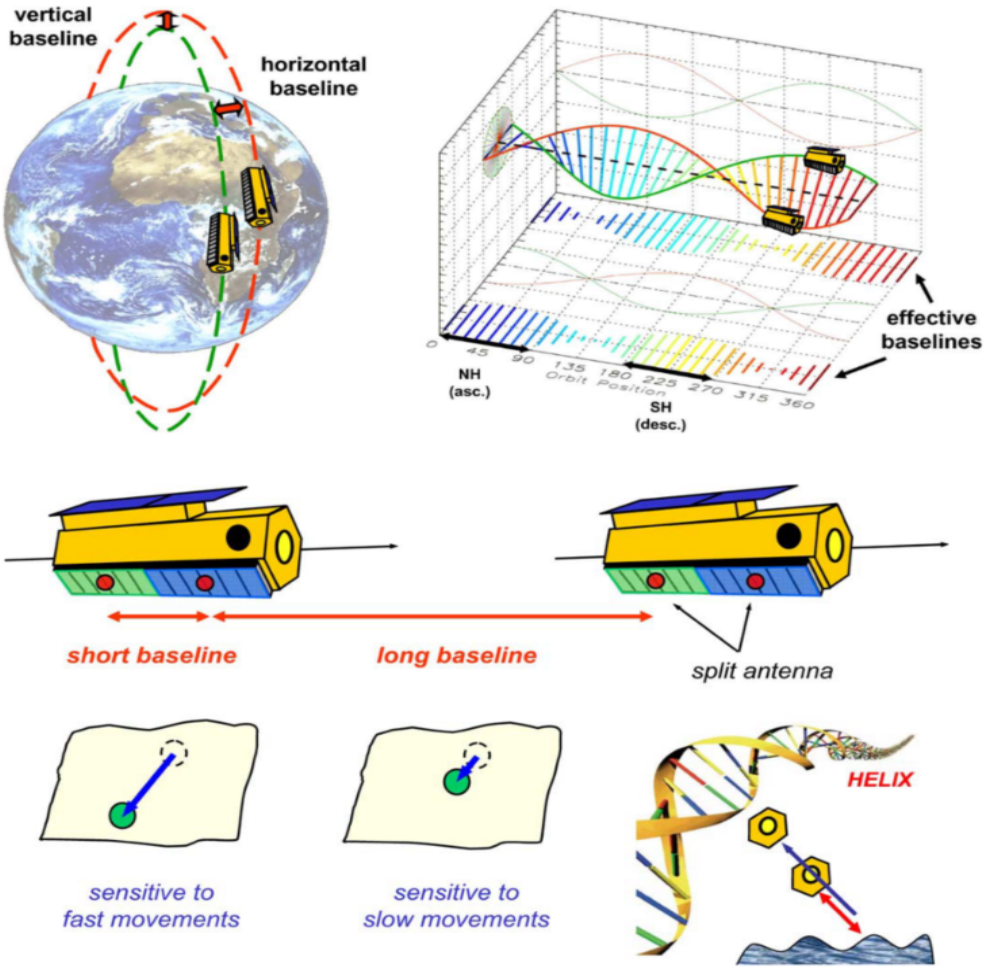

Figure 6.13. TanDEM-X orbital configuration (top) and along track interferometry (bottom).

6.6.2.2. Sentinel-1

As part of the Global Monitoring for the Environment and Society programme, ESA is undertaking the development of a European Radar Observatory known as Sentinel-1. This polar-orbiting satellite system consists of a constellation of two satellites equipped with C-band SARs and represents the current best hope for future InSAR studies of the cryosphere. Due for a 2012 launch, the two satellites have a nominal 12-day repeat orbit, though a 6-day repeat phase is available. In addition, the interferometric Wide Swath Mode with 250 km swath, 5 by 20 metre spatial resolution will have a revisit time of 1-

day over the polar regions (Attema et al., 2007) which will yield 6-day interferograms separated by 1-day. This system should be capable of providing similar quality data to the ERS-Tandem mission with the advantage of making instantaneous observations over areas roughly six times larger than ERS.

6.6.3. Future work at the Langjökull ice cap

My results contain larger errors in areas where only single-look SAR data were available and the radar LOS was almost orthogonal to the ice flow direction. Recently, the technique of Multiple Aperture InSAR (MAI) has been used with the same initial SAR data to measure velocity in the azimuth as well as the range directions (Gourmelen et al., submitted), and has yielded improved velocity estimates.

Ice thickness data for the LIC was acquired by Björnsson et al., (2006) from a ground-based radar survey. InSAR velocity estimates and these ice thickness measurements could be used to calculate the mass balance of the ice cap. This could be compared with *in situ* measurements of mass balance from ablation stakes and GPS. A term in the mass budget that is difficult to measure from the surface is the rate of basal melting due to high geothermal heat flux in this area. This could be measured with a phase-sensitive ice-penetrating radar.

6.6.4. Future work at the Flade Isblink ice cap

It should be possible to confirm whether or not the inter-annual speedup I observed at glacier D between 1978 and 1996 is a surge by examining time series' of ice elevation data from altimetry to look for changes in geometry and by using more recent InSAR data to detect any changes in ice flow speed since 1996. Work is already proceeding to study elevation changes over the ice cap using ERS Radar Altimeter and ICESat data (Rinne et al., in preparation). The position of the terminus of glacier D could be tracked over time to see if the speedup was contemporaneous with a retreat of the terminus. This may reveal a contribution to changing ice dynamics from reduced ice-buttressing (e.g. Joughin et al., 2005). The basal topography of the FIIC is unknown, resulting in large errors in estimates of ice volume. Knowledge of the ice thickness across the ice cap

could be acquired by an ice penetrating radar survey. This would allow the potential contribution of the ice cap to sea level rise to be calculated as well as the mass balance to be estimated via the mass budget method. Station Nord is in a prime location as a base for an ice-penetrating radar survey of the fastest flowing outlet glaciers which are situated within 25 km of the station. This work would be best undertaken before the start of the melt season in May, as surface water prevents complete transmission of radar energy to the ice bed.

6.6.5. Future work at the western Greenland ice sheet.

It would be interesting to know if supraglacial lakes and streams form in the same locations each year or if they are advected towards the margin with the motion of the ice, as this should help to reveal the controls on lake location. In chapter 5 I presented predictions of lake locations based on surface drainage modelling using our InSAR-derived DEM from 1996. Sundal et al., (2009) present a method for observing supraglacial lakes from NASA's Moderate-Resolution Imaging Spectroradiometer data. Comparison of the locations of modelled and observed lakes is planned (Palmer and Sundal, in preparation).

Within the NASA Program for Regional Climate Assessment (PARCA), surface-based measurements of ice motion at 30-km intervals approximately along the 2000-meter contour completely around the ice sheet have been made since 1995. However, these measurements are made only yearly to provide a annual mean motion at each location and are unable to capture variations in motion on shorter timescales. Deployment of continuously measuring GPS units at elevations up to 2000 m and above would provide data to validate the complexity in ice motion revealed by our InSAR results.

Because variations in ice flow affect the mass balance of ice sheets in numerous ways, our data show that an improved understanding of the evolution of the GrIS over the coming century requires that simulations of the ice sheet response to expected climate warming include an appreciation of the coupling between surface and basal hydrology. *In situ* temperature, hydrology, GPS and ice thickness measurements combined with contemporaneous feature tracking and laser altimetry from satellites would provide a

more complete picture of the relationship between melting, conditions at the bed and ice motion. These ‘combined’ studies are vital in driving forward our understanding of how expected warming is likely to affect ice dynamics over the next century.

6.7. Concluding remarks

I have shown that by making precise near-instantaneous measurements ice motion, InSAR can be used to investigate ice dynamics and with additional data, the processes controlling motion. Even the limited datasets presented here reveal great complexity and demonstrate the challenges facing glaciology if we are to improve estimates of the land-ice contribution to sea level rise in a warming world. I have shown that different glaciers and locations at the FIIC and the western GrIS show variations in the seasonality of ice flow over distances of ~10 km and tim-scales of ~10 days. My data is of insufficient sampling frequency and spans an insufficient length of time for us to derive a general rule for predicting the behaviour of glaciers as a function of their characteristics. I suggest that analysis of seasonal and inter-annual ice velocity variations at individual ice masses and their outlet glaciers is required to reduce the error on estimates of the response of Arctic land-ice to expected warming.

References

Abdalati, W. and K. Steffen (2001), Greenland ice sheet melt extent: 1979-1999, *Journal of Geophysical Research, 106*(D24), 33,983-33,989.

Abdalati, W., W. Krabill, E. Frederick, S. Manizade, C. Martin, J. Sonntag, R. Swift, R. Thomas, W. Wright and J. Yungel (2001), Outlet glacier margin elevation changes: Near-coastal thinning of the Greenland ice sheet, Journal of Geophysical Research – Atmospheres, 106(D24), 33729-33741.

Adam, N., M. Eineder, H. Breit, and S. Suchandt (1999). Quality of the D-PAF ERS orbits before and after the inclusion of PRARE data. 2nd International Workshop on ERS SAR Interferometry, "FRINGE99", Liege, Belgium, November 10-12.

Alley, R. B., J. Marotzke, W. D. Nordhaus, J. T. Overpeck, D. M. Peteet, R. A. Pielke Jr., R. T. Pierrehuumbert, P. B. Rhines, T. F. Stocker, L. D. Talley and J. M. Wallace (2003), Abrupt Climate Change, *Science, 299*, 2005-2010.

Alley, R. B., T. K. Dupont, B. R. Parizek, and S. Anandakrishnan (2005), Access of surface meltwater to beds of sub-freezing glaciers: preliminary insights, *The Annals of Glaciology, 40*, 8–14.

Amelung, F., D. L. Galloway, J. W. Bell, H. A. Zebker, and R. J. Laczniak (1999), Sensing the ups and downs of Las Vegas: InSAR reveals structural control of land subsidence and aquifer-system deformation, *Geology, 27*(6), 483-486.

Anandakrishnan, S., D. D. Blankenship, R. B. Alley (1998), Influence of subglacial geology on the position of a West Antarctic ice stream from seismic observations, *Nature, 394*, 62-65.

Attema et al., (2007), Sentinel-1 – The radar mission for GMES land and sea services, *ESA Bulletin, 131*, 10-17.

Bahr, D. B., M. Dyurgerov and M. F. Meier, (2009), Sea-level rise from glaciers and ice caps: A lower bound, *Geophysical Research Letters, 36*, L03501, doi:10.1029/2008GL036309

Bamler, R. and P. Hartl (1998). Synthetic aperture radar interferometry. *Inverse Problems, 14*, R1-R54.

Bechor, N. B. D. and H. A. Zebker (2006), Measuring two-dimensional movements using a single InSAR pair, *Geophysical Research Letters, 33*, L16311, doi:10.1029/2006GL026883

Bell, R. E., D. D. Blankenship, C. A. Finn, D. L. Morse, T. A. Scambos, J. M. Brozena and S. M. Hodge (1998), Influence of subglacial geology on the onset of a West Antarctic ice stream from aerogeophysical observations, *Nature, 394*, 58-62.

Bindschadler R. A., M. A King, R. B. Alley, S. Anandakrishnan, L. Padman (2003) Tidally controlled stick-slip discharge of a West Antarctic ice stream, *Science, 301*(5636), 1087-1089.

Bindschadler, R. (1998). Monitoring ice sheet behavior from space. *Reviews of Geophysics, 36*(1), 79-104.

Bindschadler, R., P. Vornberger (1998), Changes in the West Antarctic ice sheet since 1963 from declassified satellite photography, *Science 279*(5351), 689-692.

Bingham, R. G., P. W. Nienow, M. J. Sharp and S. Boon (2005), Subglacial drainage processes at a High Arctic polythermal valley glacier, *Journal of Glaciology, 51*(172), 15-24.

Bingham, R. G., P. W. Nienow, M. J. Sharp, (2003), Intra-annual and intra-seasonal flow dynamics of a High Arctic polythermal valley glacier, *Annals of Glaciology, 37*, 181-188.

Björnsson H, F. Pálsson, O. Sigurdsson, G. E. Flowers (2003), Surges of glaciers in Iceland. *Annals of Glaciology, 36,* 82-90.

Björnsson H., S. Guðmundsson, T. Jóhannesson, F. Pálsson, G. Aðalgeirsdóttir and H. H. Haraldsson. (2006), Geometry, mass balance and climate change response of Langjökull ice cap, Iceland, *The International Arctic Science Committee (IASC), Working Group on Artic Glaciology*, Obergurgl, Austria, Jan. 30 – Feb. 3, 2006.

Björnsson, H. (1979), Glaciers in Iceland. *Jökull, 29,* 74-80.

Björnsson, H., and F. Pálsson. (2008), Icelandic glaciers. *Jökull, 58*, 365-386.

Björnsson, H., F. Pálsson and H. H. Haraldsson. (2002) Mass balance of Vatnajökull (1991-2001) and Langjökull (1996 -2001), Iceland. *Jökull, 51*, 75-78.

Björnsson, H., F. Pálsson, O. Sigurðsson and G. E. Flowers. (2003), Climate change response of Vatnajökull, Hofsjökull and Langjökull ice caps, Iceland. *Annals of Glaciology, 36,* 82-90.

Boon, S and M. Sharp (2003), The role of hydrologically-driven ice fracture in drainage system evolution on an Arctic glacier, *Geophysical Research Letters, 30*(18), 1916. doi:10.1029/2003GL018034.

Box, J. E., D. H. Bromwich, B. A. Veenhuis, L. S. Bai, J. C. Stroeve, J. C. Rogers, K. Steffen, T. Haran, S. H. Wang, (2006), Greenland Ice Sheet Surface Mass Balance Variability (1988-2004) from Calibrated Polar MM5 Output. *Journal of Climate 19,* 2783-2800.

Box J. E., and K. Ski (2007), Remote sounding of Greenland supraglacial melt lakes: implications for subglacial hydraulics, Journal of Glaciology, 53(181), 257-265.

Brenner, A. et al. (2003), Derivation of range and range distributions from laser pulse waveform analysis for surface elevations, roughness, slope, and vegetations heights, Algorithm Theoretical Basis Document (ATBD) v.4.1, available at http://www.csr.utexas.edu/glas/atbd.html.

Burgess, E. W., R. R. Forster, J. E. Box, E. Mosley-Thompson, D. H. Bromwich, R. C. Bales, L. C. Smith (2009), A spatially calibrated model of annual accumulation rateon

the Greenland ice sheet (1958-2007), *Journal of Geophysical Research (Earth Surface),* accepted 5 Oct 2009.

Cappelen, J., B. V. Jørgensen, E. V. Laursen, L. S. Stannius and R. S. Thomsen (2001), The Observed Climate of Greenland, 1958-99 - with Climatological Standard Normals, 1961-90, Danish Meteorological Institute, Ministry of Transport technical Report 00-18.

Carballo, G. F. and P. W. Fieguth (2002). Hierarchical network flow phase unwrapping. *IEEE Transactions on Geoscience and Remote Sensing, 40*(8), 1695-1708.

Curlander, J. C. and R. N. McDonough (1991). *Synthetic Aperture Radar: Systems and Signal Processing.* John Wiley & Sons, New York, 647 pp.

Dall, J., S. N. Madsen, K. Keller, and R. Forsberg (2001). Topography and penetration of the Greenland Ice Sheet measured with airborne SAR interferometry. *Geophysical Research Letters, 28*(9), 1703-1706.

Das, S. B., I. Joughin, M. D. Behn, I. M. Howat, M. A. King, D. Lizarralde, M. P. Bhatia, (2008), Fracture propagation to the base of the Greenland Ice Sheet during supraglacial lake drainage. *Science, 320*(5877), 778-781.

DiMarzio, J., A. Brenner, R. Schutz, C. A. Shuman, and H. J. Zwally. (2007), *GLAS/ICESat 1 km laser altimetry digital elevation model of Greenland*. Boulder, Colorado USA: National Snow and Ice Data Center. Digital media.

Dixon, T. (ed.) (1994). SAR interferometry and surface change detection. Workshop in Boulder, February 3 and 4 (a report). Available online at http://southport.jpl.nasa.gov/scienceapps/dixon/index.html.

Dowdeswell, J. A., G. S. Hamilton, and J. O. Hagen (1991), The duration of the active phase on surge-type glaciers – contrasts between Svalbard and other regions, Journal of Glaciology, 37(27), 388-400.

Dowdeswell J. A., J. O. Hagen, H. Björnsson, A. F. Glazovsky, W. D. Harrison, P. Holmund, J. Jania, R. M. Koerner, B. Lefauconnier, C. S. L. Ommanney and R. H. Thomas. (1997), The mass balance of circum-Arctic glaciers and recent climate change. *Quaternary Research, 48,* 1-14.

Dowdeswell, J A. et al., (2002), Form and Flow of the Academy of Sciences ice cap, severnaya Zemlya, Russian High Arctic, Journal of Geophysical Research – Solid Earth, 107(B4), 2076.

Dyurgerov M. B. and M. F. Meier (2000), Twentieth century climate change: Evidence from small glaciers, *Proceedings of the National Academy of Sciences of the United States of America, 97*(4), 1406-1411.

Echelmeyer, K., and W. D. Harrison (1990), Jokobshavn Isbrae, west Greenland: seasonal variations in velocity – or lack therof. *Journal of Glaciology, 36*, 82-88.

Engelhardt, H and B. Kamb (1998), Basal sliding of Ice Stream B, West Antarctica, *Journal of Glaciology, 44*(147), 223-230.

Farrell, S. L., S. W. Laxon, D. C. McAdoo, D. Yi, and H. J. Zwally (2009), Five years of Arctic sea ice freeboard measurements from the Ice, Cloud and land Elevation Satellite, *Journal of Geophysical Research, 114*, C04008, doi:10.1029/2008JC005074.

Fialko, Y., D. Sandwell, M. Simons and P. Rosen (2005), Three-dimensional deformation caused by the Bam, Iran, earthquake and the origin of shallow slip deficit, *Nature, 435*, 295-299

Flowers, G.E., H. Björnsson, Á. Geirsdóttir, G.H. Miller and G.K.C. Clarke. (2007), Glacier fluctuation and inferred climatology of Langjökull ice cap through the Little Ice Age. *Quaternary Science Review, 22,* 2337-2353.

Forster, R. R., K. C. Jezek, L. Koenig, and E. Deeb (2003). Measurement of glacier Geophysical Properties from InSAR Wrapped Phase*, IEEE Transactions on Geoscience and Remote Sensing, 41*(11), 2595-2604.

Fricker, H. A., T. Scambos, R. Bindschadler and L. Padman (2007), An Active Subglacial Water System in West Antarctica Mapped from Space, *Science, 315*(5818), 1544-1548.

Funk, M., K. Echelmeyer and A. Iken (1994), Mechanisms of fast-flow at Jakobshavn Isbrae, West Greenland. 2. Modeling of emglacial temperatures, *Journal of Glaciology, 40*(136), 569-585.

Geirsdottir, A., G. H. Miller, N. J Wattrus, H. Björnsson and K. Thors. (2008), Stabilization of glaciers terminating in closed water bodies: Evidence and broader implications. *Geophysical Research Letters, 35*, L17502, doi:10.1029/2008GL034432

Gens, R. (1998). Quality assessment of SAR interferometric data. PhD thesis, University of Hannover, Germany, 141 pp.

Gens, R. (2003). Two-dimensional phase unwrapping for radar inteferometry: Developments and new challenges. *International Journal of Remote Sensing, 24*(4), 703-710.

Gens, R. and J. L. van Genderen (1996). Analysis of the geometric parameters of SAR interferometry for spaceborne systems. *International Archives of Photogrammetry and Remote Sensing (Vol. XXXI, Part B2).* ISPRS, Vienna, pp. 107-110.

Glen, J. W., (1955), The Creep of Polycrystalline Ice. Proceedings of the Royal Society of London. *Series A, Mathematical and Physical, 228*(1175), 519-538

Goldstein, R. (1995). Atmospheric limitations to repeat-track radar interferometry. *Geophysical Research Letters, 22*(18), 2517-2520.

Goldstein, R. M., H. A. Zebker, and C. L. Werner (1988). Satellite radar interferometry: Two-dimensional phase unwrapping. *Radio Science, 23*(4), 713-720.

Goldstein, R. M., H. Engelhardt, B. Kamb, and R. M. Frolich (1993). Satellite radar interferometry for monitoring ice sheet motion: Application to an Antarctic ice stream. *Science, 262*(5139), 1525-1530.

Goodwin, I. D. (1990). Snow accumulation and surface topography in the katabatic zone of eastern Wilkes Land, Antarctica. *Antarctic Science, 2*(3), 235-242.

Graham, L. C. (1974). Synthetic interferometer radar for topographic mapping. *Proceedings of the IEEE, 62*(6), 763-768.

Gray, L., N. Short, R. Bindschadler, I. Joughin, L. Padman, P. Vornberger and A. Khananian (2002), Radarsat interferometry for Antarctic grounding-zone mapping. *Annals of Glaciology, 34*, 269-276.

Gray, L., K. E. Mattar, and G. Sofko (2000). Influence of ionospheric electron density fluctuations on satellite radar interferometry. *Geophysical Research Letters, 27*(10), 1451-1454.

Gudmundsson, S., J. M. Carstensen, and F. Sigmundsson (2002). Unwrapping ground displacement signals in satellite radar interferograms with aid of GPS and MRF regularization. *IEEE Transactions on Geoscience and Remote Sensing, 40*(8), 1743-1754.

Guðmundsson, S., H. Björnsson, G. Aðalgeirsdóttir, T. Jóhannesson, F. Pálsson and O. Sigurðsson (2009). Similarities and differences in the response of two ice caps in Iceland to climate warming. *Hydrology Research,* (in press).

Guneriussen, T., K. A. Hogda, H. Johnsen, and I. Lauknes (2001). InSAR for estimation of changes in snow water equivalent of dry snow. *IEEE Transactions on Geoscience and Remote Sensing, 39*(10), 2101-2108.

Hall, D. K., J. E. Box, K. A. Casey, S. J. Hook, C. A. Shuman, K. Steffen (2008) Comparison of satellite-derived and in-situ observations of ice and snow surface temperatures over Greenland. *Remote Sensing of Environment 112* : 3739 DOI 10.1016/j.rse.2008.05.007.

Hanna, E., P. Huybrechts, I. Janssens, J. Cappelen, K. Steffen and A. Stephens (2005). Runoff and mass balance of the Greenland ice sheet. *Journal of Geophysical Research-Atmospheres, 110*, 1958-2003

Hanna, E., J. Cappelen, X. Fettweis, P. Huybrechts, A. Luckman and M. H. Ribergaard (2009), Hydrologic response of the Greenland ice sheet: the role of oceanographic warming, *Hydrological Processes, 23*, 7-30.

Helk , J. V. and M. Dunbar (1953). Ice islands: evidence from North Greenland, *Arctic,6*(4): 263-271.

Higgins, A. K., (1991) North Greenland Glacier Velocities and Calf Ice Production. *Polarforschung 60* (1): 1-23.

Hilley, G. E., R. Burgmann, A. Ferretti, F. Novali and F. Rocca (2004), Dynamics of slow-moving landslides from permanent scatterer analysis, *Science, 304*(5679), 1952-1955.

Hoen, E. W. and H. A. Zebker (2000). Penetration depths inferred from interferometric volume decorrelation observed over the Greenland Ice Sheet. *IEEE Transactions on Geoscience and Remote Sensing, 38*(6), 2571-2583.

Hoen, E. W. and H. A. Zebker (2000b). Topography-driven variations in backscatter strength and depth observed over the Greenland Ice Sheet with InSAR. Proceedings of International Geoscience and Remote Sensing Symposium IGARSS '00. *Institute of Electrical and Electronic Engineers, Piscataway, NJ, Vol. 2*, pp. 470-472.

Holland, D. M., R. H. Thomas, B. De Young, M. H. Ribergaard and B. Lyberth (2008), Acceleration of Jakobshavn Isbrae triggered by warm subsurface ocean waters, *Nature Geoscience, 1*, 659-664.

Howat, I.M., I. Joughin, S. Tulaczyk, and S. Gogineni, (2005). Rapid retreat and acceleration of Helheim Glacier, east Greenland. *Geophysical Research Letters, 32,* L22502, doi:10.1029/2005GL024737.

Humphrey, N.F. and C.F. Raymond. (1994). Hydrology, erosion and sediment production in a surging glacier: Variegated Glacier,Alaska, 1982–83. *Journal of Glaciology, 40*(136), 539–552.

Huntley, J. M. (1989). Noise-immune phase unwrapping algorithm. *Applied Optics, 23*, 3268-3270.

Hurrell, J. W. (1995), Decadal Trends in the North Atlantic Oscillation: Regional Temperatures and Precipitation, *Science, 269*(5224), 676-679.

Iken, A. (1974), Velocity fluctuations of an Arctic valley glacier, a study of the White glacier, Axel Heiberg Island, Canadian Arctic Archipelago. *Axel Heiberg Research Reports, Glaciology 5*. Montreal: McGill University.

Iken, A. and R. A. Bindschadler (1986). Combined Measurements of Subglacial Water-Pressure and Surface Velocity of Findelengletscher, Switzerland - Conclusions About Drainage System and Sliding Mechanism. *Journal of Glaciology, 32*(110), 101-119.

Jezek, K. and E. Rignot (1994). Katabatic wind processes on the Greenland Ice Sheet. *EOS, Transactions of the American Geophysical Union, 75*(Suppl. 212), 44.

Joughin, I. (1995). Estimation of ice sheet topography and motion using interferometric synthetic aperture radar. PhD thesis, University of Washington, Seattle, WA.

Joughin, I. (2002). Ice-sheet velocity mapping: A combined interferometric and speckle-tracking approach. *Annals of Glaciology, 34*, 195-201.

Joughin, I. R. and D. P. Winebrenner (1994). Effective number of looks for a multi-look interferometric phase distribution, Proceedings of International Geoscience and Remote Sensing Symposium IGARSS '94, Pasadena, CA. *Institute of Electrical and Electronic Engineers, Piscataway, NJ*, pp. 2276-2278.

Joughin, I. R., D. P. Winebrenner, and M. A. Fahnestock (1995). Observations of ice-sheet motion in Greenland using satellite radar interferometry. *Geophysical Research Letters, 22*, 571-574.

Joughin, I., D. Winebrenner, M. Fahnestock, R. Kwok, and W. Krabill (1996a). Measurement of ice-sheet topography using satellite-radar interferometry. *Journal of Glaciology, 42*(140), 10-22.

Joughin, I., R. Kwok, and M. Fahnestock (1996b). Estimation of ice-sheet motion using satellite radar interferometry: Method and error analysis with application to Humboldt Glacier, Greenland. *Journal of Glaciology, 42*(142), 564-575.

Joughin, I., S. Tulaczyk, M. Fahnestock, and R. Kwok (1996c). A mini-surge on the Ryder Glacier, Greenland observed via satellite radar interferometry. *Science, 274,* 1525-1530.

Joughin, I. R., R. Kwok, and M. A. Fahnestock (1998). Interferometric estimation of three dimensional ice-flow using ascending and descending passes. *IEEE Transactions on Geoscience and Remote Sensing, 36*(1), 25-37.

Joughin, I.R., M. Fahnestock, R. Kwok, P. Gogineni and C. Allen (1999), Ice flow of Humboldt, Petermann and Ryder Gletscher, northern Greenland. *Journal of Glaciology, 45*(150), 231-241.

Joughin, I.R., M. Fahnestock, J. Bamber (2000), Ice flow in the northeast Greenland ice stream. *Annals of Glaciology, 31*, 141-146.

Joughin, I., W. Abdalati, and M. Fahnestock, (2004). Large fluctuations in speed on Greenland's Jakobshavn Isbræ glacier. *Nature, 432*, 608–610.

Joughin, I., S. B. Das, M. A. King, B. E. Smith, I. M. Howat and T. Moon (2008).
Joughin, I., R. A. Bindschadler, M. A. King, D. Voigt, R. B. Alley, S, Anandakrishnan, H. Horgan, L. Peters, P. Winberry, S. B. Das and G. Catania (2005), Continued deceleration of Whillans Ice Stream, West Antarctica, *Geophysical Research Letters, 32*, L22501, doi:10.1029/2005GL024319.

Seasonal speedup along the western flank of the Greenland Ice Sheet. *Science, 320*(5877), 781-783.

Just, D. and R. Bamler (1994). Phase statistics of interferograms with applications to synthetic aperture radar. *Applied Optics, 33*(20), 4361-4368.

Kamb, B. (1987). Glacier surge mechanism based on linked cavity configuration of the basal water conduit system. *Journal of Geophysical Research, 92*(B9), 9083–9100.

Kamb, B., H. Engelhardt, M. Fahnestock, N. Humphrey, M. Meier and D. Stone (1994), Mechanical and hydrological basis for the rapid motion of a large tidewater glacier. 2. Interpretation, *Journal of Geophysical Resarch – Solid Earth, 99*(B8), 15231-15244.

Kelly, M.A. and T. V. Lowell (2009) Fluctuations of local glaciers in Greenland during latest Pleistocene and Holocene time, *Quaternary Science Reviews,* doi:10.1016/j.quascirev.2008.12.008

King, D. A. (2004), Climate Change Science: Adapt, Mitigate, or Ignore? *Science, 303*, 176-177.

King, E. C., J. Woodward and A. M. Smith (2007). Seismic and radar observations of subglacial bed forms beneath the onset zone of Rutford Ice Stream, Antarctica, *Journal of Glaciology, 53*(183), 665-672.

Kjær, K. H., E. Larsen, J. van der Meer, O. Ingolfsson, J. Kruger, I. O. Benediktsson, C. G. Knudsen and A. Schomacker (2006), Subglacial decoupling at the sediment/bedrock interface: a new mechanism for rapid flowing ice, *Quaternary Science Reviews, 25*, 2704-2712.

Koch, L. (1935). A Day in North Greenland, *Geografiska Annaler, 17*, Supplement: Hyllningsskrift Tillagnad Sven Hedin, 609-620

Krabill, W., W. Abdalati, E. Frederick, S. Manizade, C. Martin, J. Sonntag, R. Swift, R. Thomas, W. Wright, J. Yungel. (2000),Greenland Ice Sheet: High-Elevation Balance and Peripheral Thinning *Science 289*, 428-430. doi: 10.1126/science.289.5478.428.

Krabill, W., R. Thomas, K. Jezek, K. Kuivinen, and S. Manizade (1995). Greenland Ice-Sheet thickness changes measured by laser altimetry. *Geophysical Research Letters, 22*(17), 2341-2344.

Krabill, W., E. Hanna, P. Huybrechts, W. Abdalati, J. Cappelen, B. Csatho, E. Frederick, S. Manizade, C. Martin, J. Sonntag, R. Swift, R. Thomas, and J. Yungel, (2004). Greenland ice sheet: Increased coastal thinning, *Geophysical Research Letters, 31,* L24402, doi:10.1029/2004GL021533.

Krieger, G, A. Moreira, H. fiedler, I. Hajnsek, M. Werner, M. Younis and M. Zink (2007), TanDEM-X: A satellite Formation for High-Resolution SAR Interferometry, *IEEE Transactions on Geoscience and Remote Sensing, 45*(11), 3317-3341.

Kropatsch, W. G. and D. Strobl (1990). The generation of SAR layover and shadow maps from digital elevation models. *IEEE Transactions on Geoscience and Remote Sensing, 28*, 98-107.

Kwok, R. and M. A. Fahnestock (1996). Ice sheet motion and topography from radar interferometry. *IEEE Transactions on Geoscience and Remote Sensing, 34*(1), 189-200.

Lang, K. (1999). The Sun. In Beatty, Petersen, Chaiken Eds. *The New Solar System*, Cambridge, pp 422.

Lemke, P., J. Ren, R.B. Alley, I. Allison, J. Carrasco, G. Flato, Y. Fujii, G. Kaser, P. Mote, R.H. Thomas and T. Zhang, (2007). Observations: Changes in Snow, Ice and Frozen Ground. In: Climate Change 2007: The Physical Science Basis. Contribution of Working Group I to the Fourth Assessment Report of the Intergovernmental Panel on Climate Change [Solomon, S., D. Qin, M. Manning, Z. Chen, M. Marquis, K.B. Averyt, M. Tignor and H.L. Miller (eds.)]. Cambridge University Press, Cambridge, United Kingdom and New York, NY, USA.

Lemke, P., J. Ren, R. B. Alley, I. Allison, J. Carrasco, G. Flato, Y. Fuji, G. Kaser, P. Mote, R. H. Thomas and T, Zhang (2007), Observations: Changes in Snow, Ice and Frozen Ground. In: *Climate Change 2007: The Physical Science Basis. Contribution of Wworking Group I to the Fourth Assessment Report of the Intergovernmental Panel on Climate Change* [Solomon, S., D. Qin, M. Manning, Z. Chen, M. Marquis, K.B. Averyt, M.Tignor and H. L. Miller (eds.)]. Cambridge University Press, Cambridge, United Kingdom and New York, NY, USA.

Liestøl, O. (1969). Glacier surges in West Spitsbergen. *Canadian Journal of Earth Sciences 6*(4), 895–897.

Luckman, A. and T. Murray (2005), Seasonal variation in velocity before retreat of Jakobshavn Isbrae, Greenland, *Geophysical Research Letters*, *32*, L08501, doi:10.1029/2005GGGL022519.

Luckman A., T. Murray, T. Strozzi (2002). Surface flow evolution throughout a glacier surge measured by satellite radar interferometry. *Geophysical Research Letters, 29*(23).

Luckman, A., T. Murray, R. de Lange and E. Hanna (2006). Rapid and synchronous ice-dynamic changes in East Greenland. *Geophysical Research Letters, 33*, L03503.

Madsen, S. and H.A. Zebker (1998) Imaging radar interferometry. In: F. Henderson and A. J. Lewis (eds.), Principles and Applications of Imaging Radar: Manual of Remote Sensing (3rd edn., Vol. 2, R. A. Ryerson, editor-in-chief). John Wiley & Sons, New York, pp.359-380.

Madsen, S. N., J. J. Mohr, and N. Reeh (1999). Mapping Greenland by ERS-1/2 InSAR for ice mass balance and dynamics studies. *Proceedings of ESA Fringe '99 Meeting, November 10-12, Liege, Belgium* (CD-ROM, ESA Special Publication SP-478). ESA, Noordwijk, The Netherlands. Available online at http://www.esa.int/fringe99.

Maidment, D.R. (Editor), (2002). *ArcHydro: GIS for Water Resources*. ESRI Press, Redlands, California.

Mair, D., P. Nienow, I. Willis and M. Sharp (2001) Spatial patterns of glacier motion during a high-velocity event: Haut Glacier d'Arolla, Switzerland, *Journal of Glaciology, 47*(156), 9-20.

Massom, R. and D. Lubin (2006), *Polar Remote Sensing*, Springer Praxis Books, 426pp.

Massonnet, D. (1997). Satellite radar interferometry. *Scientific American, February,* 46-53.

Massonnet, D. and H. Vadon (1995). ERS-1 internal clock drift measured by interferometry. *IEEE Transactions on Geoscience and Remote Sensing, 33*(2), 401-408.

Massonnet, D. and K. L. Feigl (1998). Radar interferometry and its application to changes in the Earth's surface. *Reviews of Geophysics, 36*(4), 441-500.

Massonnet, D. and T. Rabaute (1993). Radar interferometry: Limits and potential. *IEEE Transactions on Geoscience and Remote Sensing, 31*(2), 455-464.

Massonnet, D., M. Rossi, C. Carmona, F. Adragna, G. Peltzer, K. Feigl and T. Rabaute (1993), The displacement field of the Landers earthquake mapped by radar interferometry, *Nature, 364*, 138-142.

McConnell, J. R., R. J. Arthern, E. Mosley-Thompson, C. H. Davis, R. C. Bales, R. Thomas, J. F. Burkhart and J. D. Kyne (2000), Changes in Greenland ice sheet elevation attributed primarily to snow accumulation variability, *Nature, 406*, 877-880.

McLeod, I. H., I. G. Cumming, and M. S. Seymour (1998). Envisat ASAR data reduction: Impact on SAR interferometry. *IEEE Transactions on Geoscience and Remote Sensing, 36*(2), 589-602.

McMillan, M., P. Nienow, A. Shepherd, T. Benham, and A. Sole (2007). Seasonal evolution of supra-glacial lakes on the Greenland Ice Sheet. *Earth and Planetary Science Letters, 262*(3-4), 484-492.

Mecatti , D., L. Noferini, G. Macaluso, M. Pieraccini, G. Luzi, C. Atzeni and A. Tamburini (2007), Remote sensing of glacier by ground-based radar interferometry, *IEEE IGARSS Symposium, 1-12*, 4501-4504.

Meehl, G. A., et al. (2007), Global Climate Projections, in Climate Change 2007: The Physical Science Basis. Contribution of Working Group I to the Fourth Assessment Report of the Intergovernmental Panel on Climate Change, edited by S. Solomon, D. Qin, M. Manning, Z. Chen, M. Marquis, K. B. Averyt, M. Tignor and H. L. Miller, pp. 747-846, Cambridge Univ. Press, New York. 2007.

Meier, M. F., M. B. Dyurgerov, U. K. Rick, S. O'Neel, W. T. Pfeffer, R. S. Anderson and A. F. Glazovsky (2007), Glaciers Dominate Eustatic Sea-Level rise in the 21st Century, *Science, 317*, 1064-1067.

Meier, W., J. Stroeve and F. Fetterer (2007), Whither Arctic sea ice? A clear signal of decline regionally, seasonally and extending beyond the satellite record, *Annals of Glaciology, 46*, 428-434.

Mernhild, S. H. and B. Hasholt (2009), Observed runoff, jokulhlaups and suspended sediment load from the Greenland ice sheet at Kangerlussuaq, West Greenland, 2007 and 2008, *Journal of Glaciology, 55*(193), 855-858.

Meyer, F. (2004). Topography and displacement of polar glaciers from multi-temporal SAR interferograms: Potentials, error analysis and validation. Proceedings of the XXth ISPRS Congress, July 12-23, Istanbul (Commission 3). International Society for Photogrammetry and Remote Sensing, Istanbul, Turkey.

Milankovitch, M., (1941). Kanon der Erdbestrahlung und seine Anwendung auf das Eiszeitproblem. *Special Publication of Königliche Serbische Akademie Belgrad, 133*.

Mohr, J. J. (1997). Repeat track SAR interferometry: An investigation of its utility for studies of glacier dynamics. PhD thesis, Technical University of Denmark, Copenhagen.

Mohr, J. J. and S. N. Madsen (1996). Multi-pass interferometry for studies of glacier dynamics. *Proceedings of "Fringe 96" Workshop on ERS SAR Interferometry*, Zurich, Switzerland (ESA SP-406). ESA, Noordwijk, The Netherlands, pp. 345-352.

Mohr, J. J., N. Reeh, and S. N. Madsen (1998). Three dimensional glacial flow and surface elevation measured with radar interferometry. *Nature, 391*(6664), 273-276.

Mohr, J. J., N. Reeh, and S. N. Madsen (2003). Accuracy of three-dimensional glacier surface velocities derived from radar interferometry and ice-sounding radar measurements. *Journal of Glaciology, 49*(165), 210-222.

Moreira, A, G. Krieger, I. Hajnsek, D. Hounam and M. Werner (2004), TanDEM-X: A TerraSAR-X Add-On Satellite for Single-Pass SAR Interferometry, *IGARSS 2004*.

Nakamura, K., K. Doi and K. Shibuya (2007). Estimation of seasonal changes in the flow of Shirase glacier using JERS-1/SAR image correlation. *Polar Science 1*, 73-83.

National Snow and Ice Data Centre, (2007). http://nsidc.org/data/docs/daac/nsidc0304_0305_glas_dems.gd.html

Noferini, L., M. Pieraccini, D. Mecatti, G. Macaluso, G. Luzi and C. Atzeni (2007), DEM by ground-based SAR interferometry*, IEEE Geoscience and Remote Sensing Letters*, 4(4), 659-663.

Olmsted, C. (1993). *Alaska SAR Facility Scientific SAR User's Guide (ASF-SD-003)*. Alaska SAR Facility, Juneau, 53 pp.

Parizek, B. R. and R. B. Alley, (2004). Implications of increased Greenland surface melt under global-warming scenarios: Ice-sheet simulations, *Quaternary Science Reviews, 23*, 1013-1027.

Paterson, W. S. B. (1994). The Physics of Glaciers (3rd edn.). Pergamon/Elsevier Science, Oxford, UK, 480 pp.

Paterson, W. S. B., (2004). The Physics of Glaciers, Ed. 3.A, Elsevier, Oxford, UK, 496pp.

Pritchard H. D., R. J. Arthern, D. G. Vaughan, L. A. Edwards, (2009) Extensive dynamic thinning on the margins of the Greenland and Antarctic ice sheets. *Nature,* advance online publication 23 September 2009, doi:10.1038/nature08471.

Raper, S. C. B. and R. J. Braithwaite (2006). Low sea level rise projections from mountain glaciers and ice caps under global warming. *Nature, 439*, 311-313.

Reeh, N. and N. Gundestrup (1985). Mass balance of the Greenland Ice Sheet at Dye 3. *Journal of Glaciology, 31*(108), 198-200.

Reeh, N. (1991). Parameterization of Melt Rate and Surface Temperature on the Greenland Ice Sheet. *Polarforschung 59*, 113-128.

Reeh, N., J. J. Mohr, S. N. Madsen, H. Oerter, and N. Gundestrup (2003). Three-dimensional surface velocities of the Storstrummen Glacier derived from radar interferometry and ice-sounding radar measurements. *Journal of Glaciology, 49*(165), 201-209.

Reeh, N., S. N. Madsen, and J. J. Mohr (1999). Combining SAR interferometry and the equation of continuity to estimate the three-dimensional glacier surface velocity. *Journal of Glaciology, 45*(151), 533-538.

Rees, W. G. (2001). Physical Principles of Remote Sensing (2nd edn). Cambridge University Press, Cambridge, UK, 372 pp.

Rignot E. and S. S. Jacobs (2002). Rapid bottom melting widespread near Antarctic ice sheet grounding lines. *Science, 296*(5575), 2020-2023.

Rignot, E. (1998), Fast Recession of a West Antarctic Glacier, *Science, 281*(5376), 548 551.

Rignot, E. (1996). Tidal motion, ice velocity and melt rate of Petermann Gletscher, Greenland, measured from radar interferometry. *Journal of Glaciology, 42*(142), 476-485.

Rignot, E. and R.H. Thomas (2002). Mass balance of polar ice sheets. *Science, 297,* 1502-1506.

Rignot, E., and P. Kanagaratnam (2006). Changes in the velocity structure of the Greenland Ice Sheet. *Science, 311*, 986–990.

Rignot, E., S. P. Gogineni, W. B. Krabill and S. Ekholm (1997), North and northeast Greenland ice discharge from satellite radar interferometry. *Science, 276*, 934-937.

Rignot, E., K. Echelmeyer, and W. B. Krabill (2001). Penetration depth of interferometric synthetic-aperture radar signals in snow and ice. *Geophysical Research Letters, 28*(18), 3501-3504.

Rignot, E. (2007), Ice motion mapping in Antarctica with Envisat ASAR and ALOS PALSAR, *Fringe 2007 meeting*, ESA, Frascati, Italy.

Rignot, E. (2008), Changes in West Antarctic ice stream dynamics observed with ALOS PALSAR, *Geophysical Research Letters, 35*, L12505, doi:10.1029/2008GL033365.

Rinne, E. and S. Palmer (in preparation), Elevation changes measured at Flade Isblink ice cap, eastern North Greenland.

Robinson, D. (1993). Phase unwrapping methods. In: W. R. Robinson and G. T. Reid (eds.), Interferogram Analysis: Digital Fringe Pattern Measurement Techniques. Institute of Physics, Bristol, pp. 194-229.

Rocca, F., C. Prati, and A. Ferretti (1997). An overview of SAR interferometry. In: T. D.Guyenne (ed.), Proceedings of 3rd ERS Symposium, Space at the Service of Our Environment, Florence, Italy, 17-21 March 1997. ESA, Noordwijk, The Netherlands. Available online at http://earth.esa.int/symposia/program-details/speeches/rocca-et-al/.

Rosen, P. A., S. Hensley, I. R. Joughin, F. K. Li, S. N. Madsen, E. RodrõÂguez, and R. M.Goldstein (2000). Synthetic aperture radar interferometry. *Proceedings of the IEEE, 88*(3), 333-382.

Rosen, P. A., C. W. Werner, A. Hiramatsu (1994). Two-dimensional phase unwrapping of SAR interferograms by charge connection through neutral trees, *Proceedings of IGARSS'94*, Pasadena, 8-12 August, 1994.

Rott, H. and A. Siegel (1996). Glaciological studies in the Alps and in Antarctica using ERS interferometric SAR. Proceedings of ``Fringe '96" Workshop on ERS SAR Interferometry, Zurich, Switzerland, September 30-October 2 (Vol. 2, ESA SP-406). ESA, Noordwijk, The Netherlands, pp. 149-159.

Rufino, G., A. Moccia, and S Asposito (1996). DEM generation by means of ERS tandem data. Proceedings of ``Fringe '96" Workshop on ERS SAR Interferometry, Zurich, Switzerland, September 30-October 2. ESA, Noordwijk, The Netherlands.

Samson, J. (1996). Coregistration in SAR interferometry. Master's thesis, Faculty of Geodetic Engineering, Delft University of Technology.

Sandwell, D. and E. Price (1998). Phase gradient approach to stacking interferograms. *Journal of Geophysical Research, 103*(B12), 30183-30204.

Scambos, T. A., M. J. Dutkiewtz, J. C. Wilson, R. A. Bindschadler (1992). Application of image cross-correlation to the measurement of glacier velocity using satellite image data. *Remote Sensing of the Environment, 42*(3), 177-186.

Scambos, T. A., J. A. Bohlander, C. A. Shuman, and P. Skvarca (2004), Glacier acceleration and thinning after ice shelf collapse in the Larsen B embayment, Antarctica, *Geophysical Research Letters, 31*, L18402, doi:10.1029/2004GL020670.

Scharroo, R. and P. N. Visser (1998). Precise orbit determination and gravity field improvement for the ERS satellites. *Journal of Geophysical Research, 103*(C4), 8113-8127.

Schimpp, O. (1958), Der Eishaushalt am Hintereisferner in den Jahren 1952-1953 und 1953-1954, *International Association of Scientific Hydrology Publication, 4*, 301-314.

Shabtaie, S. and C. R. Bentley (1987), West Antarctic ice streams draining into the Ross Ice Shelf: configuration and mass balance, *Journal of Geophysical Research, 92*, 1311-1136.

Sharov, A. I. and K. Gutjahr (2002). Some methodological enhancements to InSAR surveying of polar ice caps. Observing Our Environment from Space: Proceedings of 21st EARSel Symposium. European Association of Remote Sensing Laboratories, Hannover, Germany, pp. 65-72.

Sharov, A. I., K. Gutjahr, F. Meyer, and M. Schardt (2002). Methodical alternatives to the glacier motion measurement from differential SAR interferometry. *International Archives of Photogrammetry and Remote Sensing, XXXIV*(3A), 324-329.

Shepherd A. and D. Wingham (2007). Recent sea-level contributions of the Antarctic and Greenland ice sheets. *Science, 315*(5818), 1529-1532.

Shepherd, A., D. J. Wingham, J. A. D. Mansley, H. F. J. Corr (2001). Inland Thinning of Pine Island Glacier, West Antarctica, *Science, 291*(5505), 862-864.

Shepherd, A., A. Hubbard, P. Nienow, M. King, M. McMillan, and I. Joughin, (2009). Greenland ice sheet motion coupled with daily melting in late summer. *Geophysical Research Letters,* doi:10.1029/2008GL035758, in press.

Smith A.M., and T. Murray (2009). Bedform topography and basal conditions beneath a fast-flowing West Antarctic ice stream. *Quaternary Science Reviews, 28*(7-8), 584-596.

Smith, A. M., T. Murray, K. W. Nicholls, K. Makinson, G. Aoalgeirsdottir, A. E. Behar, D. G.Vaughan (2007). Rapid erosion, drumlin formation, and changing hydrology beneath an Antarctic ice stream. *Geology, 35* (2), 127-130.

Smith, B. D., B. E. Engelhardt, and D. H. Mutz (2002). The Radarsat-MAMM Automated Mission Planner. *Artificial Intelligence Magazine, 23*(2), 25-36.

Sneed, W. A. and G. S. Hamilton (2007), Evolution of melt pond volume on the surface of the Greenland Ice Sheet, *Geophysical Research Letters, 34*(3), L03501.

Solaas, G. A. (1994). ERS-1 Interferometric Baseline Algorithm Verification (Technical Report ES-TN-DPE-OM-GS02, version 1.0. ESA/ESRIN, Noordwijk, The Netherlands. Available online at http://gds.esrin.esa.it:80/CEFB565F/CORBITS.

Sole, A., T. Payne, J. Bamber, P. Nienow and W. Krabill (2008), Testing hypotheses of the cause of peripheral thinning of the Greenland Ice Sheet: is land-terminating thinning at anomalously high rates?, *The Cryosphere, 2*, 205-218.

Solomon, S., D. Qin, M. Manning, R. B. Alley, T. Berntsen, N.L. Bindoff, Z. Chen, A. Chidthaisong, J.M. Gregory, G.C. Hegerl, M. Heinmann, B. Hewitson, B.J. Hoskins, F. Joos, J. Jouzel, V. Kattsov, U. Lohmann, T. Matsuno, M. Molina, N. Nicholls, J. Overpeck, G. Raga, V. Ramaswamy, J. Ren, M. Rusticucci, R. Somerville, T.F. Stocker, P. Whetton, R.A. Wood and D. Wratt (2007). "Technical Summary" in Climate Change 2007: Physical Science Basis. Contribution of Working Group I to the Fourth Assessment Report of the Intergovernmental Panel on Climate Change [Solomon, S., D. Qin, M. Manning, Z. Chen, M. Marquis, K.B. Averyt, M. Tignor and H.L. Miller (eds.)]. Cambridge University Press, Cambridge, United Kingdom and New York, NY, USA.

Steffen, K. and J. Box, (2001). Surface climatology of the Greenland ice sheet: Greenland climate network 1995-1999. *Journal of Geophysical Research-Atmospheres 106*, 33951-33964.

Steffen, K., S. V. Nghiem, R. Huff, and G. Neumann, (2004). The melt anomaly of 2002 on the Greenland Ice Sheet from active and passive microwave satellite observations, *Geophysical Research Letters, 31*(20),L2040210.1029/2004GL020444.

Strozzi, T., A. Luckman, and T. Murray (2000). The evolution of a glacier surge observed with the ERS satellites. Proceedings of ERS-Envisat Symposium, Gothenburg, Sweden, October 16-20. ESA, Nordwijk, The Netherlands.

Strozzi, T., A. Luckman, T. Murray, U. Wegmuller and C. Werner (2002). Glacier motion estimation using SAR offset-tracking procedures. *IEEE Transactions on Geoscience and Remote Sensing, 40* (11), 2384-2391.

Strozzi, T., U. Wegmuller, and C. Matzler (1999). Mapping wet snow covers with SAR interferometry. *International Journal of Remote Sensing, 20*(12), 2395-2403.

Sundal, A. V., A. Shepherd, P. Nienow, E. Hanna, S. Palmer and P. Huybrechts (2009) Evolution of supra-glacial lakes across the Greenland Ice Sheet, *Remote Sensing of the Environment, 113*, 2164-2171.

Thomas, R. H. (2004). Force-perturbation analysis of recent thinning and acceleration of Jakobshavn Isbrae, Greenland. *Journal of Glaciology, 50*, 57–66.

Thomas, R., Abdalati, E. Frederick, W. B. Krabill, S. Manizade and K. Steffen (2003), Investigation of surface melting and dynamic thinning on Jakobshavn Isbrae, Greenland. *Journal of Glaciology, 49*, 231–239.

Toutin, T. and L. Gray (2000). State-of-the-art of elevation extraction from satellite SAR data. International Society for Photogrammetry and Remote Sensing. *Journal of Photogrammetry and Remote Sensing, 55,* 13-33.

Touzi, R., A. Lopes, J. Bruniquel, and P. W. Vachon (1999). Coherence estimation for SAR imagery. IEEE *Transactions on Geoscience and Remote Sensing, 37*(1), 135-149.

Truffer, M., W. D. Harrison and R. S. March (2005) Record negative glacier mass balances and low velocities during the 2004 heatwave in Alaska, USA: implications for the interpretation of observations by Zwally and others in Greenland, *Journal of Glaciology, 51*(175), 663-664.

Ulaby, F. T., R. K. Moore and A. K. Fung (1982). *Radar Remote Sensing and Surface Scattering and Emission Theory: Vol. 2. Microwave Remote Sensing - Active and Passive.* Addison-Wesley, Reading, MA, 1069 pp .

Usai, S. (2001). A new approach for long term monitoring of deformations by differential SAR interferometry. PhD thesis, Delft University of Technology.

van de Wal, R. S. W., W. Boot, M. R. van den Broeke, C. J. P. P. Smeets, C. H. Reijmer, J. J. A. Donker and J. Oerlemans (2008). Large and rapid melt-induced velocity changes in the ablation zone of the Greenland Ice Sheet. *Science, 321*(5885), 111-113.

van der Veen, C. J. (2007), Fracture propagation as means of rapidly transferring surface meltwater to the base of glaciers, *Geophysical Research Letters, 34*, L01501, doi:10.1029/2006GL028385.

Wegmüller, U., C. Werner and T. Strozzi. (1998) SAR interferometric and differential interferometric processing chain. *International Geoscience and Remote Sensing Symposium Proceedings, 1998 (IGARSS '98), 2*, 1106-1108.

Wegmuller, U., C. L. Werner, T. Strozzi, and A. Wiesmann (2002). Phase Unwrapping with Gamma ISP (technical report). Gamma Remote Sensing AG, Bern, Switzerland. Available online at http://www.gamma-rs.ch/docs/unwrapping.pdf.

Werner, C. L., U. Wegmuller, and T. Strozzi (2002). Processing strategies for phase unwrapping for INSAR applications. *Proceedings of 4th European Conference on Synthetic Aperture Radar EUSAR 2002*, *Cologne, Germany, 4-6 June 2002*. VDE Verlag, Frankfurt, Germany, Vol. 1, pp. 353-356.

Werner, C., T. Strozzi, A. Wiesmann, U. Wegmuller, T. Murray, H. Pritchard and A. Luckman (2001). Complimentary Measurement of Geophysical Deformation using

Repeat-Pass SAR. Geoscience *and Remote Sensing Symposium, IEEE 2001, Sydney, Australia, 7*, 3255-3258.

Werner, C., U. Wegmüller, T. Strozzi and A. Wiesmann (2000), Gamma SAR and interferometric processing of software, *ERS-Envisat Symposium, Gothenburg, Sweden, 16-20 Oct. 2000.*

Willis, I. (1995), Inter-annual variations in glacier motion: a review, *Progress in Physical Geography, 19*(1), 61-106.

Wingham, D. J., M. J. Siegert, A. Shepherd and A. S. Muir (2006). Rapid discharge connects Antarctic subglacial lakes. *Nature, 440*(7087), 1033-1036.

Wong, F., and I. G. Cumming (1996). A combined SAR Doppler centroid estimation scheme based upon signal phase*, IEEE Transactions on Geoscience and Remote Sensing, vol. 34*, 3, 696-707.

Wright, T.J., C. Ebinger, J. Biggs, A. Ayele, G. Yirgu, D. Keir and A. Stork (2006), Magma-maintained rift segmentation at continental rupture in the 2005 Afar dyking episode, *Nature, 442*, 291-294.

Wright, T.J., B. Parsons, P. C. England and E. J. Fielding (2004), InSAR observations of low slip rates on the major faults of western Tibet, *Science, 305*(5681), 236-239.

Wu, X. and K. H. Thiel (1996). The use of tandem data in the Antarctic area. *Proceedings of ``Fringe '96'' Workshop on ERS SAR Interferometry, Zurich, Switzerland (ESA SP-406).* ESA, Noordwijk, The Netherlands.

Zebker, H. A. and J. Villasenor (1992). Decorrelation in interferometric radar echoes. *IEEE Transactions on Geoscience and Remote Sensing, 30*(5), 950-959.

Zebker, H. A. and R. M. Goldstein (1986). Topographic mapping from interferometric synthetic aperture radar observations. *Journal of Geophysical Research, 91*(B5), 4993-4999.

Zebker, H. A., C. L. Werner, P. A. Rosen, and S. Hensley (1994). Accuracy of topographic maps derived from ERS-1 interferometric radar. *IEEE Transactions on Geoscience and Remote Sensing, 32*(4), 823-836.

Zebker, H. A., P. A. Rosen, R. M. Goldstein, A. Gabriel, and C. L. Werner (1994a). On the derivation of coseismic displacement fields using differential radar interferometry: The Landers Earthquake. *Journal of Geophysical Research, 99*(B10), 19617-19634.

Zhang, J. (2005), Warming of the arctic ice-ocean system is faster than the global average since the 1960s, *Geophysical Research Letters, 32*, L19602, doi:10.1029/2005GL024216.

Zwally, H. J and M. B. Giovenetto (2001). Balance mass flux and ice velocity across the equilibrium line in drainage systems of Greenland, *Journal of Geophysical Research-Atmospheres, 106*(D24), 33717-33728.

Zwally, H. J. and A. C. Brenner (2001). Ice sheet dynamics and mass balance. In: *Satellite Altimetry and Earth Science*, L-L. Fu and A. Cazenave, Eds., Academic Press, Ch. 9, 351-369.

Zwally, H. J., W. Abdalati, T. Herring, K. Larson, J. Saba and K. Steffen (2002). Surface melt-induced acceleration of Greenland ice-sheet flow. *Science, 297*(5579), 218-222.

Zwally, H. J., B. Schutz, W. Abdalati, J. Abshire, C. Bentley, A. Brenner, J. Bufton, J. Dezio, D. Hancock, D. Harding et al. (2002). ICESat's laser measurements of polar ice, atmosphere, ocean and land. *Journal of Geodynamics, 34*, 405-445.

Zwally, H. J., W. Abdalati, T. Herring, K. Larson, J. Saba and K. Steffen (2002), Surface melt-induced acceleration of Greenland ice-sheet flow. *Science, 297*(5579), 218–222.

Zwally, H. J., R. Schutz, C. Bentley, J. Bufton, T. Herring, J. Minster, J. Spinhirne, and R. Thomas (2003), updated 2009. *GLAS/ICESat L1B Global Elevation Data V018*, 2003 - 2007. Boulder, CO: National Snow and Ice Data Center. Digital media.

Appendix A: Processing chain from raw SAR data to SLC format.

A.1. Pre-processing

A.1.1. Range Spectrum Estimation

The range spectrum gives a representation of the spectral properties of a dataset across range including range chirp, noise and scatterer properties. The spectrum is retrieved by running *rspec_IQ* which applies a Fast Fourier Transform (FFT) to the raw dataset and is useful for estimating the signal-to-noise ratio (SNR) of the final image. Typically, the spectrum extends over 80 % of the digitised bandwidth. The SNR estimate is obtained by comparing the average level chirp bandwidth to the level in the noise only region. This estimate is then used for radiometric compensation of the antenna pattern gain used for calibration of the SAR image, since the antenna gain correction applies only to the signal and not the noise fraction of the SAR image.

A.1.2. Azimuth Spectrum Estimation

The azimuth spectrum of a SAR dataset contains the doppler information that will be exploited in the azimuth compression to improve the resolution of the dataset along-track. Ideally, the doppler frequency of a target decreases almost linearly passing through 0 at the point of closest approach. The doppler frequency of points at the centre of the antenna beam is called the 'doppler centroid' and under ideal conditions is zero. Non-zero doppler centroid and variation of doppler along-track can occur due to the presence of squint (when the radar look direction is not perpendicular to the flight-direction) and need to be taken into consideration when processing raw SAR image data. Squint can occur due to inaccurate pointing information or other mechanical or electrical factors.

Doppler variation along-track is primarily a result of the different contribution of the Earth's velocity to the total Earth-fixed velocity of the platform. Accurate matched filtering of the radar echoes requires the doppler history, including the ambiguities due to squint.

A.1.3. Doppler Ambiguity Resolution

The simplest method to determine the azimuth spectrum is to apply a FFT and analyse the representation of the signal in the frequency domain. When squint is present, the doppler frequency at the point of closest approach is non-zero and the spectrum is shifted, by as much as several kHz. As SAR is a sampled data system i.e. echoes are acquired at the rate of the pulse repetition frequency (PRF), aliasing can occur if the doppler centroid frequency is very large. In this case, the doppler frequency estimated from the azimuth spectrum is shifted from the true doppler frequency by an integer number of the PRF, resulting in doppler ambiguity. Processing SAR data with an aliased value of the centroid means that the estimate of the range migration rate of targets in the image is incorrect, resulting in erroneous target positions.

Several methods exist for estimating the doppler ambiguity, the most reliable being the use of precise spacecraft attitude data to estimate the squint angle, from which the doppler frequency information can be retrieved. ERS-1 and -2 utilise yaw steering in order to maintain the doppler centroid of the data within ½ of the PRF. In this case, the estimate of doppler centroid is unambiguous as it satisfies the Nyquist criterion of band-limited signals. However, the pointing algorithm for ERS makes errors in the southern hemisphere such that the actual doppler centroid is 1 or 2 multiples of the PRF. In the absence of direct measurement techniques, the most reliable method of obtaining unambiguous doppler estimates is to measure uncompensated range migration determined by correlation of images processed from different parts of the doppler spectrum. For these algorithms to work well, the fractional bandwidth of the SAR should be large and the scene relatively devoid of features.

Gamma uses two such algorithms called the Multi-Look Cross Correlation (*dop_mlcc*) and Multi-Look Beat Frequency (*dop_ambig*) algorithms, which are described by Wong and Cumming (1996).

A.2. SAR processing

A.2.1. Range compression / Azimuth prefilter

As the radar travels along the flight track, the transmitted pulses are linear frequency modulated (FM) chip signals with a large time-bandwidth product. Range compression using *pre_rc* applies a matched filter in range to the recorded data to recover the full range resolution inherent in the range chirp bandwidth by compressing the chirp energy into as narrow a time window as possible. Range compression algorithms all work similarly, though due to variations in backscatter compensation, are partly sensor-dependent. All algorithms estimate the raw data histogram and statistics, including the mean and standard deviation of each channel, and the correlation between I and Q channels in the case of IQ data.

A.2.2. Azimuth auto-focusing

For precise estimation of the along-track velocity, the program *autof* must be used. This program takes two parts of the azimuth spectrum and forms small images of the central region of the scene. If the along-track velocity estimate is correct, then the two image sections will overlay after azimuth 'deskew'. The measured offset of these two image patches are used to improve the estimate of the along-track velocity and thereby focus the image in azimuth. As this routine takes the previous best estimate as a starting point, it should be run twice to achieve the best possible focus.

A.2.3. Azimuth compression

For azimuth compression of range compressed data, the range-doppler algorithm is typically used by running *az_proc*. The range compressed data are divided into along-track patches and range migration is applied since each point in the image follows a parabolic range trajectory. The algorithm is based on the idea that all points at a particular doppler frequency will have to be migrated by the same amount at a particular range. *az_proc* also supports the radiometric calibration of the processed data using the antenna patterns provided with Gamma software.

After range and azimuth compression, the magnitude of the resulting image is non-

uniform due to the antenna gain pattern and variation in path-length which is corrected by relative calibration. Absolute radiometric calibration can then be performed using the antenna pattern. A calibrated SLC can either be in the σ_0 or g_0 form. In the σ_0 case, the SLC image intensity corresponds to the backscattering coefficient σ_0 which is normalized to the horizontal ground surface. In the case of γ_0, the SLC image intensity corresponds to the backscattering coefficient γ_0 is related to σ_0 by:

$$\gamma_0 = \frac{\sigma_0}{\cos\theta} \tag{A.1}$$

where θ is the incidence angle of the horizontal surface.

A.2.4. Multi-looking

SAR images have coherent speckle noise arising from coherent interference of signals scattered from different parts of the radar resolution element. This noise is suppressed by the incoherent summation of statistically independent images of the scene. Each of the images formed from the different Doppler bands are independent because they view the scene with different aspect angles. Further suppression of speckle noise can be achieved by local incoherent spatial averaging of pixels at the cost of reduced spatial resolution. In Gamma, multi-looking is implemented with the *multi_SLC* routine.

Ice velocity measurements of Langjökull, Iceland, from interferometric synthetic aperture radar (InSAR)

Steven PALMER,[1] Andrew SHEPHERD,[1] Helgi BJÖRNSSON,[2] Finnur PÁLSSON[2]

[1]*School of GeoSciences, University of Edinburgh, Drummond Street, Edinburgh EH8 9XP, UK*
E-mail: s.j.palmer@sms.ed.ac.uk
[2]*Institute of Earth Sciences, Building of Natural Sciences, Askja, Sturlugata 7, IS-101 Reykjavík, Iceland*

ABSTRACT. We have computed the velocity of Langjökull ice cap (LIC), Iceland, using InSAR data acquired by the European Remote-sensing Satellite in 1994 and an ice-surface elevation model derived from a GPS survey conducted in 1997. The velocity map covers 68% of the 925 km^2 of LIC. Eight principal outlet glaciers were identified, along which ice velocities increased from zero at the ice divide to a maximum of 75 m a^{-1}. When the InSAR velocity dataset is compared with surface GPS measurements of ice flow determined in summer 2001, there is generally good agreement, suggesting interannual and seasonal stability for much of the ice cap during this period. However, non-zero ice velocities at the termini of four of the eight glaciers surveyed suggest that these glaciers were advancing in 1994. Comparison of our GPS and InSAR velocities suggests that Sudurjökull experienced elevated velocity in late February 1994, which, when other studies are considered, appears to be consistent with a glacier surge.

INTRODUCTION

At the end of the 20th century, the mass loss of glaciers and ice caps (excluding those of Antarctica and Greenland) is estimated to have formed the largest cryospheric component of the observed sea-level rise of 3.1 ± 0.7 mm a^{-1} (Lemke and others, 2007). Estimates of the 21st-century sea-level contribution due to glaciers and ice caps vary by a factor of two (Van de Wal and Wild, 2001; Raper and Braithwaite, 2006; Meehl and others 2007) depending on how the sensitivity of ice mass balance to future climate forcing is modelled. Because ice velocity is a factor in the estimation of glacier mass balance, knowledge of its seasonal and interannual variability is important to gain an improved understanding of the response of glaciers and ice caps to expected climate change.

About 11% (11 200 km^2) of Iceland is covered by temperate ice (Fig. 1), comprising roughly 4% of the 272 200 km^2 of Arctic land ice outside of Greenland (Dowdeswell and others, 1997). In the maritime Icelandic climate, snow accumulation is sensitive to winter temperature and the position of the paths of the North Atlantic low-pressure weather fronts. As a consequence, the temperate glaciers of Iceland are dynamically active and respond sensitively to climatic fluctuations (Björnsson, 1979). On the highest parts of the main ice caps, average annual temperatures are below freezing. Due to a steeply decreasing precipitation gradient from south to north, south-flowing glaciers tend to be steep and fast-flowing, terminating at low altitude in areas of high ablation. Conversely, north-flowing glaciers have lower accumulation in their higher reaches, shallower slopes and terminate in broad fronts at higher altitudes. During the early 20th century, there was a general recession of Icelandic glaciers which accelerated after the 1930s and slowed after the 1960s (Björnsson, 1979).

With an area of 925 km^2, Langjökull is Iceland's second largest ice cap (Björnsson and Pálsson, 2008). Radio-echo sounding has revealed a mean ice thickness of about 200 m and a maximum of 580 m (Björnsson and others, 2006). Total ice volume is estimated to be 195 km^3, which is equivalent to 0.5 mm of eustatic sea-level rise (SLR). The southern outlet glacier of Hagafellsjökull Vestri flows down to an altitude of 500 m and, following at least 40 years of quiescence, has experienced four separate periods of glacier surging between 1971 and 2002 affecting an area of 150 km^2 (Björnsson and others, 2003). The surface mass balance of Langjökull ice cap (LIC) has been measured at 22 stake locations since 1996. The net surface mass balance was negative from 1996 to 2001, resulting in a loss of 5.36 km^3 of ice or 3% of the total ice-cap mass. Although there is no simple relationship to explain the observed mass loss, the minimum winter surface mass balance in 2001 coincided with a precipitation minimum recorded at a nearby meteorological station (Hveravellir), and, in consequence, it would appear to have meteorological origins (Björnsson and others, 2002).

In this study, we use interferometric synthetic aperture radar (InSAR) to determine the velocity of LIC in 1994, and ground-based global positioning system (GPS) observations made in 2001 to investigate the extent to which velocity fluctuations may be responsible for recent mass trends.

METHODS

A repeat-pass interferogram calculated from synthetic aperture radar (SAR) data records surface motion within the data repeat interval (Goldstein and others, 1993). If the perpendicular component of distance between sensor positions of the repeat-pass data is non-zero, there is an additional topographic contribution to the interferometric phase which can be removed to isolate the motion contribution (Kwok and Fahnestock, 1996). A single interferogram measures only the component of motion in the satellite line of sight (LOS), orthogonal to the flight path. To estimate surface motion in three dimensions, interferograms from ascending and descending satellite orbits can be combined with the additional assumption of ice motion parallel to the ice surface (Joughin and others, 1998). In general, ice does not flow parallel to the surface; instead, ice flow is inclined slightly upwards in the ablation zone and slightly downwards in the accumulation zone (Paterson, 1994). For LIC, where slopes are low and both accumulation and ablation are modest, the assumption of surface-parallel flow should

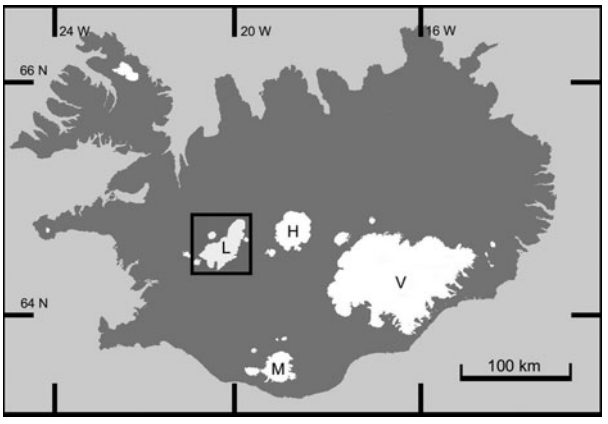

Fig. 1. Location of Langjökull and other major ice caps in Iceland.

not yield significant errors in estimates of vertical motion. Estimates of horizontal components of motion should be relatively unaffected by deviations from surface-parallel flow because the SAR look direction is close to nadir (~24°) and because surface gradients of LIC are low. In the absence of SAR data acquired from separate orbits, the ice-flow direction can be estimated from the direction of maximum averaged (over an area with a radius of 10–20 times the ice thickness) downhill slope (Paterson, 1994).

Repeat-pass interferograms were derived from pairs of European Remote-sensing Satellite-1 (ERS-1) SAR images obtained from satellite passes sequentially 3 days apart in late February 1994 (Table 1). Data were acquired from both ascending and descending satellite orbits, providing InSAR data oriented in approximately orthogonal directions. The SAR scenes were co-registered to sub-pixel accuracy using a cross-correlation of the detected single-look complex data (Wegmüller and others, 1998). We removed the 'flat-Earth' component arising from the Earth's curvature using precise orbit information (Scharroo and Visser, 1998). The phase contribution due to topography was removed by subtracting a synthetic interferogram (Massonnet and Rabaute, 1993) generated from a digital elevation model (DEM) of LIC. This external DEM was constructed from a GPS survey conducted in April 1997, with values in the horizontal axes equally spaced every 200 m and an estimated vertical accuracy of 2–5 m. After accounting for these topographic signals, the phase due to motion during the repeat-pass interval was unwrapped (Wegmüller and others, 1998) and from this we generated ice displacement maps in both ascending and descending geometries.

LIC displacement maps formed from InSAR data acquired in ascending and descending satellite orbits were then combined with the surface DEM to derive a three-dimensional (3-D) surface-parallel ice velocity vector field for about 50% of the ice cap (Fig. 2). Ice velocity errors in areas with dual-look InSAR coverage were about 5 m a^{-1} as estimated from the range of ice velocity values measured for stationary bedrock (root-mean-square (rms) value is 4.5 m a^{-1}). However, to improve spatial coverage we augmented the 3-D velocity field with estimates of ice motion derived from single-look InSAR displacement fields in other areas, excluding data for which the angle between sensor look direction and local aspect was >72°. This procedure introduced an additional error due to uncertainties in the ice-flow direction, which we estimate to be ±5°. As the southern part of LIC was not covered by ascending-pass data, ice velocities were calculated in that location using descending-pass data only and we estimate errors for this area to be ~10 m a^{-1} as estimated in the same way as the dual-look error (rms value is 8.8 m a^{-1}). The sensor LOS for ascending passes is almost perpendicular to the direction of ice flow, and is therefore insensitive to ice motion at the south-flowing glaciers in the southern part of the ice cap.

Finally, ice motion was determined at 22 stakes positioned across LIC (Fig. 2) during the summer of 2001 (April to October) over a period of 170 days using differential GPS. The error on the stake velocities was calculated by dividing the sum of the error in the position of the differential GPS measurements (2 × 50 cm) by the interval between measurements (170 days) to obtain a value of ±2.2 m a^{-1}.

Table 1. ERS SAR data used in our study

Satellite heading	Image dates	Satellite orbits	Interferogram perpendicular baseline m	Interferogram temporal baseline days
Descending	22 Feb 1994 25 Feb 1994	13625 13668	140	3
Ascending	24 Feb 1994 27 Feb 1994	13660 13703	80	3

RESULTS AND DISCUSSION

Our InSAR data represent the first detailed map of the LIC velocity field (Fig. 2). Eight outlet glaciers are apparent from the InSAR velocity data, with the majority located in the northern half of LIC. Three glaciers flow to the west or northwest and the remainder flow to the east or southeast. Although apparent from GPS measurements (locations 1–8, Fig. 2), the southward-flowing outlet glacier of Hagafellsjökull Vestri is not obvious in the InSAR data due to the large angle between the ice-flow direction and the radar look direction, a condition that is not favourable for detecting ice motion from single-pass data. These eight glaciers surveyed range in area from 18 to 71 km^2 (Table 2), and the maximum ice speed we have recorded is 75 m a^{-1} at the terminus of Sudurjökull in the southeast part of LIC. Derived velocities are below the InSAR measurement error for 32% of LIC and are omitted from Figure 2. The elevation at which the surveyed glaciers reach their maximum velocity varies between 1200 m for the northeast glacier to 870 m for Kirkjujökull, with an average across all eight outlet glaciers of 1000 m.

We extracted InSAR velocity data along eight transects (see Fig. 2) of LIC that passed close to the centre of each principal glacier and were linked by the GPS survey sites, to allow for a more detailed comparison of the two datasets. A summary of LIC geometry and flow along each transect is shown in Table 2. The glaciers can be grouped by the shape of their InSAR velocity profiles as shown in Figure 3. Along the northwest and northeast profiles, ice velocity increases progressively from near-zero at the highest elevations to a maximum about 2.5 km from the ice margin at an elevation of about 1150 m, and decreases gradually thereafter to about zero at the terminus. The southwest transect has similar characteristics, although, due to loss of coherence near the ice margin, InSAR velocity was not retrievable for the whole

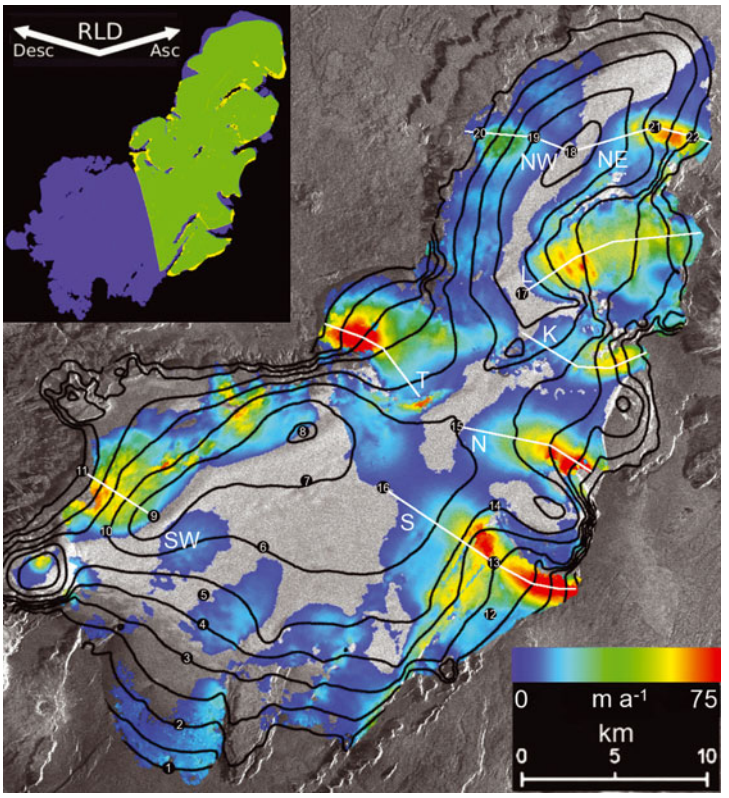

Fig. 2. Ice velocity map with 100 m elevation contours, GPS stake locations and data transects shown in Figures 3 and 4, projected over SAR intensity image. Locations of data transects are shown in white: northwest transect (NW), northeast transect (NE), Leidarjökull (L), Kirkjujökull (K), Nordurjökull (N), Sudurjökull (S), southwest transect (SW), Thristapajökull (T). Areas of 3-D velocity (green), ascending pass only (yellow) and descending pass only (blue) are shown in the inset. Radar look direction (RLD) for ascending (Asc) and descending passes (Desc) is also shown.

profile. Although Kirkjujökull exhibits a similar profile, ice velocity at the terminus is about 20 m a^{-1}. At Thristapajökull, the ice velocity increases along the transect until it reaches its maximum value of 75 m a^{-1} about 3 km from the margin. Below this, ice velocity decreases with a roughly constant rate to about 30 m a^{-1} at the ice margin.

The three remaining transects exhibit markedly different behaviour from those above as well as each other (Fig. 3). Ice velocity for Leidarjökull increases rapidly from the ice divide to a maximum of 40 m a^{-1} within a short distance (4 km) of the ice divide. Thereafter, it remains approximately constant at about 30 m a^{-1} before decreasing to about 10 m a^{-1} in the final 2 km. The lower part of the outlet covers a caldera where ice thickness is ~400 m. The central part of the surface profile has a shallower surface gradient, and a rough estimate of the deformation velocity (from surface slope and ice thickness) yields ~15 m a^{-1}, which accounts for only half of the observed surface flow. Calculations of basal water pressure based on radio-echo sounding studies of bedrock topography (Flowers and others, 2007; Guðmundsson and others, 2009) suggest that sliding at the bed is enhanced for Leidarjökull, which helps to explain the concave-up surface profile. At Nordurjökull, ice velocity increases at roughly a constant rate along the length of the profile, although, due to coherence loss near the terminus, we were unable to retrieve InSAR velocity for the final 1 km. The lower slopes of this glacier are narrow and steep and the outlet flows into the Hvítárvatn lake. Though

Table 2. InSAR velocity transect attributes. Position and elevation of maximum speed are the distance from the margin (km) and altitude (m), respectively, at which maximum ice speed occurs

Transect	Length	Maximum speed	Average speed	Average elevation	Position of max. speed	Elevation of max. speed	Glacier area
	km	m a^{-1}	m a^{-1}	m a.s.l.	km	m a.s.l.	km^2
Northwest	7.0	25	14	1200	2.4	1100	18.5
Northeast	9.0	44	22	1180	2.5	1200	18.3
Thristapajökull	8.0	75	36	940	2.8	900	53.3
Leidarjökull	12.0	37	25	1065	7.5	1100	71.2
Kirkjujökull	7.5	38	20	1050	2.0	870	17.6
Nordurjökull	10.0	64	28	1040	1.7	880	37.4
Southwest	5.0	44	30	1125	1.5	1030	39.4
Sudurjökull	13.5	63	34	980	4.8	890	61.3

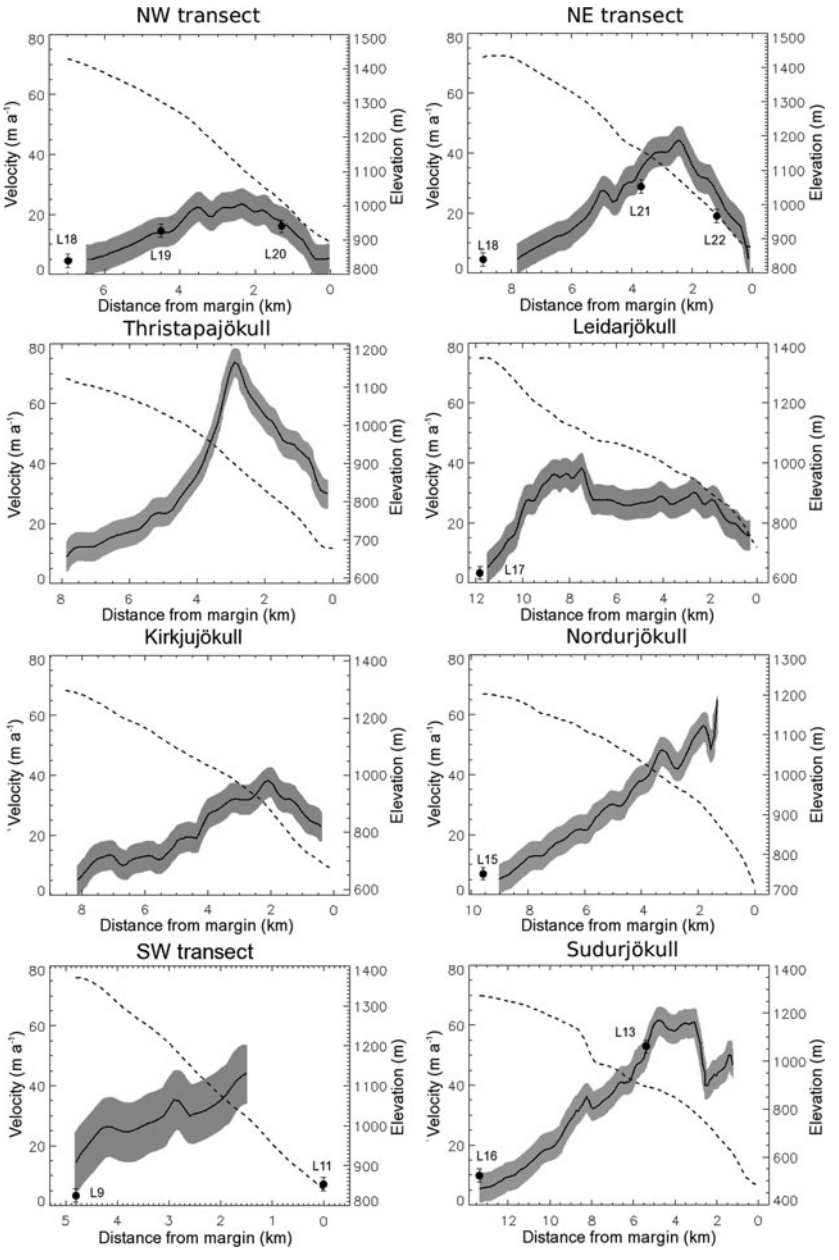

Fig. 3. InSAR-derived velocity for winter 1994 (solid curve) and 1997 ice surface (dashed curve) for transects shown in Figure 2. Solid points with error bars show 2001 summer velocity from stake measurements. Grey areas show error for InSAR velocity values.

the terminus does not float, ice breaks off at the margin into the lake, and the presence of water is likely to reduce basal friction, which may explain the high ice velocity near the terminus. Along Sudurjökull, ice velocity increases gradually downslope from the ice divide to about 60 m a^{-1} where it remains roughly constant for ~2 km. At 3 km from the margin, ice velocity drops by 20 m a^{-1} in 500 m horizontal distance; although low coherence prevented retrieval of the final 1 km, it is likely that ice velocity at the terminus is about 40 m a^{-1}. This area of high velocity on the lower slopes suggests that in February 1994 Sudurjökull was experiencing a surge. The record of GPS-surveyed velocities at site L13 between summer 1997 and summer 2008 also suggests that another surge started in summer 1999 (the velocity in summer 1999 is 65 m a^{-1}) and culminated in 2004; by 2005 the velocity had dropped to 40 m a^{-1}. The positions of the terminus on maps from 1986, 1997 and 2004 show that the terminus must have advanced between 1986 and 1997 and again between 1997 and 2004, which is consistent with the above. There is anecdotal evidence that Sudurjökull has surged in the past (Björnsson and others, 2003) and it is also known from sediments in the lake in front of the terminus that Sudurjökull has been extremely dynamic (Geirsdóttir and others, 2008).

The correlation between the InSAR and GPS data, shown in Figure 4, is 0.79 with a rms difference of 5 m a^{-1}. Observations at locations on Hagafellsjökull Vestri were omitted, as ice flows in a direction for which the sensor had little sensitivity due to the acquisition geometry. In addition, the GPS data for this glacier show that, in 2001, the glacier velocity peaked 9.4 km from the margin at an elevation of 950 m and velocity was enhanced following a surge event of 1999, so agreement between the InSAR and GPS observations is not expected. That the smallest measurement uncertainties (±5 m a^{-1}) are at the level of the rms difference between the InSAR and GPS velocities suggests that any seasonal or interannual variations in ice velocity between February1994 and summer 2001 are modest.

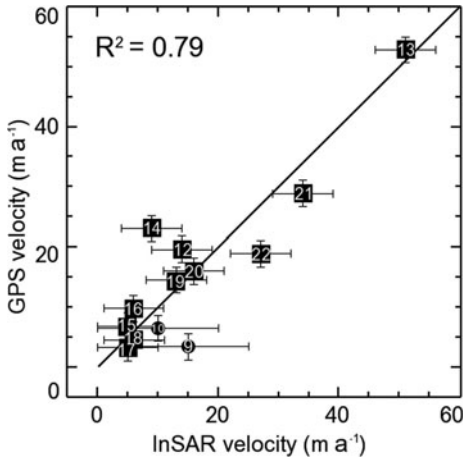

Fig. 4. Comparison of InSAR- and GPS-derived ice velocities for 13 locations on the ice cap, numbered as in Figure 2. Data from locations covered by dual-look InSAR are shown as squares; those for single-look coverage are shown as circles. Stake locations on Hagafellsjökull Vestri (1–8) are omitted – as agreement is not expected due to enhanced ice velocity in 2001 following a glacier surge in 1999 and the fact that the radar look direction is insensitive to flow. Location 11 was also omitted from the comparison, as no InSAR data were available within 500 m.

CONCLUSIONS

This research provides the first ice velocity map for LIC. The velocity data were derived from ERS SAR interferometry and the data were acquired between 22 and 27 February 1994. We have identified eight principal outlet glaciers, and the maximum speed recorded was 75 m a^{-1}. Eight down-glacier velocity transects were extracted, along three of which we were able to compare our InSAR results with sparse surface velocity measurements determined from a GPS survey undertaken over 170 days during summer 2001. At six of the eleven locations included in both the GPS and InSAR datasets, ice velocity measurements were within error, indicating little change in ice velocity between February1994 and summer 2001. The largest difference (47 ± 10 m a^{-1}) between the InSAR and GPS velocity datasets occurred at Hagafellsjökull Vestri (L4) and is attributed to locally high InSAR measurement error and the fact that, in 2001, ice velocity was elevated following a surge.

The close agreement between the GPS and InSAR datasets indicates that seasonal ice velocity variations at LIC are small, though non-zero velocities at the termini of four of the eight glaciers surveyed suggest that these glaciers were advancing in February 1994. Our data, in addition to other studies, suggest that Sudurjökull was experiencing a surge in 1994.

REFERENCES

Björnsson, H. 1979. Glaciers in Iceland. *Jökull,* **29**, 74–80.

Björnsson, H. and F. Pálsson. 2008. Icelandic glaciers. *Jökull,* **58**, 365–386.

Björnsson, H., F. Pálsson and H. Haraldsson. 2002. Mass balance of Vatnajökull (1991–2001) and Langjökull (1996–2001), Iceland. *Jökull,* **51**, 75–78.

Björnsson, H., F. Pálsson, O. Sigurðsson and G.E. Flowers. 2003. Surges of glaciers in Iceland. *Ann. Glaciol.,* **36**, 82–90.

Björnsson, H., S. Gudmundsson, T. Jóhannesson, F. Pálsson, G. Aðalgeirsdóttir and H. Haraldsson 2006. *Geometry, mass balance and climate change response of Langjökull ice cap, Iceland.* Obergurgl, International Arctic Science Committee. Working Group on Arctic Glaciology.

Dowdeswell, J.A. *and 10 others.* 1997. The mass balance of circum-Arctic glaciers and recent climate change. *Quat. Res.,* **48**(1), 1–14.

Flowers, G.E., H. Björnsson, A. Geirsdóttir, G.H. Miller and G.K.C. Clarke. 2007. Glacier fluctuation and inferred climatology of Langjökull ice cap through the Little Ice Age. *Quat. Sci. Rev.,* **26**(19–21), 2337–2353.

Geirsdóttir, A., G.H. Miller, N.J. Wattrus, H. Björnsson and K. Thors. 2008. Stabilization of glaciers terminating in closed water bodies: evidence and broader implications. *Geophys. Res. Lett.,* **35**(17), L17502. (10.1029/2008GL034432.)

Goldstein, R.M., H. Engelhardt, B. Kamb and R.M. Frolich. 1993. Satellite radar interferometry for monitoring ice sheet motion: application to an Antarctic ice stream. *Science,* **262**(5139), 1525–1530.

Guðmundsson, S., H. Björnsson, G. Aðalgeirsdóttir, T. Jóhannesson, F. Pálsson and O. Sigurðsson. 2009. Similarities and differences in the response of two ice caps in Iceland to climate warming. *Hydrol. Res.,* **40**(5), 495–502.

Joughin, I.R., R. Kwok and M.A. Fahnestock. 1998. Interferometric estimation of three-dimensional ice-flow using ascending and descending passes. *IEEE Trans. Geosci. Remote Sens.,* **36**(1), 25–37.

Kwok, R. and M.A. Fahnestock. 1996. Ice sheet motion and topography from radar interferometry. *IEEE Trans. Geosci. Remote Sens.,* **34**(1), 189–200.

Lemke, P. *and 10 others.* 2007. Observations: changes in snow, ice and frozen ground. *In* Solomon, S. *and 7 others, eds. Climate change 2007: the physical science basis. Contribution of Working Group I to the Fourth Assessment Report of the Intergovernmental Panel on Climate Change.* Cambridge, etc., Cambridge University Press, 337–383.

Massonnet, D. and T. Rabaute. 1993. Radar interferometry: limits and potential. *IEEE Trans. Geosci. Remote Sens.,* **31**(2), 455–464.

Meehl, G.A. *and 12 others.* 2007. Global climate projections. *In* Solomon, S. *and 7 others, eds. Climate change 2007: the physical science basis. Contribution of Working Group I to the Fourth Assessment Report of the Intergovernmental Panel on Climate Change.* Cambridge, etc., Cambridge University Press, 747–845.

Paterson, W.S.B. 1994. *The physics of glaciers. Third edition.* Oxford, etc., Elsevier.

Raper, S.C.B. and R.J. Braithwaite. 2006. Low sea level rise projections from mountain glaciers and icecaps under global warming. *Nature,* **439**(7074), 311–313.

Scharroo, R. and P. Visser. 1998. Precise orbit determination and gravity field improvement for the ERS satellites. *J. Geophys. Res.,* **103**(C4), 8113–8127.

Van de Wal, R.S.W. and M. Wild. 2001. Modelling the response of glaciers to climate change by applying volume–area scaling in combination with a high resolution GCM. *Climate Dyn.,* **18**(3–4), 359–366.

Wegmüller, U., C. Werner and T. Strozzi. 1998. SAR interferometric and differential interferometric processing chain. *In* Stein, T.I., *ed. IGARSS '98. 18th International Geoscience and Remote Sensing Symposium, 6–10 July 1998, Seattle, Washington. Proceedings. Vol. 2.* Piscataway, NJ, Institute of Electrical and Electronics Engineers, 1106–1108.

MS received 17 July 2008 and accepted in revised form 4 May 2009